

Isogeometric Analysis of Acoustic Scattering using Infinite Elements

Jon Vegard Venås^{a,*}, Trond Kvamsdal^a, Trond Jenserud^b

^a*Department of Mathematical Sciences, Norwegian University of Science and Technology, Trondheim, Norway*

^b*Department of Marine Systems, Norwegian Defence Research Establishment, Horten, Norway*

Abstract

Isogeometric analysis (IGA) has proven to be an improvement on the classical finite element method (FEM) in several fields, including structural mechanics and fluid dynamics. In this paper, the performance of IGA coupled with the infinite element method (IEM) for some acoustic scattering problems is investigated. In particular, the simple problem of acoustic scattering by a rigid sphere, and the scattering of acoustic waves by an elastic spherical shell with fluid domains both inside and outside, representing a full acoustic-structure interaction (ASI) problem. Finally, a mock shell and a simplified submarine benchmark are investigated. The numerical examples include comparisons between IGA and the FEM. Our main finding is that the usage of IGA significantly increases the accuracy compared to the usage of C^0 FEM due to increased inter-element continuity of the spline basis functions.

Keywords:

Isogeometric analysis, acoustic scattering, infinite elements, acoustic-structure interaction.

1. Introduction

Acoustic scattering is the physical phenomena of how sound interacts with objects and medium fluctuations. When an acoustic wave hits a rigid object, it is totally reflected, and the object is left in a quiescent state. In the case of an elastic object, part of the sound is transmitted into the object, which is set into motion and starts radiating sound. This leads to a coupled acoustic-structure interaction (ASI) problem. Applications include underwater acoustics [1] and noise propagation in air [2]. Inverse problems are also of interest, such as shape optimization of membranes [3] and the problem of designing submarines with low scattering strength. Assuming harmonic time dependency, the fluid and solid media can be modeled using the scalar and vector Helmholtz equations, respectively. The vector Helmholtz equation can be used to model electromagnetic waves [4], such that the work presented herein can also be used for electromagnetic scattering.

Herein, the acoustic scattering characterized by sound waves reflected by man-made elastic objects will be addressed. Shape optimization for optimal acoustic scattering on man-made objects, e.g. antennas, submarines etc., is a typical problem facing design engineers.

Isogeometric analysis (IGA) is basically an extension of the finite element method (FEM) using non-uniform rational B-splines (NURBS) as basis functions not only representing the solution space, but also the geometry. Being introduced in 2005 by Hughes et al. [5], followed by the book [6] in 2009, IGA tries to bridge the gap between finite element analysis (FEA) and computer aided design (CAD) tools. The important feature of IGA is that it uses the same basis as CAD software for describing the given geometry, and thus exact representation of the model is possible.

The physical problem is illustrated in Figure 1 where the incoming sound waves, p_{inc} , originate from a point source far from this object, such that the (spherical) sound waves are quite accurately approximated

*Corresponding author.

Email addresses: Jon.Venas@ntnu.no (Jon Vegard Venås), Trond.Kvamsdal@ntnu.no (Trond Kvamsdal), Trond.Jenserud@ffi.no (Trond Jenserud)

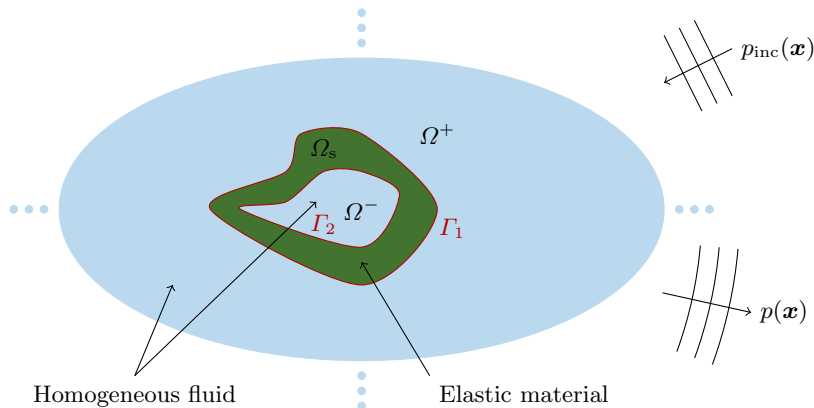


Figure 1: Illustration of the physical problem. A plane incident wave, $p_{\text{inc}}(\mathbf{x})$, is scattered by the scatterer, Ω_s , in an unbounded domain, Ω^+ , resulting in the scattered wave, $p(\mathbf{x})$. The scatterer, which is bounded by the boundaries Γ_1 and Γ_2 , envelops a fluid domain, Ω^- .

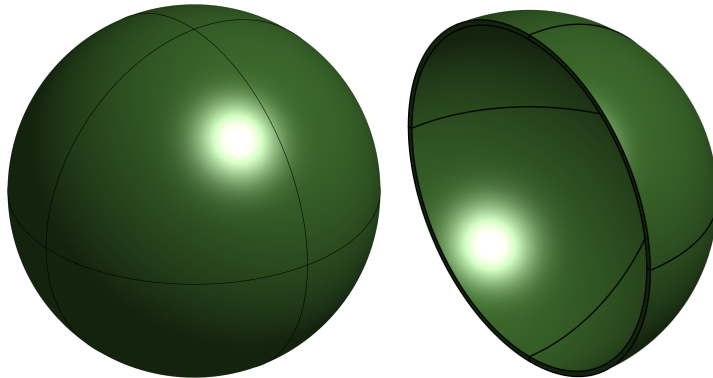


Figure 2: Exact geometry of a spherical shell using 8 elements.

by plane waves when the waves reaches the proximity of the object. For rigid objects of irregular shape, the incoming wave may be reflected multiple times before leaving the object. When the object is elastic a coupled ASI problem results. The goal is then to calculate the scattered wave p at an arbitrary far field point. Finally, to use the FEM or IGA the domain must be finite. A fictitious boundary is thus introduced, which must be implemented in such a way that outgoing waves reaching this boundary are absorbed.

The problem at hand is time dependent. However, harmonic time dependency will be assumed, such that all time dependent functions may be written as $\tilde{F} = \tilde{F}(\mathbf{x}, t) = F(\mathbf{x})e^{-i\omega t}$ where ω is the angular frequency and $i = \sqrt{-1}$ the imaginary unit. This enables us to model the pressure p in the fluid with the Helmholtz equation given by

$$\nabla^2 p + k^2 p = 0 \quad (1)$$

with the wave number $k = \frac{\omega}{c_f}$ (where c_f is the wave speed in the fluid). Other important quantities include the frequency $f = \frac{\omega}{2\pi}$ and the wavelength $\lambda = \frac{2\pi}{k}$.

The geometry of the elastic object may be quite complex, but is typically exactly represented using NURBS. This fact is one of the motivating factor for using IGA, as it uses the same functions as basis functions for analysis. The spherical shell depicted in Figure 2 is an example of a geometry that has an exact representation using NURBS, but is outside the space of standard (Lagrangian) FEM geometries.

It has been shown that the continuity of the basis functions plays an important role for the accuracy of solving elliptical problems (for instance the Helmholtz equation), see [7] and [8]. This motivates the use of IGA even further, as IGA enables control of the continuity of the basis function up to C^{p-1} (in contrast

with the C^0 -continuity restriction in FEA). IGA has proven to be promising in a host of areas related to the problem at hand, which yields further motivation in the use of IGA. For instance, in [9] the method was shown to be suited for the more complex scenario of sound propagation through laminar flow.

In addition to IGA, the so-called infinite element method (IEM) has been chosen to handle the boundary conditions at the artificial boundary. Typically, the boundary element method (BEM) [10, 11] has been used for this purpose. However, for higher frequencies and complex geometries, BEM becomes computationally expensive (although improvement in performance has been done in the recent decades [12]). The main motivation for the infinite element method is computational efficiency as reported by Burnett [13] and Gerdes and Demkowicz [14].

Before starting on the full ASI problem, it is important to establish good results for the IEM. This method only applies for the outer fluid, and it would thus be natural to first investigate the scattering problem on rigid objects (that is, no acoustic-structure interaction occurs). An introduction to the IEM is presented in Section 2. The extension to ASI problems (presented in Section 3) naturally follows from the implementation of rigid scattering using IEM. In Section 4 the results obtained for both rigid and elastic scattering on a spherical shell is presented. Results for rigid scattering from a mock shell are included to investigate condition numbers. Moreover, results for a simplified submarine is presented to illustrate the performance of the implementation on complex geometries. Finally, conclusions and suggested future work can be found in Section 5.

2. Exterior Helmholtz problems

Scattering problems involve *unbounded exterior domains*, Ω^+ . A common method for solving such problems with the FEM is to introduce an artificial boundary that encloses the scatterer. On the artificial boundary some sort of absorbing boundary condition (ABC) is prescribed. The problem is then reduced to a finite domain, and both the elastic scatterer and the bounded domain between the scatterer and the artificial boundary can be discretized with finite elements. Several methods exist for handling the exterior Helmholtz problem (on unbounded domain), including

- the perfectly matched layer (PML) method after Bérenger [15, 16]
- the boundary element method [10, 11, 17, 18]
- Dirichlet to Neumann-operators (DtN-operators) [19]
- local differential ABC operators [20, 21, 22, 23]
- the infinite element method. [24, 25]

Herein, the infinite element method is chosen. For the IEM, the unbounded domain Ω^+ is partitioned into two domains by the artificial boundary Γ_a ; Ω_a and Ω_a^+ (see Figure 3). These domains are discretized by finite and infinite elements, respectively. A convergence analysis of a coupled FEM-IEM can be found in [26].

The exterior Helmholtz problem is given by

$$\nabla^2 p + k^2 p = 0 \quad \text{in } \Omega^+, \quad (2)$$

$$\partial_n p = g \quad \text{on } \Gamma_1, \quad (3)$$

$$\frac{\partial p}{\partial r} - ikp = o(r^{-1}) \quad \text{with } r = |\mathbf{x}| \quad (4)$$

where the Sommerfeld condition [27] in Eq. (4) restricts the field in the limit $r \rightarrow \infty$ uniformly in $\hat{\mathbf{x}} = \frac{\mathbf{x}}{r}$, such that no waves originate from infinity. The Neumann condition given by the function g will in the case of rigid scattering be given by the incident wave p_{inc} . Zero displacement of the fluid normal on the scatterer (rigid scattering) implies that $\partial_n(p + p_{\text{inc}}) = 0$ where ∂_n denotes the partial derivative in the normal direction on the surface Γ_1 (pointing “out” from Ω^+), which implies that

$$g = -\frac{\partial p_{\text{inc}}}{\partial n}. \quad (5)$$

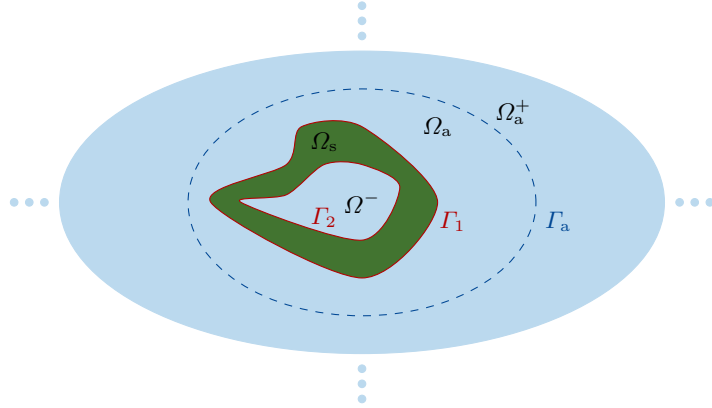


Figure 3: An artificial boundary Γ_a is introduced such that the exterior domain Ω^+ is decomposed by the two domains Ω_a (which is bounded by Γ_1 and Γ_a) and Ω_a^+ . Thus, $\Omega^+ = \Omega_a \cup \Omega_a^+$.

Plane incident waves (with amplitude P_{inc}) traveling in the direction \mathbf{d}_s can be written as

$$p_{\text{inc}} = P_{\text{inc}} e^{ik\mathbf{d}_s \cdot \mathbf{x}}. \quad (6)$$

The normal derivative on the surface of any smooth geometry may then be computed by

$$\frac{\partial p_{\text{inc}}}{\partial n} = \mathbf{n} \cdot \nabla p_{\text{inc}} = ik\mathbf{d}_s \cdot \mathbf{n} p_{\text{inc}}. \quad (7)$$

2.1. Weak formulation for the Helmholtz equation

In order to choose the correct solution space in the infinite element method, the asymptotic behavior of the scattered pressure p at large radii¹ r must be examined. In [28], Wilcox shows that the scalar pressure field $p(\mathbf{x})$ satisfying the Helmholtz equation and the Sommerfeld radiation conditions can be written in the form²

$$p(\mathbf{x}) = \frac{e^{ikr}}{r} \sum_{n=0}^{\infty} \frac{p_n(\vartheta, \varphi)}{r^n}, \quad (8)$$

which implies that $|p| = \mathcal{O}(r^{-1})$ asymptotically for large r . Considering a function which represents this asymptotic property

$$\Psi(r) = \frac{e^{ikr}}{r}, \quad (9)$$

one can observe that the L^2 Hermitian inner product does not exist. Indeed, if Γ_1 is the unit sphere then

$$(\Psi, \Psi)_{L^2} = \int_{\Omega^+} \frac{e^{ikr}}{r} \frac{e^{-ikr}}{r} d\Omega = 4\pi \int_1^{\infty} \frac{1}{r^2} r^2 dr,$$

which is not finite. The solution to the problem is to introduce weighted norms by defining the inner product

$$(p, q)_w = \int_{\Omega^+} w p \bar{q} d\Omega, \quad \text{with } w = \frac{1}{r^2}. \quad (10)$$

The following norm may then be induced

$$\|p\|_{1,w} = \sqrt{(p, p)_w + (\nabla p, \nabla p)_w} \quad (11)$$

¹Here, r is referred to as the radius even though it does not necessarily represent the radius in spherical coordinates.

²In some appropriate coordinate system (r, ϑ, φ) with the “radial variable”, r , extending to infinity. Typically some degeneration of the ellipsoidal (in 3D) coordinate system.

such that the trial functions satisfy $\|p\|_{1,w} < \infty$. The integrals

$$\int_{\Omega^+} p\bar{q} \, d\Omega \quad \text{and} \quad \int_{\Omega^+} \nabla p \cdot \nabla \bar{q} \, d\Omega \quad (12)$$

are well defined if the test functions q are such that

$$(q, q)_{w^*} < \infty \quad \text{and} \quad (\nabla q, \nabla q)_{w^*} < \infty \quad (13)$$

with the inner product

$$(p, q)_{w^*} = \int_{\Omega^+} w^* p \bar{q} \, d\Omega, \quad \text{with} \quad w^* = r^2, \quad (14)$$

and the corresponding norm

$$\|p\|_{1,w^*} = \sqrt{(p, p)_{w^*} + (\nabla p, \nabla p)_{w^*}}. \quad (15)$$

Define now the following *weighted Sobolev spaces* for the trial- and test spaces

$$H_w^1(\Omega^+) = \{p : \|p\|_{1,w} < \infty\} \quad \text{and} \quad H_{w^*}^1(\Omega^+) = \{q : \|q\|_{1,w^*} < \infty\}, \quad (16)$$

respectively. These definitions will not ensure that all trial function satisfy the Sommerfeld condition. Leis solved this problem in [29] by modifying the trial space to be

$$H_w^{1+}(\Omega^+) = \{p : \|p\|_{1,w}^+ < \infty\} \quad (17)$$

where

$$\|p\|_{1,w}^+ = \sqrt{\|p\|_{1,w}^2 + \int_{\Omega^+} \left| \frac{\partial p}{\partial r} - ikp \right|^2 \, d\Omega}. \quad (18)$$

For a more detailed discussion of the functional analysis involved in these spaces refer to the book by Ihlenburg [30, pp. 41-43].

The weak form of the Helmholtz equation may now be found by multiplying Eq. (2) with a test function and integration over the domain

$$\int_{\Omega^+} [q \nabla^2 p + k^2 qp] \, d\Omega = 0.$$

Using Greens first identity this can be written as

$$- \int_{\Omega^+} \nabla q \cdot \nabla p \, d\Omega + \int_{\partial\Omega^+} q \nabla p \cdot \mathbf{n} \, d\Gamma + k^2 \int_{\Omega^+} qp \, d\Omega = 0.$$

Thus,

$$\int_{\Omega^+} \nabla q \cdot \nabla p \, d\Omega - k^2 \int_{\Omega^+} qp \, d\Omega = \int_{\partial\Omega^+} qg \, d\Gamma. \quad (19)$$

The weak formulation then becomes:

$$\text{Find } p \in H_w^{1+}(\Omega^+) \text{ such that } B(q, p) = L(q), \quad \forall q \in H_{w^*}^1(\Omega^+), \quad (20)$$

where the bilinear form is given by

$$B(q, p) = \int_{\Omega^+} [\nabla q \cdot \nabla p - k^2 qp] \, d\Omega$$

and the corresponding linear form is given by

$$L(q) = \int_{\Gamma_1} qg \, d\Gamma.$$

2.2. Infinite elements

In the following, a derivation of the weak formulation for infinite elements using a prolate spheroidal coordinate system is presented (cf. [13]). The IEM is typically presented with four infinite element formulations:

- Petrov–Galerkin conjugated (PGC)
- Petrov–Galerkin unconjugated (PGU)
- Bubnov–Galerkin conjugated (BGC)
- Bubnov–Galerkin unconjugated (BGU)

The Petrov–Galerkin formulations are based on the weighted Sobolev spaces after Leis [29]. It turns out that it is possible to create Bubnov–Galerkin formulations as well when the integration in the weak formulation is understood in the sense of the Cauchy principal value (consider [13] and [31] for details). These spaces differ compared to the Petrov–Galerkin counterpart in that the test space and trial space are equal. The difference between the conjugated formulations and the unconjugated formulations is simply conjugations of the test functions in the weak formulation. The accuracy of these formulations has been assessed in the overview in [32].

The idea of the IEM is to partition the unbounded domain Ω^+ into Ω_a and Ω_a^+ separated by an artificial boundary Γ_a (cf. Figure 3). These two domains can then be discretized with finite elements and infinite elements, respectively. The boundary of the scatterer is assumed to be parameterized using 3D NURBS surface patches, such that the domain Ω_a can be parameterized using 3D NURBS volume patches. Denote by $\mathcal{V}_h(\Omega_a)$, the space spanned by these trivariate NURBS-basis functions. As the 3D NURBS volume representation of Ω_a reduces to a NURBS surface parametrization at Γ_a , a natural partition of Γ_a into surface elements arises. Denote by $\mathcal{V}_h(\Gamma_a)$, the space spanned by the resulting bivariate basis functions. Consider now the following basis of the *radial shape functions* which is motivated by the Wilcox expansion in Eq. (8)

$$\mathcal{I}_{N,w}^+ = \text{span} \left(\left\{ \frac{e^{ikr}}{r^n} \right\}_{n=1,\dots,N} \right). \quad (21)$$

Moreover, define corresponding spaces for the test-space

$$\mathcal{I}_{N,w^*}^+ = \begin{cases} \mathcal{I}_{N,w}^+ & \text{for Bubnov–Galerkin formulations} \\ \text{span} \left(\left\{ \frac{e^{ikr}}{r^{n+2}} \right\}_{n=1,\dots,N} \right) & \text{for Petrov–Galerkin formulations.} \end{cases} \quad (22)$$

The trial- and test spaces for the infinite elements can then be defined by

$$\mathcal{I}_{h,w}^+ = \mathcal{V}_h(\Gamma_a) \times \mathcal{I}_{N,w}^+, \quad (23)$$

$$\mathcal{I}_{h,w^*}^+ = \mathcal{V}_h(\Gamma_a) \times \mathcal{I}_{N,w^*}^+, \quad (24)$$

respectively. Finally, the trial- and test spaces for the coupled FEM-IEM can be written as

$$\mathcal{F}_{h,w}^+ = \left\{ p \in H_w^{1+}(\Omega^+); p|_{\Omega_a} \in \mathcal{V}_h(\Omega_a) \quad \text{and} \quad p|_{\Omega_a^+} \in \mathcal{I}_{h,w}^+ \right\}, \quad (25)$$

$$\mathcal{F}_{h,w^*}^+ = \left\{ q \in H_{w^*}^{1+}(\Omega^+); q|_{\Omega_a} \in \mathcal{V}_h(\Omega_a) \quad \text{and} \quad q|_{\Omega_a^+} \in \mathcal{I}_{h,w^*}^+ \right\}, \quad (26)$$

respectively. Note that $\mathcal{F}_{h,w^*}^+ = \mathcal{F}_{h,w}^+$ for Bubnov–Galerkin formulations.

For the unconjugated formulations the Galerkin formulations now takes the form:

$$\text{Find } p_h \in \mathcal{F}_{h,w}^+ \quad \text{such that} \quad B_{\text{uc}}(q_h, p_h) = L(q_h), \quad \forall q_h \in \mathcal{F}_{h,w^*}^+ \quad (27)$$

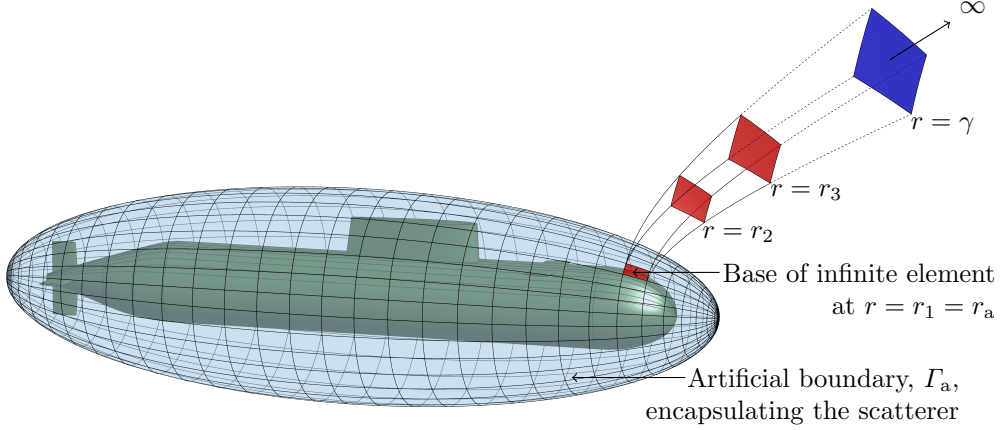


Figure 4: Illustration of an infinite element (with $N = 3$) where the radial shape functions have the Kronecker delta property at radii $r_1 = r_a$, $r_2 = \frac{5}{4}r_a$ and $r_3 = \frac{6}{4}r_a$. The (green) scatterer inside Γ_a is the BeTSSi submarine which originates from the BeTSSi workshops [1]. Note that the volume elements discretizing the domain Ω_a (bounded by the scatterer and the artificial boundary) are not shown here.

where the bilinear form and linear form are respectively given by

$$B_{uc}(q, p) = \lim_{\gamma \rightarrow \infty} \left(\int_{\Omega^\gamma} [\nabla q \cdot \nabla p - k^2 qp] d\Omega - \int_{S^\gamma} q \partial_n p d\Gamma \right), \quad (28)$$

$$L(q) = \int_{\Gamma_1} qg d\Gamma.$$

Here, S^γ is the surface at $r = \gamma$ (and Ω^γ is the domain bounded by Γ_1 and S^γ , such that $\lim_{\gamma \rightarrow \infty} \Omega^\gamma = \Omega^+$) and the full domain can then be recovered by letting $\gamma \rightarrow \infty$ (see Figure 4). Recall that $\partial_n p = \frac{\partial p}{\partial n} = \mathbf{n} \cdot \nabla p$ where \mathbf{n} is pointing “out” of Ω^γ . In the conjugated formulations the test functions q_h are conjugated.

Let r_a be the radius in the prolate spheroidal coordinate system at the artificial boundary Γ_a . Moreover, let the radial shape functions ϕ be defined by

$$\phi_m(r) = e^{ik(r-r_a)} Q_m\left(\frac{r_a}{r}\right), \quad m = 1, \dots, N \quad (29)$$

where

$$Q_m(x) = \sum_{\tilde{m}=1}^N D_{m\tilde{m}} x^{\tilde{m}} \quad (30)$$

is a set of polynomial functions defined on the half open interval $(0, 1]$. To obtain optimal sparsity of the global matrix, one should choose the polynomials such that $Q_m(1) = \delta_{m1}$, with the Kronecker delta function defined by

$$\delta_{ij} = \begin{cases} 1 & \text{if } i = j \\ 0 & \text{if } i \neq j \end{cases} \quad (31)$$

which implies that $\phi_m(r_a) = \delta_{m1}$. In [13] Burnett includes the restrictions $\phi_m(r_n) = \delta_{mn}$ with radii r_n , $n = 1, \dots, N$ (see Figure 4). Alternatively, one could use the shifted Chebyshev polynomials as done by Shirron and Dey in [33]. These polynomials are defined by the three-term recurrence relation

$$\tilde{T}_{m+1}(x) = 2(2x-1)\tilde{T}_m(x) - \tilde{T}_{m-1}(x) \quad (32)$$

for $m \geq 1$ starting with

$$\tilde{T}_0(x) = 1 \quad \text{and} \quad \tilde{T}_1(x) = 2x - 1. \quad (33)$$

Let

$$Q_m(x) = \begin{cases} x(\tilde{T}_{m-1}(x) - 1) & m > 1 \\ x & m = 1. \end{cases} \quad (34)$$

Then the coefficients $D_{m\tilde{m}}$ in Eq. (30) can be collected in the matrix (for $N \leq 6$)

$$\mathbf{D} = \begin{bmatrix} 1 & 0 & 0 & 0 & 0 & 0 \\ -2 & 2 & 0 & 0 & 0 & 0 \\ 0 & -8 & 8 & 0 & 0 & 0 \\ -2 & 18 & -48 & 32 & 0 & 0 \\ 0 & -32 & 160 & -256 & 128 & 0 \\ -2 & 50 & -400 & 1120 & -1280 & 512 \end{bmatrix}.$$

For the Petrov–Galerkin formulations, a second set of shape functions (for the test space) must be created, namely

$$\psi_n(r) = e^{ik(r-r_a)} \tilde{Q}_n\left(\frac{r_a}{r}\right), \quad n = 1, \dots, N \quad (35)$$

using

$$\tilde{Q}_n(x) = \sum_{\tilde{n}=1}^N \tilde{D}_{n\tilde{n}} x^{\tilde{n}+2} \quad (36)$$

where it is natural to choose $\tilde{D}_{n\tilde{n}} = D_{n\tilde{n}}$. The Bubnov–Galerkin formulations use the same shape functions for the test space, i.e., $\psi_n = \phi_n$.

Alternatively, the polynomials Q can be based upon the Bernstein basis of order $\check{p} = N - 1$ by

$$Q_m(x) = x b_{p-m+1, \check{p}}(x) \quad m = 1, \dots, N \quad (37)$$

where

$$b_{i, \check{p}}(x) = \binom{\check{p}}{i} (1-x)^{\check{p}-i} x^i = \sum_{j=0}^{\check{p}-i} (-1)^j \binom{\check{p}}{i} \binom{\check{p}-i}{j} x^{i+j}, \quad i = 0, \dots, \check{p}. \quad (38)$$

For completeness, note that the coefficients for the radial shape functions used by Burnett [13] (for the Bubnov–Galerkin formulations) can be found by solving $\mathbf{D}\mathbf{B} = \mathbf{E}$ where

$$\mathbf{B} = \begin{bmatrix} x_1 & x_2 & \dots & x_N \\ x_1^2 & x_2^2 & \dots & x_N^2 \\ \vdots & \vdots & \ddots & \vdots \\ x_1^N & x_2^N & \dots & x_N^N \end{bmatrix}, \quad \mathbf{E} = \begin{bmatrix} 1 & & & \\ & e^{ik(r_a-r_2)} & & \\ & & \ddots & \\ & & & e^{ik(r_a-r_N)} \end{bmatrix}, \quad x_n = \frac{r_a}{r_n}.$$

The coefficients $D_{m\tilde{m}}$ are thus given by $\mathbf{D} = \mathbf{E}\mathbf{B}^{-1}$. For Petrov–Galerkin formulations, the coefficients $\tilde{D}_{n\tilde{n}}$ are found in the same way, but now with the matrix

$$\tilde{\mathbf{B}} = \begin{bmatrix} x_1^3 & x_2^3 & \dots & x_N^3 \\ x_1^4 & x_2^4 & \dots & x_N^4 \\ \vdots & \vdots & \ddots & \vdots \\ x_1^{N+2} & x_2^{N+2} & \dots & x_N^{N+2} \end{bmatrix}$$

instead of \mathbf{B} . So with the notation presented, these basis functions are based on the Lagrange polynomials with polynomial order³ $\check{p} = N - 1$

$$l_n(x) = \prod_{\substack{0 \leq n \leq \check{p} \\ n \neq m}} \frac{x - x_n}{x_m - x_n}, \quad (39)$$

³The usage of a check sign above the polynomial order p is to avoid ambiguity between the polynomial order and the scattered pressure.

since the polynomials Q_m can be written as

$$Q_m(x) = e^{ik(r_a - r_m)} \frac{r_m}{r_a} x l_m(x)$$

such that

$$\phi_m(r) = e^{ik(r - r_m)} \frac{r_m}{r} l_m\left(\frac{r_a}{r}\right).$$

The radial shape functions in the test space for the Petrov–Galerkin formulations take the form

$$\psi_n(r) = e^{ik(r - r_n)} \left(\frac{r_n}{r}\right)^3 l_n\left(\frac{r_a}{r}\right).$$

As all these sets of basis functions span the same space, they should only affect the conditioning of the system. Note that the sets of basis functions are identical for $N = 1$.

The trial- and test functions now take the form

$$p_h(\mathbf{x}) = \begin{cases} \sum_{J \in \kappa_a} \sum_{m=1}^N d_{m,J} \phi_m(r) R_J(\xi, \eta, \zeta) \Big|_{\Gamma_a} & \mathbf{x} \in \Omega_a^+ \\ \sum_{J \in \kappa} d_{1,J} R_J(\xi, \eta, \zeta) & \mathbf{x} \in \Omega_a \end{cases} \quad (40)$$

and

$$q_h(\mathbf{x}) = \begin{cases} \sum_{I \in \kappa_a} \sum_{n=1}^N c_{n,I} \psi_n(r) R_I(\xi, \eta, \zeta) \Big|_{\Gamma_a} & \mathbf{x} \in \Omega_a^+ \\ \sum_{I \in \kappa} c_{1,I} R_I(\xi, \eta, \zeta) & \mathbf{x} \in \Omega_a, \end{cases} \quad (41)$$

respectively. Here, κ is the collection of the global indices of the NURBS basis functions and κ_a the corresponding indices of the non-zero NURBS function at the surface Γ_a . Moreover, $R_I(\xi, \eta, \zeta)$ is the set of NURBS basis functions. The system of equations will now be obtained by inserting the functions in Eq. (40) and Eq. (41) into the bilinear form (or sesquilinear form for the BGC and PGC formulations, i.e. the bilinear form with conjugated test functions).

Before the insertion, it is advantageous to split the bilinear form in Eq. (28) as

$$B_{\text{uc}}(q, p) = B_a(q, p) + B_{\text{uc},a}^+(q, p) \quad (42)$$

where

$$B_a(q, p) = \int_{\Omega_a} [\nabla q \cdot \nabla p - k^2 qp] \, d\Omega$$

$$B_{\text{uc},a}^+(q, p) = \lim_{\gamma \rightarrow \infty} \left(\int_{\Omega_a^\gamma} [\nabla q \cdot \nabla p - k^2 qp] \, d\Omega - \int_{S^\gamma} q \partial_n p \, d\Gamma \right). \quad (43)$$

Insertion of Eq. (40) and Eq. (41) into Eq. (27) (using the splitting in Eq. (42)) results in the following system of equations

$$(\mathbf{A}_a + \mathbf{A}_{\text{uc},a}^+) \mathbf{d} = \mathbf{F} \quad (44)$$

with components

$$\begin{aligned} \mathbf{A}_a[I, J] &= B_a(R_I, R_J) & I, J &= 1, \dots, |\kappa| \\ \mathbf{F}[I] &= L(R_I) & I &= 1, \dots, |\kappa| \\ \mathbf{d}[J] &= d_{1,J} & J &= 1, \dots, |\kappa| \end{aligned}$$

and

$$\begin{aligned}\mathbf{A}_{\text{uc,a}}^+[\tilde{I}, \tilde{J}] &= B_{\text{uc,a}}^+(R_I \psi_n, R_J \phi_m) \\ \mathbf{d}[\tilde{J}] &= d_{m,J}\end{aligned}$$

where $I = \kappa_a[\tilde{i}]$ and $J = \kappa_a[\tilde{j}]$ for $\tilde{i}, \tilde{j} = 1, \dots, |\kappa_a|$ and $m, n = 1, \dots, N$, and

$$\begin{aligned}\tilde{I} &= \begin{cases} \kappa_a[\tilde{i}] & n = 1 \\ |\kappa| + (n-2)|\kappa_a| + \tilde{i} & n > 1 \end{cases} \\ \tilde{J} &= \begin{cases} \kappa_a[\tilde{j}] & m = 1 \\ |\kappa| + (m-2)|\kappa_a| + \tilde{j} & m > 1. \end{cases}\end{aligned}$$

Note that \mathbf{A}_a and \mathbf{F} are independent of the IEM and that there are $|\kappa| + |\kappa_a|(N-1)$ linear equations. The matrices are assembled as in the classical FEM. That is, instead of looping through the indices, one loops through the elements. A formula for $B_{\text{uc,a}}^+(R_I \psi_n, R_J \phi_m)$ for the Petrov Galerkin formulation is derived in Appendix A and the final bilinear form is given in Eq. (A.19). The final formulas for the other three formulations are also added in this appendix.

2.3. Far field pattern

The problem is solved inside an artificial boundary, computing the so-called near field. However, the far field is also often of interest. To solve this issue, one uses the integral solution given by⁴ (cf. [18, Theorem 2.21])

$$p(\mathbf{x}) = \int_{\Gamma_1} \left[p(\mathbf{y}) \frac{\partial \Phi_k(\mathbf{x}, \mathbf{y})}{\partial n(\mathbf{y})} - \Phi_k(\mathbf{x}, \mathbf{y}) \frac{\partial p(\mathbf{y})}{\partial n(\mathbf{y})} \right] d\Gamma(\mathbf{y}) \quad (45)$$

where \mathbf{y} is a point on the surface Γ_1 , n lies on Γ_1 pointing ‘‘into’’ Ω^+ at \mathbf{y} and Φ_k is the free space Green’s function for the Helmholtz equation in Eq. (2) given (in 3D) by

$$\Phi_k(\mathbf{x}, \mathbf{y}) = \frac{e^{ikR}}{4\pi R}, \quad \text{where } R = |\mathbf{x} - \mathbf{y}|. \quad (46)$$

The derivative of both Green’s function and the numerical solution for the pressure is therefore needed

$$\frac{\partial \Phi_k(\mathbf{x}, \mathbf{y})}{\partial n(\mathbf{y})} = \frac{\Phi_k(\mathbf{x}, \mathbf{y})}{R} (ikR - 1) \frac{\partial R}{\partial n(\mathbf{y})}, \quad \text{where } \frac{\partial R}{\partial n(\mathbf{y})} = -\frac{(\mathbf{x} - \mathbf{y}) \cdot \mathbf{n}(\mathbf{y})}{R}. \quad (47)$$

Note that for sound-hard scattering (where $\partial_n(p + p_{\text{inc}}) = 0$) the values for $\partial_n p$ are known at the boundary Γ_1 (given by Eq. (3)). To use the exact expression for the derivative seems to give better results, and is for this reason used in the sound-hard scattering cases when computing the field outside the artificial boundary.

The *far field pattern* for the scattered pressure p , is now defined by

$$p_0(\hat{\mathbf{x}}) = \lim_{r \rightarrow \infty} r e^{-ikr} p(r\hat{\mathbf{x}}), \quad (48)$$

with $r = |\mathbf{x}|$ and $\hat{\mathbf{x}} = \mathbf{x}/|\mathbf{x}|$. Using the limits

$$\lim_{r \rightarrow \infty} r e^{-ikr} \Phi_k(r\hat{\mathbf{x}}, \mathbf{y}) = \frac{1}{4\pi} e^{-ik\hat{\mathbf{x}} \cdot \mathbf{y}} \quad \text{and} \quad \lim_{r \rightarrow \infty} r e^{-ikr} \frac{\partial \Phi_k(r\hat{\mathbf{x}}, \mathbf{y})}{\partial n(\mathbf{y})} = -\frac{ik}{4\pi} e^{-ik\hat{\mathbf{x}} \cdot \mathbf{y}} \hat{\mathbf{x}} \cdot \mathbf{n}(\mathbf{y}) \quad (49)$$

⁴For the conjugated formulations one may also compute the far field using the radial shape functions in the infinite elements, but for the unconjugated formulations it is mentioned in [34, p. 137] that the expansion does not converge in the far field, such that it must be computed by other means.

the formula in Eq. (45) simplifies in the far field to (cf. [30, p. 32])

$$p_0(\hat{\mathbf{x}}) = -\frac{1}{4\pi} \int_{\Gamma_1} \left[ikp(\mathbf{y})\hat{\mathbf{x}} \cdot \mathbf{n}(\mathbf{y}) + \frac{\partial p(\mathbf{y})}{\partial n(\mathbf{y})} \right] e^{-ik\hat{\mathbf{x}} \cdot \mathbf{y}} d\Gamma(\mathbf{y}). \quad (50)$$

From the far field pattern, the *target strength*, TS, can be computed. It is defined by

$$\text{TS} = 20 \log_{10} \left(\frac{|p_0(\hat{\mathbf{x}})|}{|P_{\text{inc}}|} \right) \quad (51)$$

where P_{inc} is the amplitude of the incident wave at the geometric center of the scatterer (i.e. the origin). Note that TS is independent of P_{inc} , which is a result of the linear dependency of the amplitude of the incident wave in scattering problems (i.e. doubling the amplitude of the incident wave will double the amplitude of the scattered wave).

3. Acoustic-structure interaction

In [30, pp. 13-14] Ihlenburg briefly derives the governing equations for the ASI problem. Building upon this the formulas are generalized to include an interior fluid domain Ω^- . The pressure in the exterior and interior fluid domain are now denoted by p_1 and p_2 (see Figure 3).

$$\nabla^2 p_1 + k_1^2 p_1 = 0 \quad \text{in } \Omega^+ \quad (52)$$

$$\frac{\partial p(\mathbf{x}, \omega)}{\partial r} - ikp(\mathbf{x}, \omega) = o(r^{-1}) \quad \text{with } r = |\mathbf{x}| \quad (53)$$

$$\rho_{f,1}\omega^2 u_i n_i - \frac{\partial p_1}{\partial n} = \frac{\partial p_{\text{inc}}}{\partial n} \quad \text{on } \Gamma_1 \quad (54)$$

$$\sigma_{ij} n_i n_j + p_1 = -p_{\text{inc}} \quad \text{on } \Gamma_1 \quad (55)$$

$$\sigma_{ij,j} + \omega^2 \rho_s u_i = 0 \quad \text{in } \Omega_s \quad (56)$$

$$\rho_{f,2}\omega^2 u_i n_i - \frac{\partial p_2}{\partial n} = 0 \quad \text{on } \Gamma_2 \quad (57)$$

$$\sigma_{ij} n_i n_j + p_2 = 0 \quad \text{on } \Gamma_2 \quad (58)$$

$$\nabla^2 p_2 + k_2^2 p_2 = 0 \quad \text{in } \Omega^- \quad (59)$$

The first two equations represent the Helmholtz equation and Sommerfeld conditions, respectively, for the exterior domain. The wave numbers in the exterior and interior fluid domain are denoted by k_1 and k_2 . The elasticity equation in Eq. (56) comes from momentum conservation (Newton's second law), while Eqs. (54), (55), (57) and (58) represent the coupling equations and come from the continuity requirement of the displacement and pressures at the boundaries Γ_m . The final formula is simply the Helmholtz equation for the internal fluid domain. The function p_{inc} represents the incident plane wave in Eq. (6) (in the exterior domain). The mass densities of the solid and the fluid are denoted by ρ_s and ρ_f , respectively, and σ_{ij} represents the stress components as a function of the displacement $\mathbf{u} = u_i \mathbf{e}_i$ in the solid.

For the domain of the scatterer, Ω_s , it can be shown that the following weak formulation is obtained from the strong form in Eq. (56) (see for example [30])

$$\int_{\Omega_s} [v_{i,j} \sigma_{ij} - \rho_s \omega^2 u_i \bar{v}_i] d\Omega = \int_{\Gamma_1} v_i (\sigma_{ij} n_j) d\Gamma + \int_{\Gamma_2} v_i (\sigma_{ij} n_j) d\Gamma. \quad (60)$$

where the normal vectors point out of Ω_s . The integrands on the right-hand side may be rewritten using Eqs. (55) and (58) in the following way. Consider a point \mathbf{P} on Γ_1 or Γ_2 , with normal vector $\mathbf{n} = n_i \mathbf{e}_i$. Let T_i be the components (in Cartesian coordinates) of the exterior traction vector \mathbf{T} . That is to say, $T_i = \sigma_{ij} n_j$. One can then create a local orthogonal coordinate system at this point with unit vectors \mathbf{e}_\perp , $\mathbf{e}_{\parallel 1}$ and $\mathbf{e}_{\parallel 2}$,

where the latter two vectors represent basis vectors for the tangential plane of the surface at \mathbf{P} (and \mathbf{e}_\perp represents the normal unit vector on this plane at \mathbf{P}).

As the scalar product is invariant to orthogonal transformations, the following holds

$$T_i v_i = T_x v_x + T_y v_y + T_z v_z = T_\perp v_\perp + T_{\parallel_1} v_{\parallel_1} + T_{\parallel_2} v_{\parallel_2}.$$

Since the acoustic pressure from the fluid only exerts forces normal to the surfaces Γ_1 and Γ_2 , the static equilibrium conditions for the traction at \mathbf{P} are given by

$$T_{\parallel_1} = 0, \quad T_{\parallel_2} = 0, \quad \text{and} \quad T_\perp = -p_{\text{tot},m},$$

where the total pressure is given by

$$p_{\text{tot},m} = \begin{cases} p_{\text{inc}} + p_1 & m = 1 \\ p_2 & m = 2. \end{cases}$$

The scalar product may therefore be written as

$$T_i v_i = -p_{\text{tot},m} v_\perp = -p_{\text{tot},m} v_i n_i.$$

Eq. (60) can thus be rewritten as

$$\int_{\Omega_s} [v_{i,j} \sigma_{ij} - \rho_s \omega^2 u_i v_i] d\Omega = - \int_{\Gamma_1} (p_{\text{inc}} + p_1) v_i n_i d\Gamma - \int_{\Gamma_2} p_2 v_i n_i d\Gamma. \quad (61)$$

Moreover, from Eq. (19) one obtains

$$\int_{\Omega^+} [\nabla q_1 \cdot \nabla p_1 - k_1^2 q_1 p_1] d\Omega = - \int_{\Gamma_1} q_1 \frac{\partial p_1}{\partial n} d\Gamma$$

and

$$\int_{\Omega^-} [\nabla q_2 \cdot \nabla p_2 - k_2^2 q_2 p_2] d\Omega = - \int_{\Gamma_2} q_2 \frac{\partial p_2}{\partial n} d\Gamma$$

where the sign of the right-hand side must be changed in order to get a normal vector that points out of Ω_s . Using now Eqs. (54) and (57)

$$\frac{1}{\rho_{f,1} \omega^2} \int_{\Omega^+} [\nabla q_1 \cdot \nabla p_1 - k_1^2 q_1 p_1] d\Omega = - \int_{\Gamma_1} q_1 \left(u_i n_i - \frac{1}{\rho_{f,1} \omega^2} \frac{\partial p_{\text{inc}}}{\partial n} \right) d\Gamma \quad (62)$$

and

$$\frac{1}{\rho_{f,2} \omega^2} \int_{\Omega^-} [\nabla q_2 \cdot \nabla p_2 - k_2^2 q_2 p_2] d\Omega = - \int_{\Gamma_2} q_2 u_i n_i d\Gamma. \quad (63)$$

Adding Eqs. (61) to (63)

$$\begin{aligned} & \frac{1}{\rho_{f,1} \omega^2} \int_{\Omega^+} [\nabla q_1 \cdot \nabla p_1 - k_1^2 q_1 p_1] d\Omega + \int_{\Gamma_1} [q_1 u_i n_i + p_1 v_i n_i] d\Gamma + \int_{\Omega_s} [v_{i,j} \sigma_{ij} - \rho_s \omega^2 u_i v_i] d\Omega \\ & + \frac{1}{\rho_{f,2} \omega^2} \int_{\Omega^-} [\nabla q_2 \cdot \nabla p_2 - k_2^2 q_2 p_2] d\Omega + \int_{\Gamma_2} [q_2 u_i n_i + p_2 v_i n_i] d\Gamma = \int_{\Gamma_1} \left[\frac{1}{\rho_{f,1} \omega^2} q_1 \frac{\partial p_{\text{inc}}}{\partial n} - p_{\text{inc}} v_i n_i \right] d\Gamma \end{aligned}$$

where $\mathbf{n} = \{n_1, n_2, n_3\}$ points outwards from the solid. Defining the Sobolev spaces $\mathcal{H}_w = \mathcal{S} \times H_w^{1+}(\Omega^+) \times H^1(\Omega^-)$ and $\mathcal{H}_{w^*} = \mathcal{S} \times H_w^{1*}(\Omega^+) \times H^1(\Omega^-)$ where $\mathcal{S} = \{\mathbf{u} : u_i \in H^1(\Omega_s)\}$, the weak formulation for the ASI problem then becomes (with the notation $U = \{\mathbf{u}, p_1, p_2\}$ and $V = \{\mathbf{v}, q_1, q_2\}$):

$$\text{Find } U \in \mathcal{H}_w \text{ such that } B_{\text{ASI}}(V, U) = L_{\text{ASI}}(V), \quad \forall V \in \mathcal{H}_{w^*} \quad (64)$$

where

$$B_{\text{ASI}}(V, U) = \frac{1}{\rho_{f,1}\omega^2} \int_{\Omega^+} [\nabla q_1 \cdot \nabla p_1 - k_1^2 q_1 p_1] d\Omega + \int_{\Gamma_1} [q_1 u_i n_i + p_1 v_i n_i] d\Gamma + \int_{\Omega_s} [v_{i,j} \sigma_{ij} - \rho_s \omega^2 u_i v_i] d\Omega \\ + \frac{1}{\rho_{f,2}\omega^2} \int_{\Omega^-} [\nabla q_2 \cdot \nabla p_2 - k_2^2 q_2 p_2] d\Omega + \int_{\Gamma_2} [q_2 u_i n_i + p_2 v_i n_i] d\Gamma$$

and

$$L_{\text{ASI}}(V) = \int_{\Gamma_1} \left[\frac{1}{\rho_{f,1}\omega^2} q_1 \frac{\partial p_{\text{inc}}}{\partial n} - p_{\text{inc}} v_i n_i \right] d\Gamma.$$

Let $\mathcal{S}_h = \{\mathbf{u} : u_i \in \mathcal{V}(\Omega_s)\} \subset \mathcal{S}$ where $\mathcal{V}(\Omega_s)$ is the space spanned by the NURBS basis functions used to parameterize $\mathcal{V}(\Omega_s)$, and correspondingly for $\mathcal{F}_h^- = \{p_2 : p_2 \in \mathcal{V}(\Omega^-)\} \subset H^1(\Omega^-)$. Moreover, define the spaces $\mathcal{H}_{h,w} = \mathcal{S}_h \times \mathcal{F}_{h,w}^+ \times \mathcal{F}_h^-$ and $\mathcal{H}_{h,w^*} = \mathcal{S}_h \times \mathcal{F}_{h,w^*}^+ \times \mathcal{F}_h^-$. The Galerkin formulation for the ASI problem then becomes:

$$\text{Find } U_h \in \mathcal{H}_{h,w} \text{ such that } B_{\text{ASI}}(V_h, U_h) = L_{\text{ASI}}(V_h), \quad \forall V_h \in \mathcal{H}_{h,w^*}. \quad (65)$$

As the bilinear forms treated in this work are not V -elliptic [30, p. 46], they do not induce a well defined energy-norm. For this reason, the energy norm for the fluid domains Ω_a are defined by

$$\|p_1\|_{\Omega_a} = \sqrt{\int_{\Omega_a} |\nabla p_1|^2 + k_1^2 |p_1|^2 d\Omega} \quad \text{and} \quad \|p_2\|_{\Omega^-} = \sqrt{\int_{\Omega^-} |\nabla p_2|^2 + k_2^2 |p_2|^2 d\Omega} \quad (66)$$

and for the solid domain (using Einstein summation convention)

$$\|\mathbf{u}\|_{\Omega_s} = \sqrt{\int_{\Omega_s} u_{(i,j)} c_{ijkl} \bar{u}_{(k,l)} + \rho_s \omega^2 |\mathbf{u}|^2 d\Omega} \quad (67)$$

where

$$u_{(i,j)} = \frac{1}{2} \left(\frac{\partial u_i}{\partial x_j} + \frac{\partial u_j}{\partial x_i} \right)$$

and elastic coefficients expressed in terms of Young's modulus, E , and the Poisson's ratio, ν , as [6, p. 110]

$$c_{ijkl} = \frac{\nu E}{(1+\nu)(1-2\nu)} \delta_{ij} \delta_{kl} + \frac{E}{2(1+\nu)} (\delta_{ik} \delta_{jl} + \delta_{il} \delta_{jk}).$$

The energy norm for the coupled problem with $\Omega = \Omega_a \cup \Omega_s \cup \Omega^-$ is then defined by

$$\|U\|_{\Omega} = \sqrt{\frac{1}{\rho_{f,1}\omega^2} \|p_1\|_{\Omega_a}^2 + \|\mathbf{u}\|_{\Omega_s}^2 + \frac{1}{\rho_{f,2}\omega^2} \|p_2\|_{\Omega^-}^2}. \quad (68)$$

As the unconjugated formulations do not converge in the far field, the norm in the exterior domain is taken over the Ω_a instead of Ω^+ .

4. Numerical examples

Rigid scattering on a sphere and elastic scattering on a spherical shell are investigated in the following. These problems possess analytic solutions [35] and are for this reason often used to verify numerical methods in acoustic scattering, e.g. [14, 30, 36, 31, 37, 38]. The mock shell is analyzed to investigate the infinite element formulations, and we end this section by analyzing a simplified submarine benchmark.

In this work, the test setting is chosen so that the present approach can be compared to other methods. In particular, the scattering on a rigid sphere example found in [36] and the scattering on a spherical shell

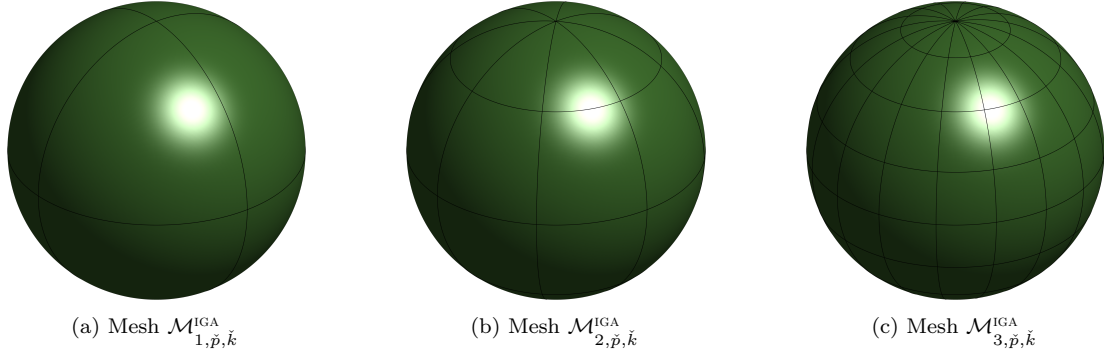


Figure 5: **Numerical examples:** Illustration of the first three meshes, using two successive refinements from the coarse mesh $\mathcal{M}_{1,\check{p},\check{k}}^{\text{IGA}}$.

used in [30] are addressed. The latter problem will be investigated in depth and we shall build upon this problem to include both rigid scattering and scattering with full ASI on both sides of the shell.

The direction of the incident wave is along the x -axis while the symmetry of the parametrization of the domain is around the z -axis (to avoid exploitation of the symmetry of the problems).

We define the *SAV index* by

$$I_{\text{SAV}} = \frac{L_{\Gamma_a}}{2} \frac{|\Gamma_1|}{|\Omega_a|} \quad (69)$$

where L_{Γ_a} is the characteristic length of the artificial boundary, $|\Gamma_1|$ is the surface area of the scatterer and $|\Omega_a|$ is the volume of the discretized fluid between Γ_1 and Γ_a . The SAV index is based on a scaled surface-area-to-volume ratio (SA/V) such that the domain of computation is fitted in a unit sphere. It can be thought of as an efficiency index for the IEM compared to BEM, as problems with low I_{SAV} will be more suited for BEM, while high values of I_{SAV} will be more suited for IEM. If we for the sphere example place the artificial boundary, Γ_a , at $r_a = sR_0$, where R_0 is the outer radius of the scatterer, then the SAV index is given by

$$I_{\text{SAV}} = \frac{3s}{s^3 - 1}. \quad (70)$$

The IEM is optimal for the sphere problem in the sense that the SAV index can be arbitrarily large. In fact, the infinite elements can be attached directly onto the scatterer (such that $I_{\text{SAV}} = \infty$) as done in [33]. This, however, is not the case for more complex geometries. A typical SAV index for submarines like the one depicted in Figure 4 is approximately 5, so by choosing $s > 1$, the SAV index can be adjusted for a fairer comparison with methods like BEM. In the numerical experiments on spherical shells we use $s = \frac{32+\pi}{32-\pi} \approx 1.2$ (such that the aspect ratio of the elements in the tensor product meshes are minimal), resulting in $I_{\text{SAV}} \approx 4.5$.

The meshes will be generated from a standard discretization of a sphere using NURBS as seen in Figure 5. We shall denote by $\mathcal{M}_{m,\check{p},\check{k}}^{\text{IGA}}$ mesh number m with polynomial order \check{p} and continuity \check{k} across element boundaries⁵. For the corresponding FEM meshes we denote by $\mathcal{M}_{m,\check{p},s}^{\text{FEM}}$ and $\mathcal{M}_{m,\check{p},i}^{\text{FEM}}$ the subparametric and isoparametric FEM meshes, respectively. The construction of NURBS meshes are illustrated in Figure 5. The initial mesh is depicted as mesh $\mathcal{M}_{1,\check{p},\check{k}}^{\text{IGA}}$ in Figure 5a and is refined only in the angular directions for the first 3 refinements (that is, mesh $\mathcal{M}_{4,\check{p},\check{k}}^{\text{IGA}}$ only have one element thickness in the radial direction). Mesh $\mathcal{M}_{m,\check{p},\check{k}}^{\text{IGA}}$, $m = 5, 6, 7$, have 2, 4 and 8 elements in its thickness, respectively. This is done to obtain low aspect ratios for the elements. All the meshes will then be nested and the refinements are done uniformly. We shall use the same polynomial order in all parameter directions; $\check{p}_\xi = \check{p}_\eta = \check{p}_\zeta$. Finally, unless otherwise stated, we shall use the BGU formulation and $N = 4$ basis functions in the radial direction of the infinite elements.

⁵Except for some possible C^0 lines in the initial CAD geometry.

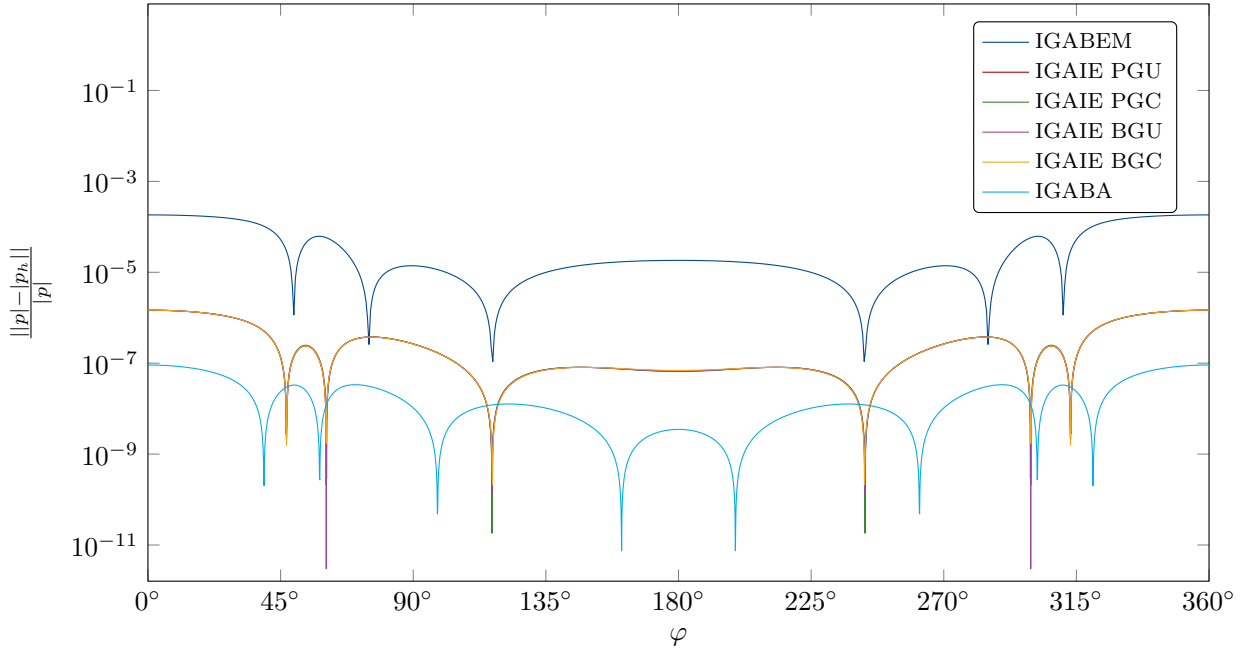


Figure 6: **Simpson benchmark**: The relative error in the modulus of the pressure is plotted on a circle (azimuth direction, φ) in the xy -plane at $r = 5$ m. All simulations were computed on mesh $\mathcal{M}_{3,3,2}^{\text{IGA}}$. The IGAIE formulations here produce roughly the same result.

4.1. Simpson benchmark

The configuration presented by Simpson et al. [36] is considered: a rigid sphere of radius $R_0 = 0.5$ m is impinged by an incident plane wave and the total pressure is measured at a distance $r = 5$ m from the origin. This is a low frequency problem with $k = 2 \text{ m}^{-1}$. It is emphasized that the trace of the NURBS discretization of the domain Ω_a at the surface Γ_1 reduces to the exact same NURBS discretization used in [36] to discretize the boundary Γ_1 . From Figure 6 we observe that the IGA infinite element method (IGAIE) exploits the available degrees of freedom at Γ_1 more effectively than the IGA boundary element method (IGABEM) in [36]⁶. By projecting the analytic solution onto this set of NURBS basis functions at Γ_1 (the best approximation in the L_2 -norm by least squares projection, IGA best approximation, IGABA), it is revealed that even more accuracy can potentially be made. This is an inherent problem for Galerkin FEM when solving the Helmholtz equation and is related to the pollution effect [39]. All IEM formulations (PGU, PGC, BGU and BGC) gave approximately the same result in this case.

4.2. Ihlenburg benchmark

Three benchmark solutions based on the model problem after Ihlenburg [30, p. 191] with parameters given in Table 1, are investigated. The parameters for the fluid domains are the speed of sound in water c_f and the fluid density ρ_f , and the parameters for the solid domain are the Young's modulus, E , the Poisson's ratio ν and the solid density ρ_s . The first benchmark is a simple rigid scattering case (with sound-hard boundary conditions, SHBC) on a sphere with radius R_0 . The second benchmark problem on a spherical shell has ASI conditions at the outer radius, R_0 , and homogeneous Neumann condition at the inner radius, R_1 (sound-soft boundary conditions, SSBC). This case can be thought of as an approximation of a scattering problem on a spherical shell with an internal fluid with very low density. The third and final benchmark is a further extension with ASI conditions on both sides of the spherical shell (Neumann-Neumann conditions on

⁶Due to low resolution of the plots in [36, Fig. 17], the results was reproduced and sampled at 3601 points (rather than 30 points) using our own IGABEM implementation.

Table 1: **Ihlenburg benchmark:** Parameters for the Ihlenburg benchmark problems.

Parameter	Description
$P_{\text{inc}} = 1 \text{ Pa}$	Amplitude of incident wave
$E = 2.07 \cdot 10^{11} \text{ Pa}$	Young's modulus
$\nu = 0.3$	Poisson's ratio
$\rho_s = 7669 \text{ kg m}^{-3}$	Density of solid
$\rho_f = 1000 \text{ kg m}^{-3}$	Density of water
$c_f = 1524 \text{ m s}^{-1}$	Speed of sound in water
$R_0 = 5.075 \text{ m}$	Outer radius
$R_1 = 4.925 \text{ m}$	Inner radius

both surfaces of the shell, NNBC). All of these benchmarks have analytic solutions [35] (see Figures 7 and 8), which enables computation of the error in the energy norm. As we use the same parameters in both fluids, we denote the common wave number in these fluids by $k = k_1 = k_2$. For each experiment, we use the same NURBS order everywhere. Denote by $\check{p}_\xi = \check{p}_{\xi,f} = \check{p}_{\xi,s}$ the common NURBS order in the fluid and the solid in the ξ -direction. Similarly $\check{p}_\eta = \check{p}_{\eta,f} = \check{p}_{\eta,s}$ and $\check{p}_\zeta = \check{p}_{\zeta,f} = \check{p}_{\zeta,s}$. Moreover, we denote by $\check{p} = \check{p}_\xi = \check{p}_\eta = \check{p}_\zeta$ the common polynomial orders in all domains.

In order to compare C^0 FEM and IGA on the scattering problem, we shall transform the NURBS mesh to a C^0 FEM mesh. We use the technique described in Appendix D to get an isoparametric B-spline approximation of the geometry (isoparametric FEM). This parametrization will have C^0 continuity at element boundaries and correspondingly G^0 continuity of the geometry representation (i.e. with kinks). The geometric approximation error is of one order higher than the finite element approximation of the solution [40], so one could expect the C^0 -IGA meshes (with $\hat{k} = 0$) to produce the same accuracy as the isoparametric FEM meshes of higher order ($\hat{p} \geq 2$). It should be noted that the FEM analysis would then use the Bernstein basis instead of the classical Lagrange basis. However, both of these set of functions spans the same spaces, such that the results should be identical in the absence of round-off errors.

In Figure 9 we illustrate h -refinement through the error in the energy norm for the first benchmark example (rigid scattering). Predicted convergence rates are not obtained until the aspect ratio of the elements are reduced sufficiently (that is, from mesh \mathcal{M}_4 and onward). By comparing the results of mesh $\mathcal{M}_{m,2,i}^{\text{FEM}}$ and mesh $\mathcal{M}_{m,2,0}^{\text{IGA}}$ it can be concluded that the geometry error of mesh $\mathcal{M}_{m,2,i}^{\text{FEM}}$ has almost no impact on the accuracy. However, when using maximum continuity, we get significantly better results. Expected convergence rates are visualized in Figure 10 where we now plot the energy norm against λ/h_{max} (corresponding to the number of elements per wave) with λ being the wavelength $\lambda = 2\pi/k$. A key observation is that the number of elements per wave (needed to obtain a given accuracy) is greatly reduced with higher order IGA methods compared to the classical linear FEM (where 10 elements per wavelength is typically desired for engineering precision, [30, p. 182]). The result for the subparametric meshes $\mathcal{M}_{m,2,s}^{\text{FEM}}$ indicates that the convergence rate is reduced due to the reduced accuracy in the geometric representation. This is to be expected as shown in [40, p. 202].

Approaching the ASI problems, we illustrate some meshes in Figure 11 for the full ASI problem. The corresponding meshes for the SSBC problem (with $p_2 = 0$) are obtained by removing the mesh inside the solid domain. In Figures 12 to 17 the target strength, TS, and the error in the energy norm is plotted against the scaled wave number, kR_0 , in all of the three Ihlenburg benchmarks. As each frequency sweep is computed with a different number of degrees of freedom, one should draw the conclusions based on comparing both the accuracy of the results and the related computational costs.

Some data from simulations at $k = 1 \text{ m}^{-1}$ are reported in Table 2 (simulation run with 12 processors of the type Intel(R) Xeon(R) CPU E5-4650 2.70GHz). It should be noted that all simulations were done using the same code, such that the computational time for the FEM simulations can be optimized. However, this is actually the case for the IGA code as well since the implementation does not utilize optimized quadrature rules. The integration is done with $(\check{p} + 1)^3$ quadrature points per element when building the system.

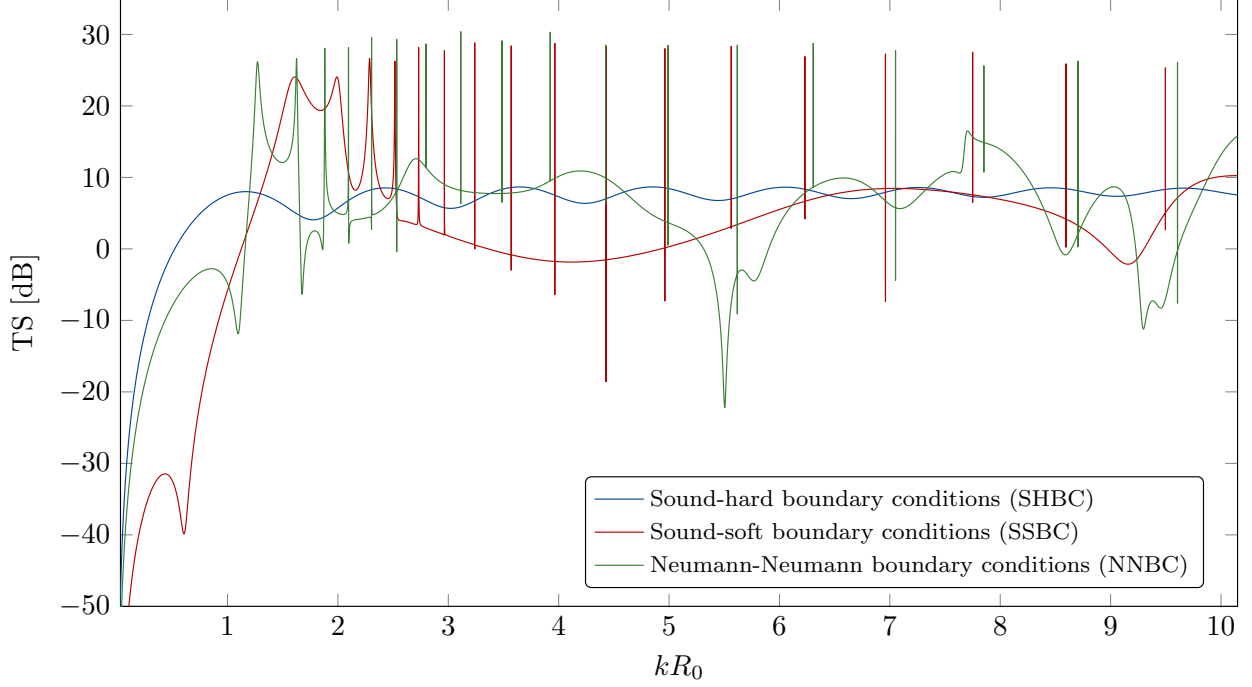


Figure 7: **Ihlenburg benchmark**: Analytic solutions to the scattering problem on a spherical shell with parameters given in Table 1. The far field pattern of backscattered pressure is plotted against the wave number k . A single Neumann condition at the outer radius, R_0 , corresponds to the rigid scattering case with $\mathbf{u} = \mathbf{0}$ and $p_2 = 0$. ASI at R_0 and Neumann at R_1 models $p_2 = 0$. Note that Ihlenburg [30, p. 192] plots the far field pattern in Eq. (48) instead of the target strength, TS, in Eq. (51).

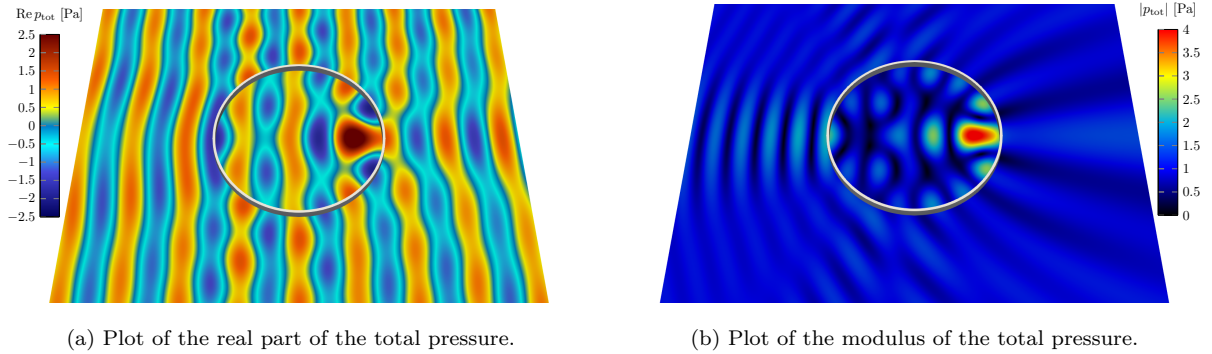


Figure 8: **Ihlenburg benchmark with NNBC**: The analytic solution with ASI at both R_0 and R_1 with $kR_0 = 10.15$ is plotted in the xy -plane. The solid domain is cut open for visualization purposes.

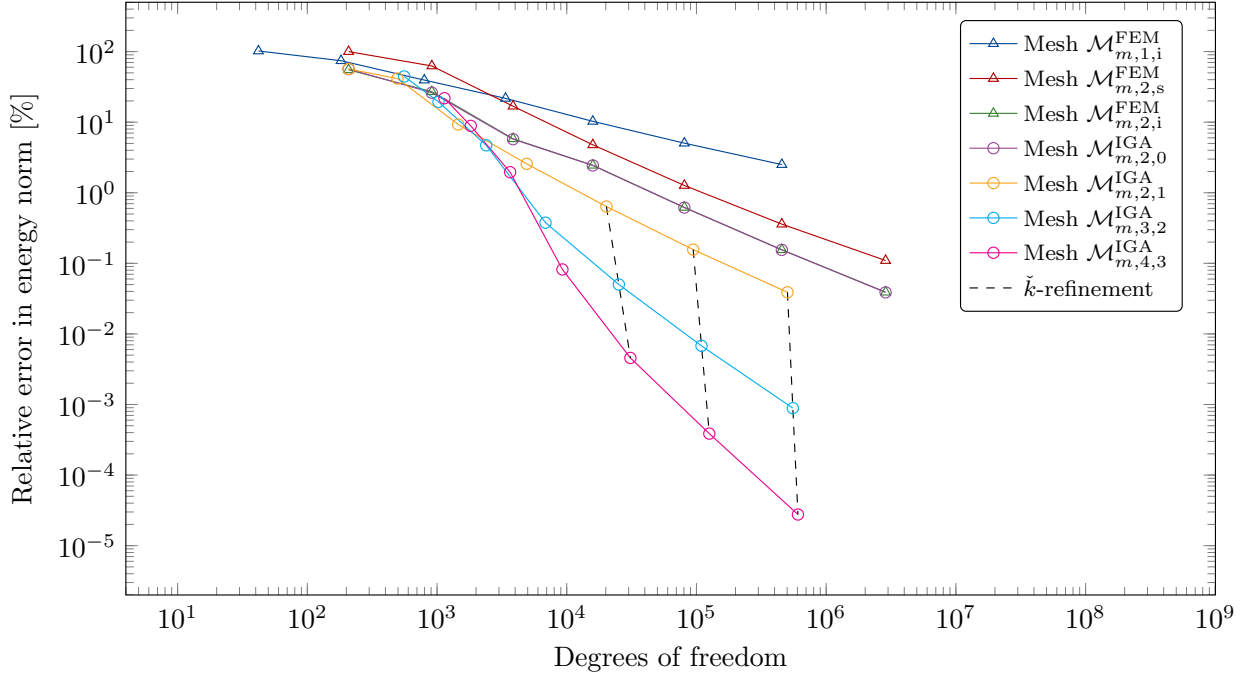


Figure 9: **Ihlenburg benchmark with SHBC**: Convergence analysis on the rigid scattering case with $k = 1 \text{ m}^{-1}$ and mesh \mathcal{M}_m , $m = 1, \dots, 7$, using $N = 6$. The relative energy error (Eq. (66)) is plotted against the degrees of freedom.

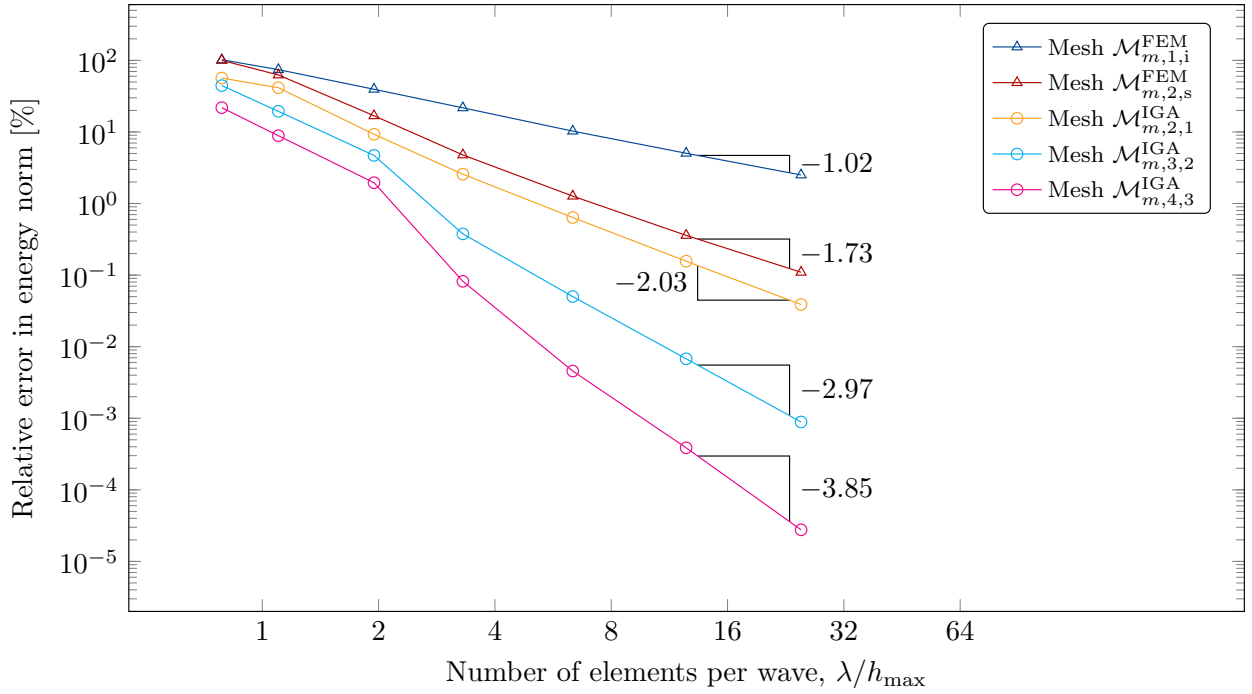


Figure 10: **Ihlenburg benchmark with SHBC**: Convergence analysis on the rigid scattering case with $k = 1 \text{ m}^{-1}$ and mesh \mathcal{M}_m , $m = 1, \dots, 7$, using $N = 6$. The relative energy error (Eq. (66)) is plotted against the number of elements per wave.

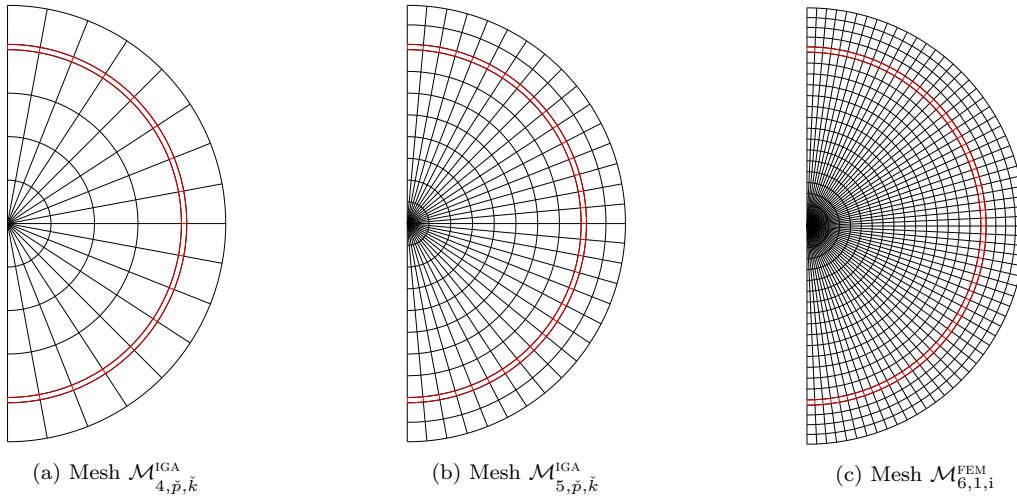


Figure 11: **Ihlenburg benchmark with NNBC**: Illustration of some meshes for the full ASI problem in the xz -plane ($x > 0$), where the mesh lines for the solid domain is colored red. The full mesh is obtained by rotation around the z -axis. Mesh $\mathcal{M}_{5,2,i}^{FEM}$ is visually indistinguishable from $\mathcal{M}_{5,\check{p},\check{k}}^{IGA}$.

For higher order splines spaces this is significantly more quadrature point than what is needed for exact integration (on meshes with affine geometry mapping⁷). In [42, 43], it is shown that the optimal number of quadrature points is half the number of degrees of freedom of the splines space under consideration. That is, the number of quadrature points in the IGA 3D tensor product meshes can be reduced by a factor up to $2^3(\check{p} + 1)^3$ for meshes with maximal continuity. Thus, the efficiency of the IGA simulation may be improved significantly.

A particular interesting observation is that IGA obtains roughly the same accuracy as FEM when the same number of elements is used, even though this corresponds to far less degrees of freedom for the IGA simulation. Moreover, even better result can be obtained with less degrees of freedom if the polynomial degree is increased in the IGA simulations. This, however, only occurs when the mesh resolves the number of waves per element. When the mesh is sufficiently resolved, one order of magnitude improvement in the accuracy is obtained by increasing the polynomial degree. Since another magnitude of accuracy is obtained by the use of higher order elements in FEM/IGA, the IGA offers several orders of magnitude better accuracy than classical linear FEM.

The peaks in the frequency sweeps represent eigenmodes. The quality of the numerical approximation of the corresponding frequencies is reduced for higher frequencies, resulting in fictitious modes. This typically does not pose that much of a problem as the bandwidth of these eigenmodes becomes very small, with a corresponding reduction in the energy they represent. Note that mesh $\mathcal{M}_{4,3,2}^{IGA}$ performs particularly poorly on the partial ASI problem due to a fictitious mode at $k = 1 \text{ m}^{-1}$ for this mesh. The improvement offered by IGA concerning the accuracy in the eigenmodes is investigated in [44].

It should be noted that the meshes used throughout this work are not optimal. This is in particular the case for the full ASI problem where the density of elements becomes large at the origin. These meshes were used as they naturally arise from tensor product NURBS meshes of spherical shells and spheres. One could thus obtain increased performance for the FEM solutions using standard meshing of the domain. However, locally refined meshes can also be obtained with the IGA method, for example using LR B-splines [45].

In Figure 18 we visualize the distribution of the error of the full ASI problem. The error is observed to be largest at element boundaries where the continuity is reduced. Since second order basis functions are

⁷Using the same quadrature scheme on truly isoparametric elements will according to [41, p. 256] give a numerical integration error of the same order as the finite element discretization error. Thus, the argument for optimal quadrature scheme also holds for isoparametric elements as well.

Table 2: **Ihlenburg benchmark**: Data for some simulations on the rigid scattering problem with $k = 1 \text{ m}^{-1}$. The errors are given in the energy norm (Eq. (68)). For each simulation, the mesh number, the polynomial order, \bar{p} , the number of mesh elements n_{el} (not including the infinite elements) and the number of degrees of freedom n_{dof} , is reported. The elapsed times for building the system t_{sys} and for solving the system t_{sol} (using LU-factorization) are also included (times in seconds). Finally, the relative error in the energy norm is given in percentage.

(a) Sound-hard boundary conditions (SHBC).

	n_{el}	n_{dof}	t_{sys} [s]	t_{sol} [s]	Relative energy error [%]
Mesh $\mathcal{M}_{6,1,i}^{\text{FEM}}$	32 768	56 462	7.7	26.5	5.04
Mesh $\mathcal{M}_{5,2,i}^{\text{FEM}}$	4096	56 462	5.1	20.5	0.62
Mesh $\mathcal{M}_{5,2,1}^{\text{IGA}}$	4096	13 476	4.8	4.3	0.64
Mesh $\mathcal{M}_{4,3,2}^{\text{IGA}}$	512	4572	3.1	1.6	0.38
Mesh $\mathcal{M}_{5,3,2}^{\text{IGA}}$	4096	17 654	14.8	8.3	0.05

(b) Sound-soft boundary conditions (SSBC).

	n_{el}	n_{dof}	t_{sys} [s]	t_{sol} [s]	Relative energy error [%]
Mesh $\mathcal{M}_{6,1,i}^{\text{FEM}}$	40 960	104 858	13.7	75.3	7.66
Mesh $\mathcal{M}_{5,2,i}^{\text{FEM}}$	6144	129 056	15.9	106.1	1.35
Mesh $\mathcal{M}_{5,2,1}^{\text{IGA}}$	6144	33 690	13.4	34.7	0.99
Mesh $\mathcal{M}_{4,3,2}^{\text{IGA}}$	1024	13 716	11.8	9.0	41.30
Mesh $\mathcal{M}_{5,3,2}^{\text{IGA}}$	6144	47 918	52.0	69.9	0.09

(c) Neumann-Neumann boundary conditions (NNBC).

	n_{el}	n_{dof}	t_{sys} [s]	t_{sol} [s]	Relative energy error [%]
Mesh $\mathcal{M}_{6,1,i}^{\text{FEM}}$	172 032	233 915	27.8	429.5	6.55
Mesh $\mathcal{M}_{5,2,i}^{\text{FEM}}$	22 528	258 113	31.1	462.7	0.53
Mesh $\mathcal{M}_{5,2,1}^{\text{IGA}}$	22 528	53 905	22.5	64.9	0.71
Mesh $\mathcal{M}_{4,3,2}^{\text{IGA}}$	3072	18 289	17.1	17.3	1.47
Mesh $\mathcal{M}_{5,3,2}^{\text{IGA}}$	22 528	73 139	93.2	145.7	0.05

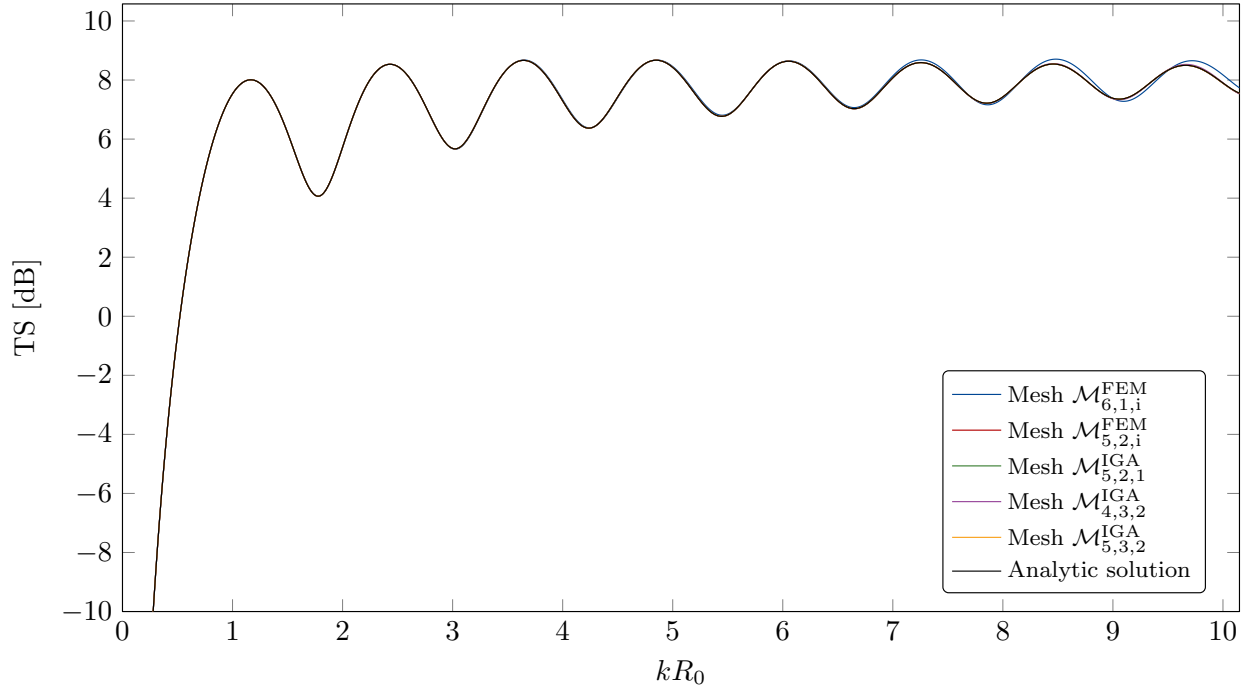


Figure 12: **Ihlenburg benchmark with SHBC**: The target strength (TS) in Eq. (51) is plotted against kR_0 .

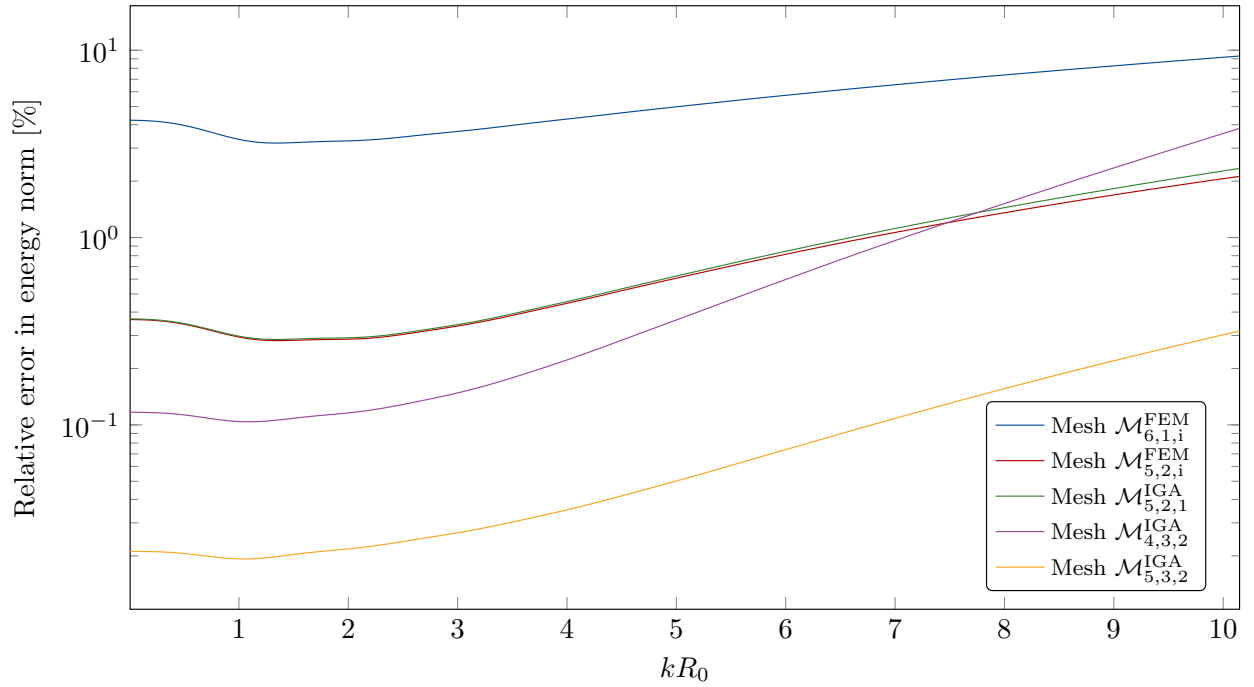


Figure 13: **Ihlenburg benchmark with SHBC**: The relative energy norm (Eq. (68)) is plotted against kR_0 .

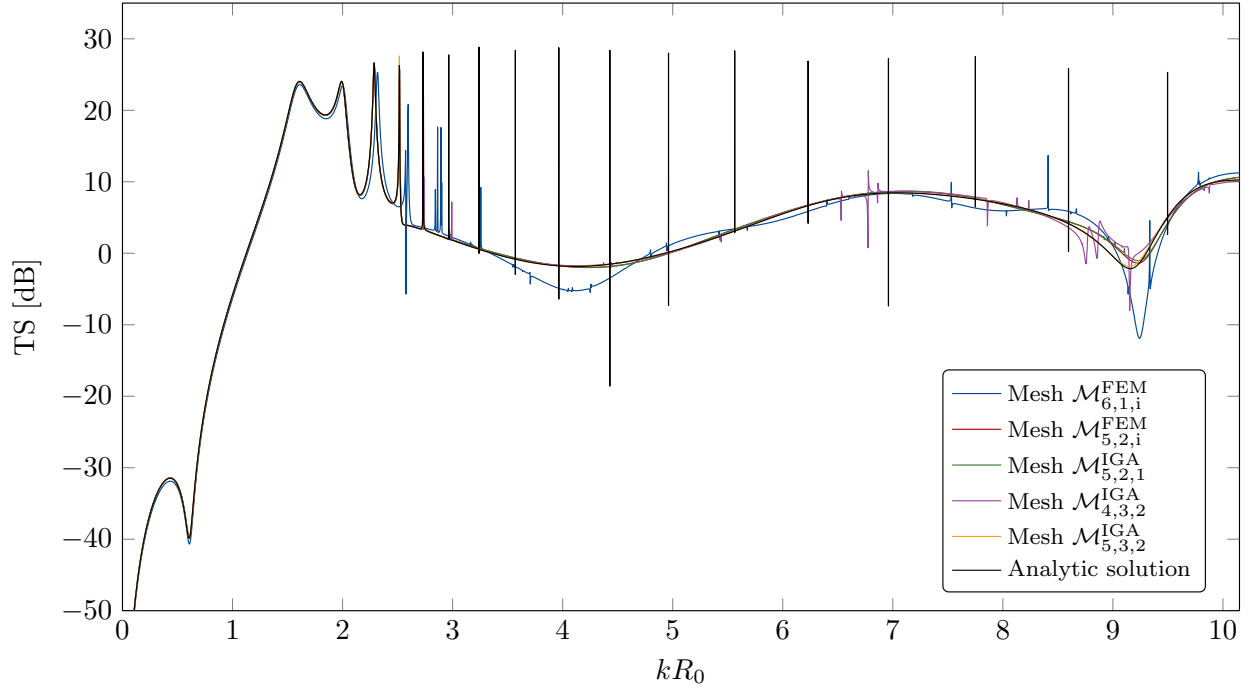


Figure 14: **Ihlenburg benchmark with SSBC**: ASI problem with the internal pressure modeled to be $p_2 = 0$. The target strength (TS) in Eq. (51) is plotted against kR_0 .

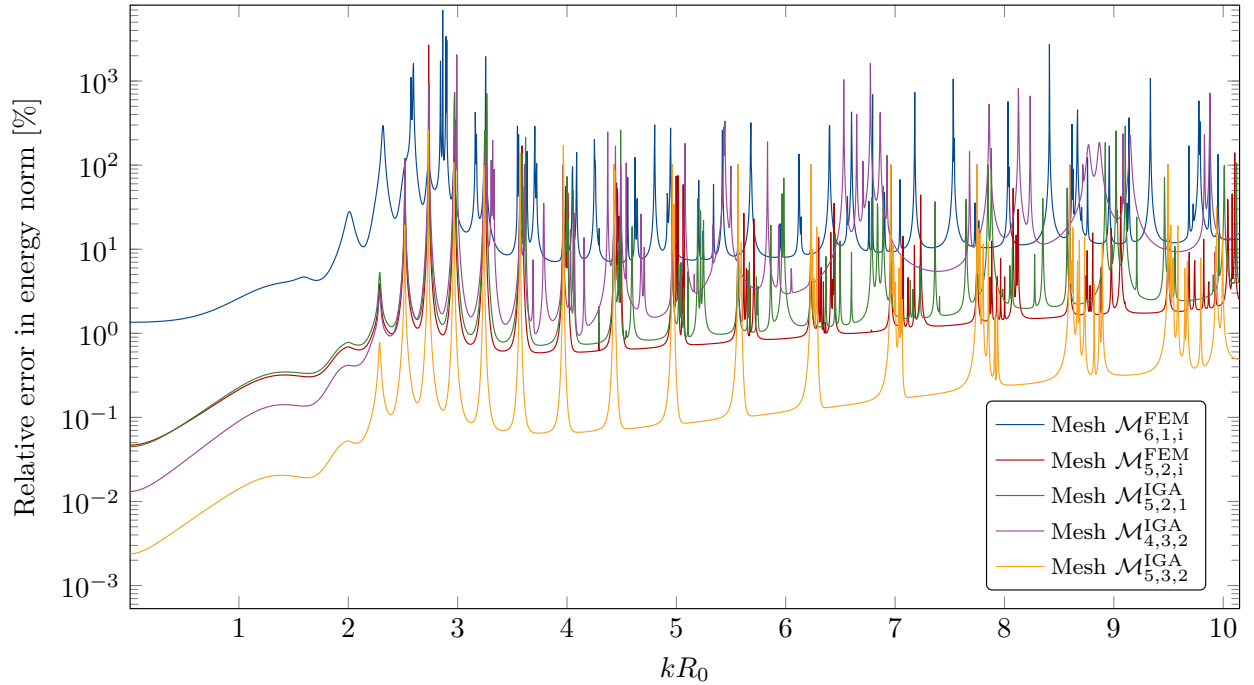


Figure 15: **Ihlenburg benchmark with SSBC**: ASI problem with the internal pressure modeled to be $p_2 = 0$. The relative energy norm (Eq. (68)) is plotted against kR_0 .

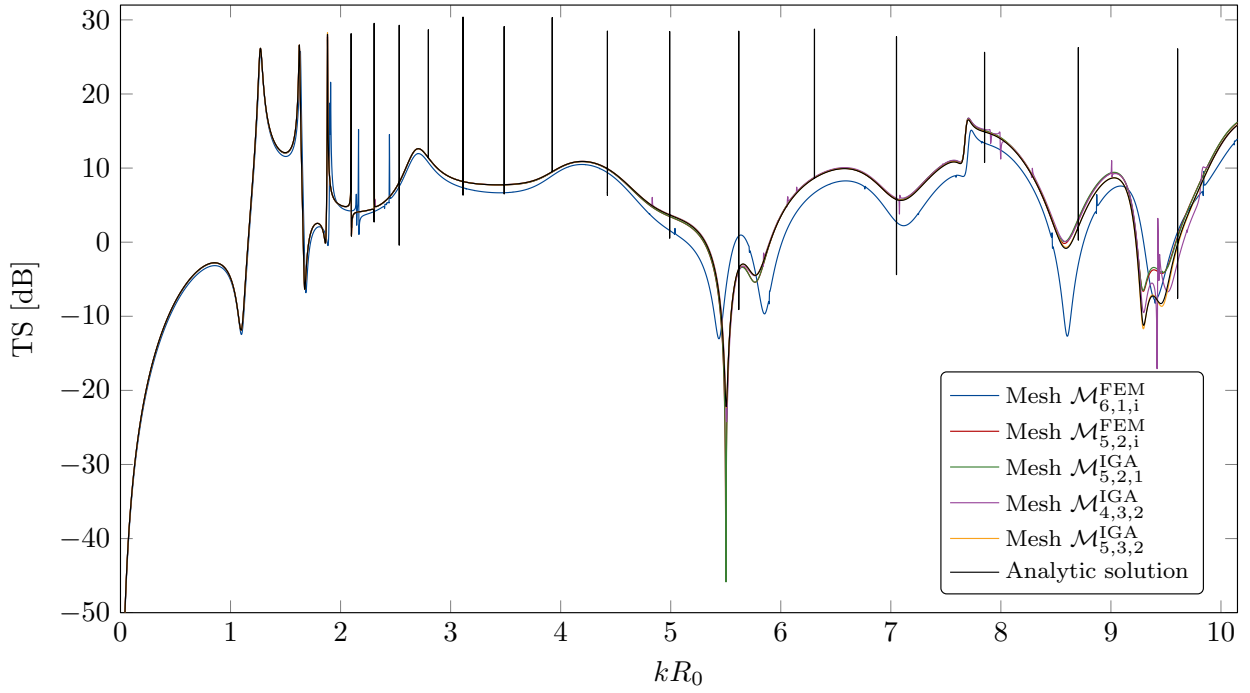


Figure 16: **Ihlenburg benchmark with NNBC**: The target strength (TS) in Eq. (51) is plotted against kR_0 .

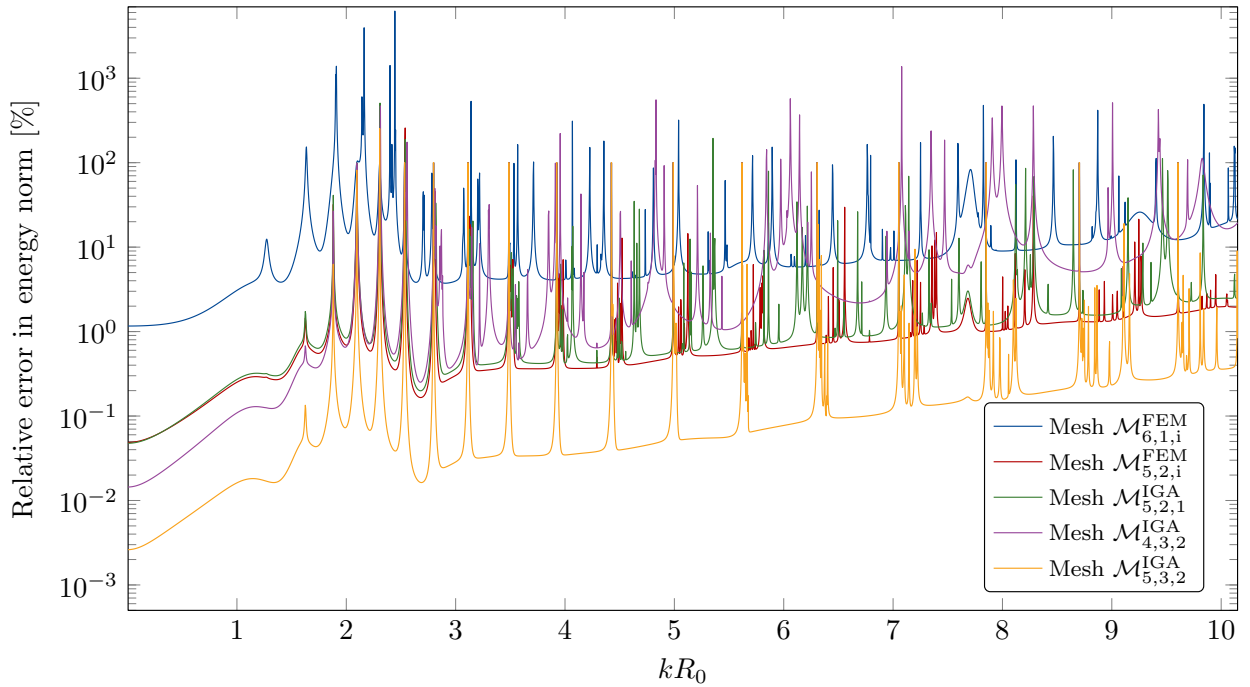


Figure 17: **Ihlenburg benchmark with NNBC**: The relative energy norm (Eq. (68)) is plotted against kR_0 .

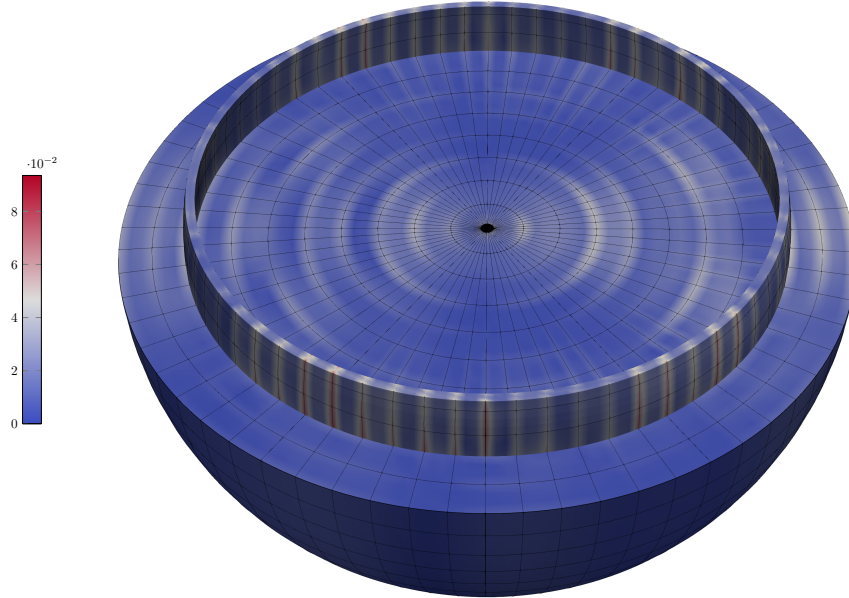


Figure 18: **Ihlenburg benchmark with NNBC**: Simulation of the full ASI problem on mesh $\mathcal{M}_{5,2,1}^{\text{GA}}$. Pointwise evaluation of the square root of the integrand of the volume integrals in the energy norm $\|U - U_h\|_{\Omega}$ in Eq. (68) with $k = 2 \text{ m}^{-1}$ (error in the infinite elements in Ω_a^+ is not shown) is here visualized, where U is the set of analytic solutions in both fluid domains and the solid domain, and U_h is the corresponding numerical solution. The values are scaled by the square root of the maximum of the corresponding integrand values of $\|U\|_{\Omega}$. Both fluid domains are cut open at the xy -plane (at $z = 0$), and the solid domain is cut open at $z = 1.1 \text{ m}$.

used and the error in the velocity/stress dominates the error in the pressure/displacement, the results are in agreement with what was observed in [46], i.e., that the error in the derivative of the primary solution is largest at the element boundaries.

4.3. Radial pulsation from a mock shell

By construction of the fundamental solution of the Helmholtz equation ($\Phi_k(\mathbf{x}, \mathbf{y})$ in Eq. (46)), the function $p(\mathbf{x}) = \Phi_k(\mathbf{x}, \mathbf{y})$ is a solution to Eqs. (2) to (4) whenever $\mathbf{y} \in \mathbb{R}^3 \setminus \overline{\Omega^+}$ and for the Neumann boundary condition $g(\mathbf{x}) = \partial_n \Phi_k(\mathbf{x}, \mathbf{y})$ on Γ_1 . Hence, we have an exact reference solution for the exterior Helmholtz problem for arbitrary geometries Γ_1 which encloses the point \mathbf{y} . It is emphasized that this solution is non-physical for non-spherical geometries Γ_1 . General solutions may be constructed by separation of variables (cf. [30, p. 26])

$$p(\mathbf{x}) = \sum_{n=0}^{\infty} \sum_{m=-n}^n C_{nm} h_n^{(1)}(kR) P_n^{|m|}(\cos \vartheta) e^{im\varphi} \quad (71)$$

with

$$R = |\mathbf{x} - \mathbf{y}|, \quad \vartheta = \arccos\left(\frac{x_3 - y_3}{R}\right), \quad \varphi = \text{atan2}(x_2 - y_2, x_1 - y_1)$$

where $h_n^{(1)}$ is the n^{th} spherical Hankel function of first kind and P_n^m are the associated Legendre functions. In fact, the solution $p(\mathbf{x}) = \Phi_k(\mathbf{x}, \mathbf{y})$ is a special case of this general form with

$$C_{nm} = \begin{cases} \frac{ik}{4\pi} & n = 0, m = 0 \\ 0 & \text{otherwise.} \end{cases} \quad (72)$$

The complexity of this problem setup does not scale with the complexity of the model as it is independent of Γ_1 . However, it preserves two important properties of acoustic scattering, namely the radial decay and the

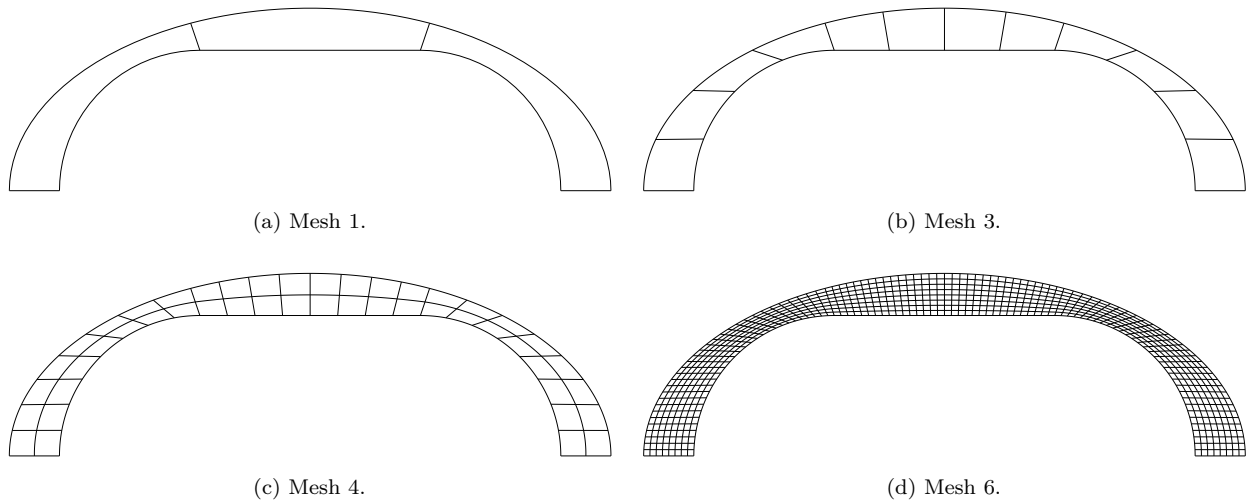


Figure 19: **Radial pulsation from a mock shell**: Meshes for the fluid domain between the scatterer and the artificial boundary. The meshes are constructed from the initial mesh 1, which is rotated around the axis of symmetry using four elements. Mesh 2 and 3 are refined only in the angular direction, while the more refined meshes also refine in the radial direction to obtain smallest aspect ratio. The meshes are nested.

oscillatory nature. Thus, this problem setup represents a general way of constructing manufactured solutions, that can be utilized to verify the correctness of the implemented code for solving the Helmholtz equation. A special case of this general setup is the pulsating sphere example in [36].

From the first limit of Eq. (49), the far field is given by $p_0(\hat{\mathbf{x}}) = \frac{1}{4\pi} e^{-ik\hat{\mathbf{x}}\cdot\mathbf{y}}$. Thus, the target strength is a constant, $TS = -20 \log_{10}(4\pi) \approx -21.984$ (where we define $P_{\text{inc}} = 1 \text{ Pa}$ in Eq. (51) for this problem).

Consider the case $\mathbf{y} = \frac{R_0}{4}(1, 1, 1)$ and the boundary Γ_1 given by a *mock shell* composed of a cylinder with hemispherical endcaps (with axis of symmetry along the x -axis such that the center of the spherical endcaps are located at $x = 0$ and $x = -L$). The cylinder has radius $R_0 = 1 \text{ m}$ and length $L = \frac{\pi}{2}R_0$. The analytic solution is given by

$$p(\mathbf{x}) = \frac{e^{ikR}}{4\pi R}, \quad R = |\mathbf{x} - \mathbf{y}| \quad (73)$$

and the Neumann condition is then

$$g(\mathbf{x}) = \frac{e^{ikR}}{4\pi R^3} (ikR - 1)(\mathbf{x} - \mathbf{y}) \cdot \mathbf{n}(\mathbf{x}). \quad (74)$$

This example is used to illustrate the differences of the infinite element formulations using the prolate ellipsoidal elements after Burnett [13]. The mesh construction is illustrated in Figure 19, and an illustration of the solution is presented in Figure 20. Convergence plots are shown in Figure 21. Gerdes did a similar comparison in [31] where scattering on a sphere was investigated. Our results verify these findings, namely lower errors for the unconjugated formulations (cf. Figure 21). Good results can be obtained using only a single radial shape function in case of unconjugated formulations. For the conjugated versions, on the other hand, $N > 6$ functions are needed to obtain similar accuracy and more degrees of freedom are required to get an asymptotic behavior.

In Figure 22 and Figure 23 the condition number is investigated for the different formulations and basis functions in the radial shape functions. The condition number for the unconjugated versions increases more rapidly as a function of N compared to the corresponding formulations in the conjugated case. The condition number of the Lagrange basis increases particularly fast with N , making it useless⁸ for the conjugated formulations. However, the Lagrange basis yields the best result for the unconjugated formulations for small

⁸In the case of $r_n = nr_a$.

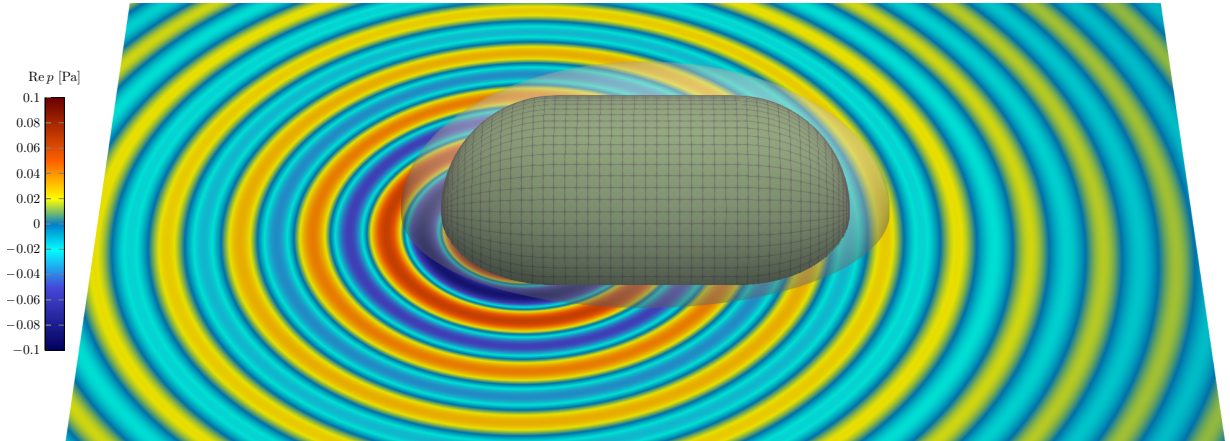


Figure 20: **Radial pulsation from a mock shell:** Visualization of numerical solution in the xy -plane using BGU with $N = 6$ on mesh 5.

N . The Chebyshev basis seems to give the best condition numbers for the conjugated formulations for large N (which is required for acceptable results). The unconjugated formulations perform quite similar, both in terms of the condition numbers and the error. The BGU formulation has the additional advantage of producing symmetric matrices, and reduces the memory requirement. It is clear that the choice of basis functions in the infinite elements plays a crucial role for the condition number, and more research is required to find the optimal set of basis functions. Based on the findings in this work, it is recommended to use the BGU formulation alongside the Lagrange basis (in the radial direction) in the infinite elements. However, if larger N is needed for accuracy, the Chebyshev basis is recommended.

4.4. Stripped BeTSSi submarine

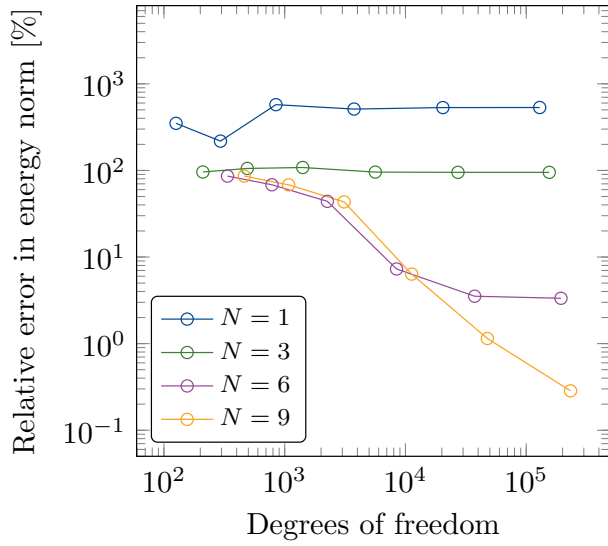
Finally, we consider the *stripped BeTSSi submarine*⁹ described in Appendix C, and let a plane wave, with the direction of incidence given by

$$\mathbf{d}_s = - \begin{bmatrix} \cos \beta_s \cos \alpha_s \\ \cos \beta_s \sin \alpha_s \\ \sin \beta_s \end{bmatrix}, \quad \text{where } \alpha_s = 240^\circ, \beta_s = 0^\circ, \quad (75)$$

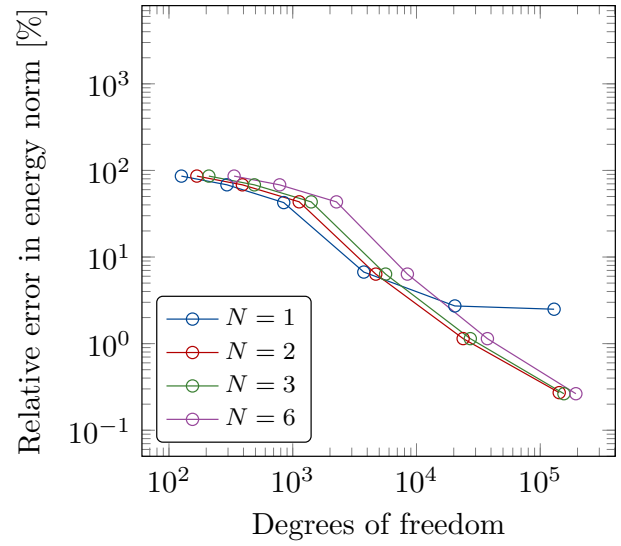
be scattered by this submarine. The CAD model is given in Figure 24 alongside computational meshes. Again, we shall denote by $\mathcal{M}_{m,\check{p},\check{k}}^{\text{IGA}}$, mesh number m with polynomial order \check{p} and continuity \check{k} across element boundaries of the NURBS parametrization.

The near field at $f = 1000$ Hz is visualized in Figure 25. The low frequency problem at $f = 100$ Hz is considered in Figure 26. In this case, mesh $\mathcal{M}_{1,2,1}^{\text{IGA}}$ resolves this frequency, but the solution slightly deviates from the reference solution computed by IGABEM on a fine mesh. The reason for this is that N is too low. Although $N = 3$ was enough for engineering precision (below 1%) in the mock shell example, it does not suffice for the more complicated geometry like the stripped BeTSSi submarine. Consider the relative error for the far field at the well resolved mesh $\mathcal{M}_{2,3,2}^{\text{IGA}}$. In this case the error will originate from the low resolution (governed by N) in the radial direction for the infinite elements. As illustrated in Figure 27 an order of magnitude in accuracy is gained by increasing N . This effect was also observed by the verification test in Section 4.3 applied to the stripped BeTSSi submarine. In Figure 28 the target strength is plotted for $f = 500$ Hz and $f = 1000$ Hz. A reference solution (using IGABEM) is added for the $f = 500$ Hz case, and illustrates again the pollution of low N . The IGA mesh 1 resolves the frequency $f = 500$ Hz quite well using only about 5 elements per wave length. This corresponds to about 5 dofs per wave length in each dimensional direction compared to the classical 10-12 dofs per wave length needed for FEM methods.

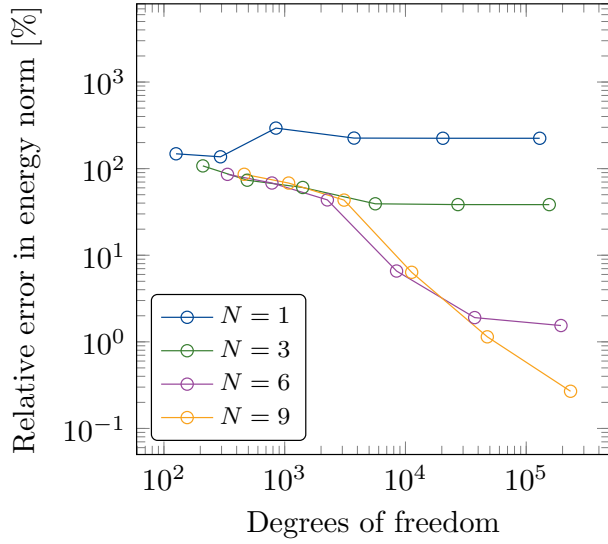
⁹Based upon the BeTSSi submarine which originates from the BeTSSi workshops [1].



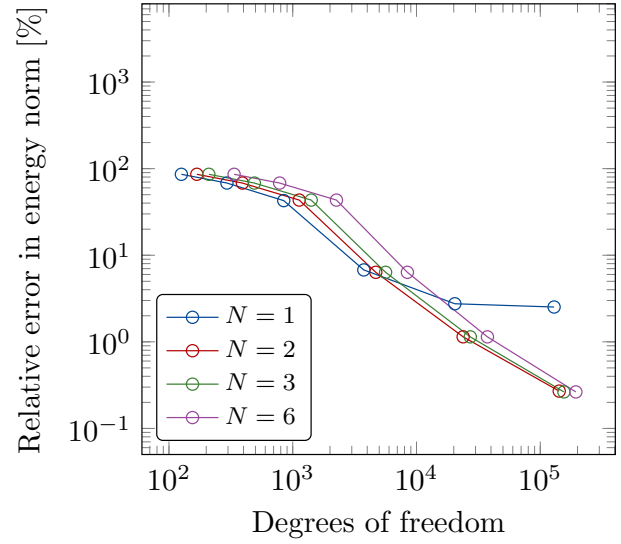
(a) BGC



(b) BGU

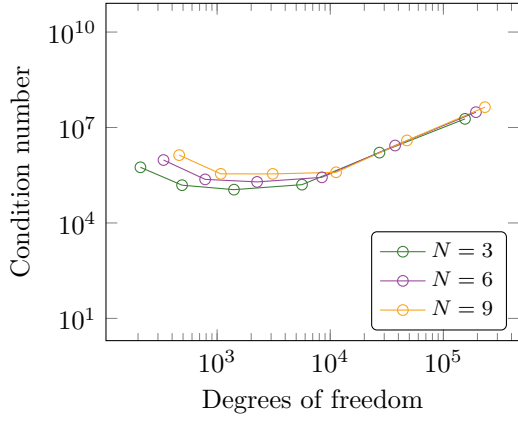


(c) PGC

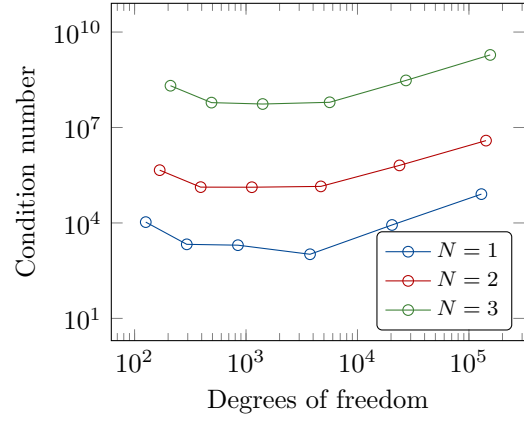


(d) PGU

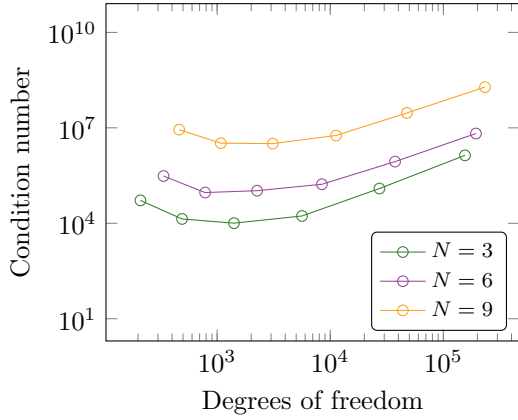
Figure 21: **Radial pulsation from a mock shell**: Convergence plots for the four infinite element formulations. The relative error in the energy norm (Eq. (66)) is plotted against the number of degrees of freedom.



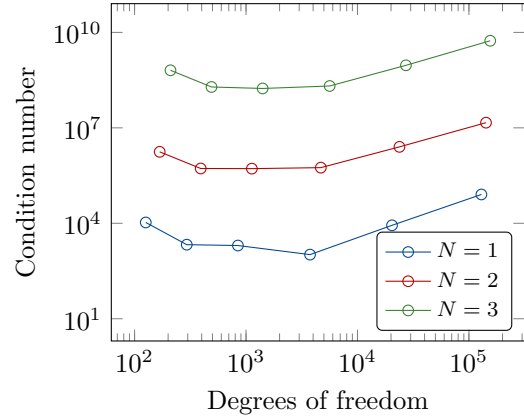
(a) BGC with the shifted Chebyshev basis



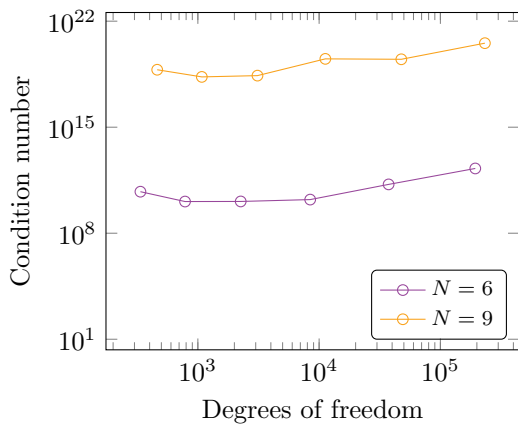
(b) BGU with the shifted Chebyshev basis



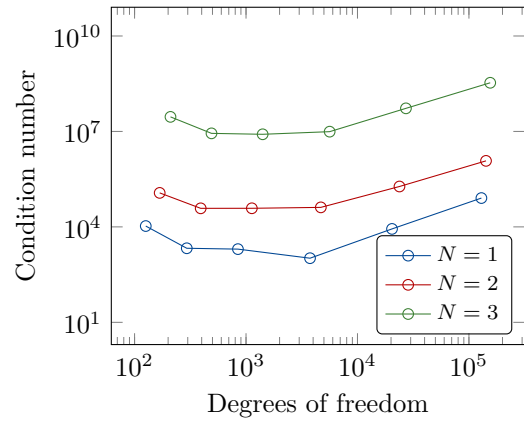
(c) BGC with the Bernstein basis



(d) BGU with the Bernstein basis

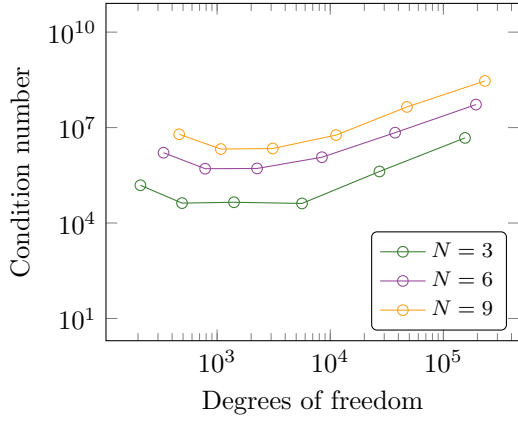


(e) BGC with the Lagrange basis

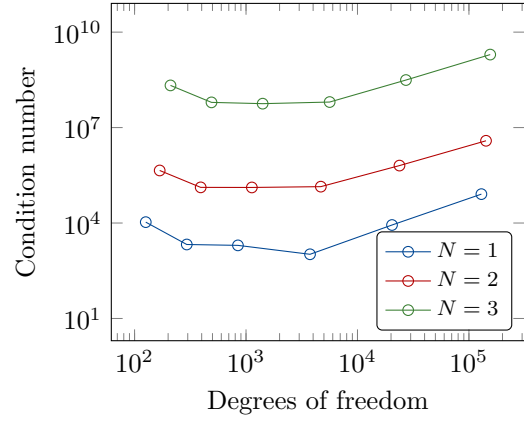


(f) BGU with the Lagrange basis

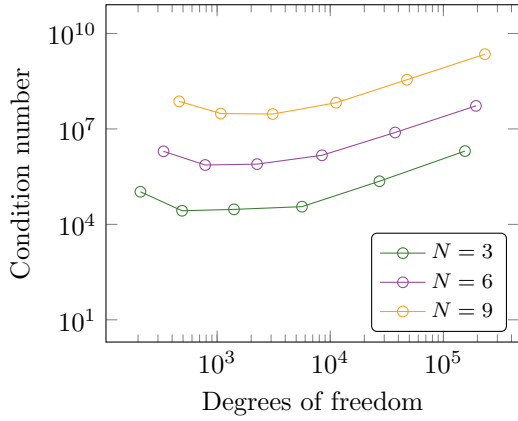
Figure 22: **Radial pulsation from a mock shell**: Convergence plots for the BGC and BGU formulations using three different sets of radial shape functions (Chebyshev, Bernstein and Lagrange). The condition number (1-norm condition number estimate provided by `condst` in MATLAB) is plotted against the number of degrees of freedom.



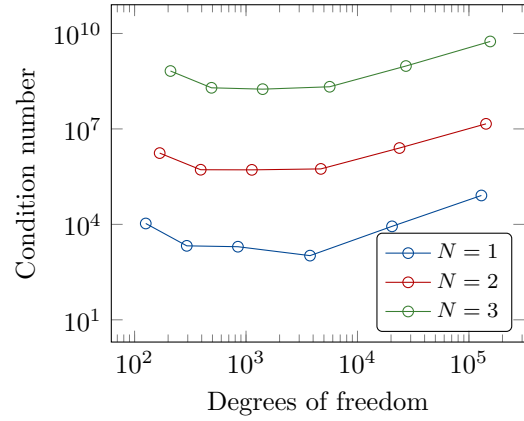
(a) PGC with the shifted Chebyshev basis



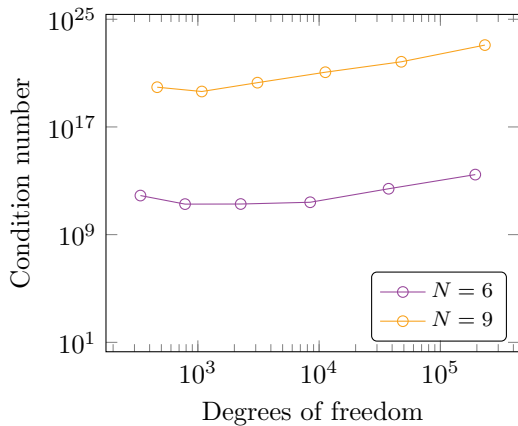
(b) PGU with the shifted Chebyshev basis



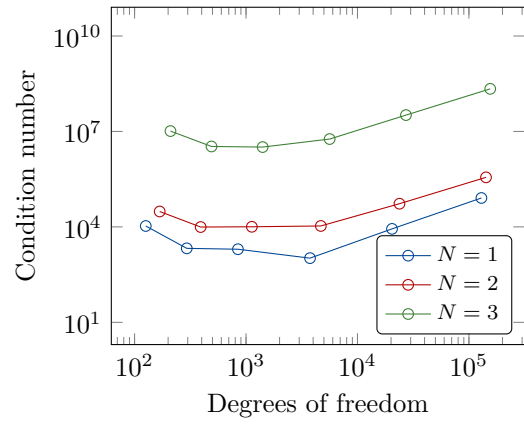
(c) PGC with the Bernstein basis



(d) PGU with the Bernstein basis

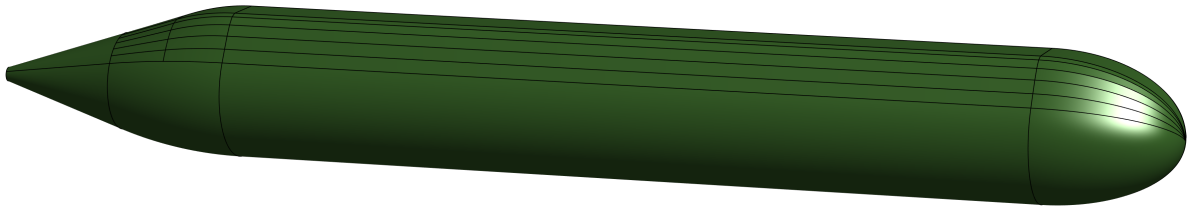


(e) PGC with the Lagrange basis

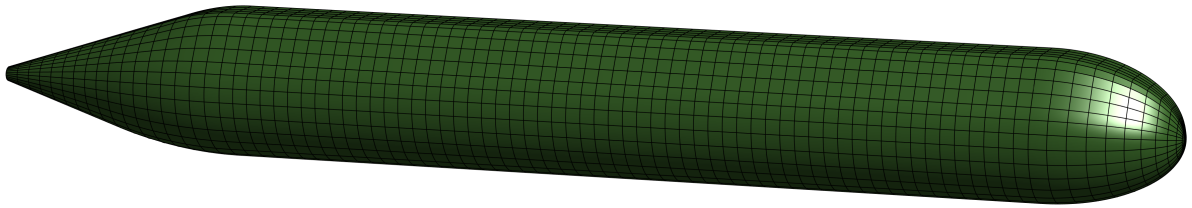


(f) PGU with the Lagrange basis

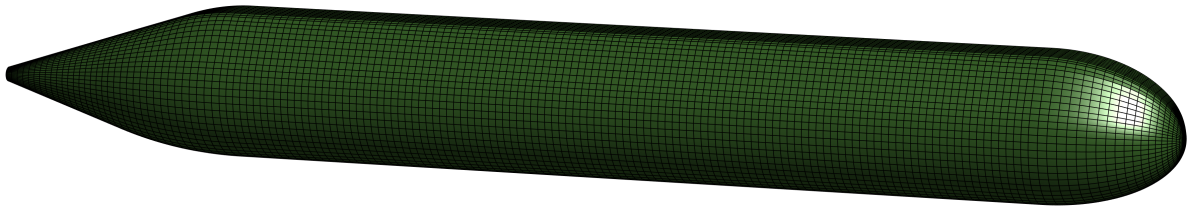
Figure 23: **Radial pulsation from a mock shell**: Convergence plots for the PGC and PGU formulations using three different sets of radial shape functions (Chebyshev, Bernstein and Lagrange). The condition number (1-norm condition number estimate provided by `condst` in MATLAB) is plotted against the number of degrees of freedom.



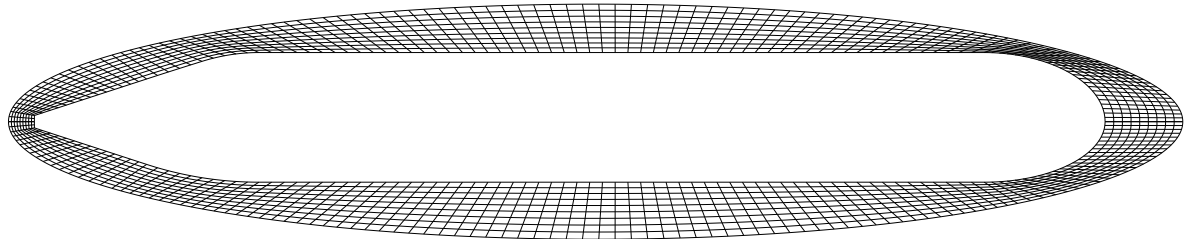
(a) CAD model.



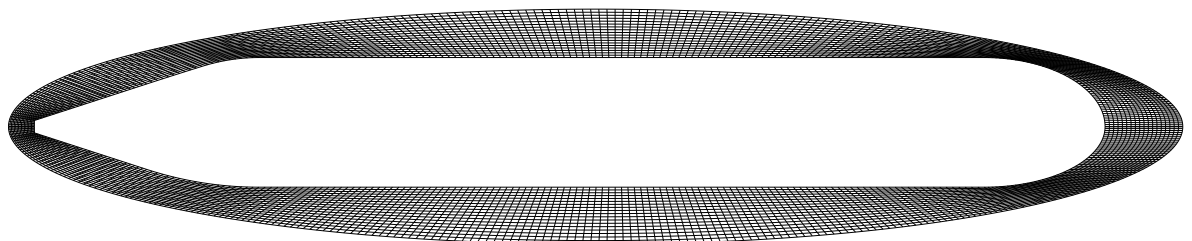
(b) Surface mesh for mesh $\mathcal{M}_{1, \hat{p}, \hat{k}}^{IGA}$.



(c) Surface mesh for mesh $\mathcal{M}_{2, \hat{p}, \hat{k}}^{IGA}$.

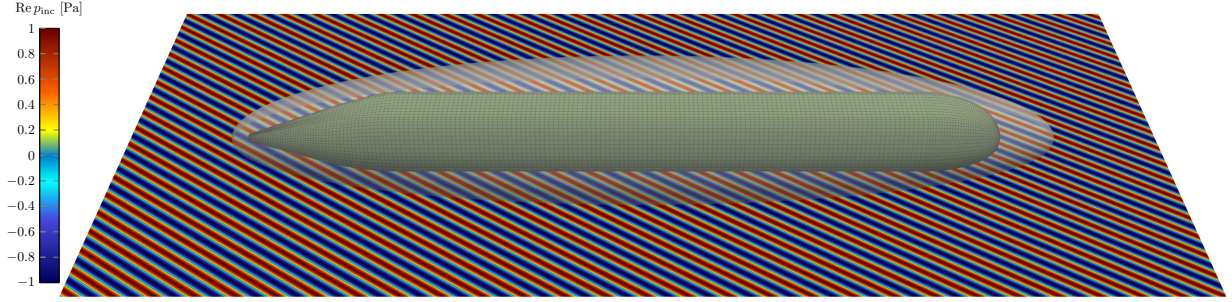


(d) Crosssection in the xz -plane for mesh $\mathcal{M}_{1, \hat{p}, \hat{k}}^{IGA}$.

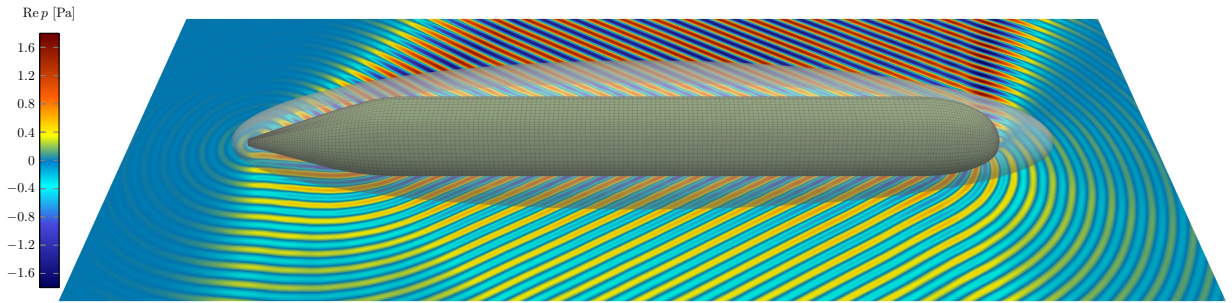


(e) Crosssection in the xz -plane for mesh $\mathcal{M}_{2, \hat{p}, \hat{k}}^{IGA}$.

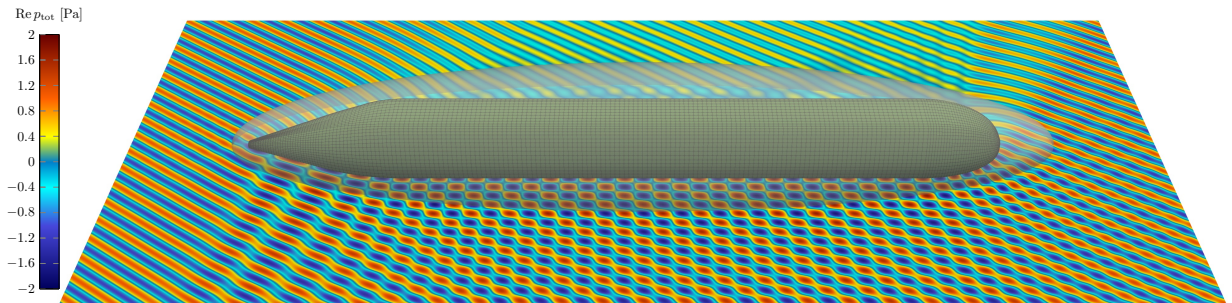
Figure 24: **Stripped BeTSSi submarine**: CAD model and meshes used for computations.



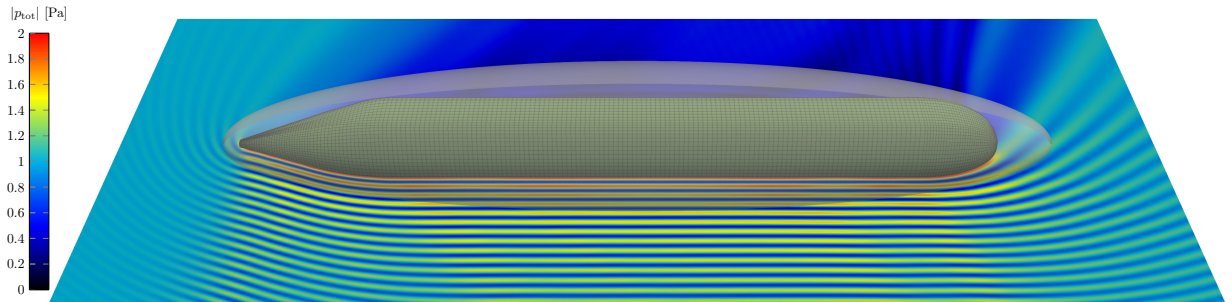
(a) Real part of the incident wave $p_{\text{inc}}(\mathbf{x}) = P_{\text{inc}}e^{ik\mathbf{d}_s \cdot \mathbf{x}}$.



(b) Real part of the scattered pressure $p(\mathbf{x})$.



(c) Real part of the total pressure $p_{\text{tot}}(\mathbf{x}) = p_{\text{inc}}(\mathbf{x}) + p(\mathbf{x})$.



(d) Modulus of the total pressure $p_{\text{tot}}(\mathbf{x}) = p_{\text{inc}}(\mathbf{x}) + p(\mathbf{x})$.

Figure 25: **Stripped BeTSSi submarine with SHBC**: The simulation at $f = 1000$ Hz is visualized in the xy -plane, and is computed on mesh $\mathcal{M}_{2,3,2}^{\text{GA}}$ and the BGU formulation with $N = 4$. The numerical evaluations outside the (transparent) prolate ellipsoidal artificial boundary are evaluated with Eq. (45).

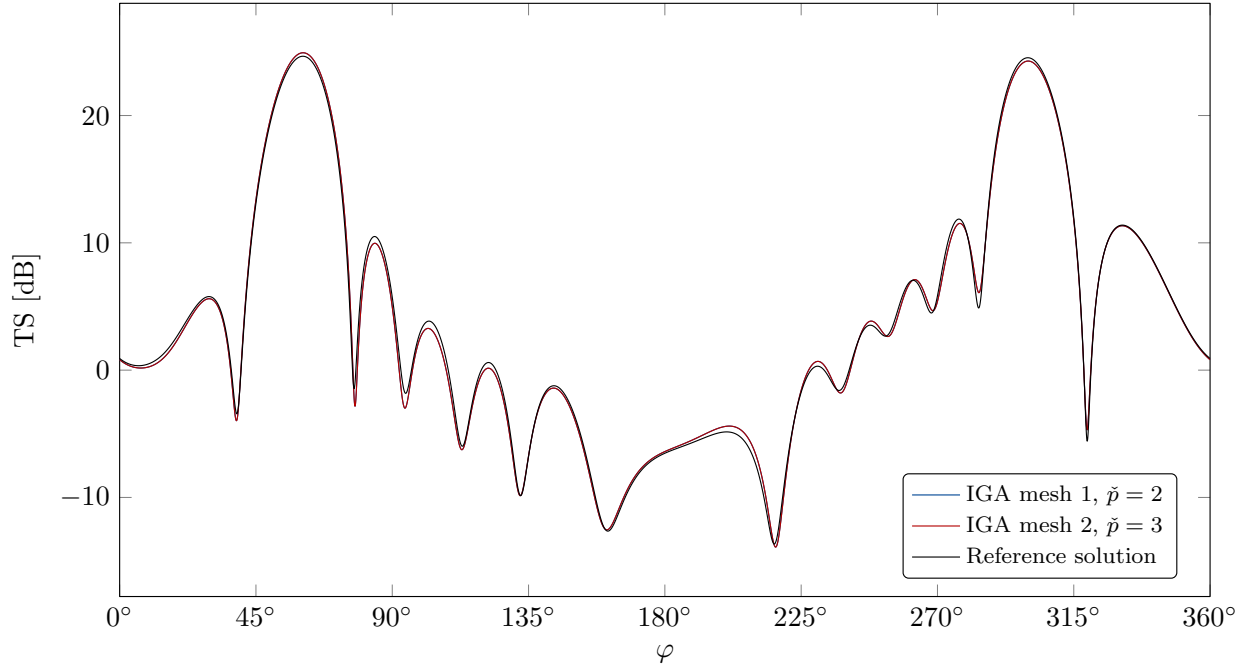


Figure 26: **Stripped BeTSSi submarine with SHBC**: Computation of target strength (Eq. (51)) at $f = 100$ Hz as a function of the azimuth angle in the spherical coordinate system. The two IGA results (both using $N = 3$) are visually indistinguishable meaning that mesh $\mathcal{M}_{1,2,1}^{\text{IGA}}$ is well resolved for this frequency.

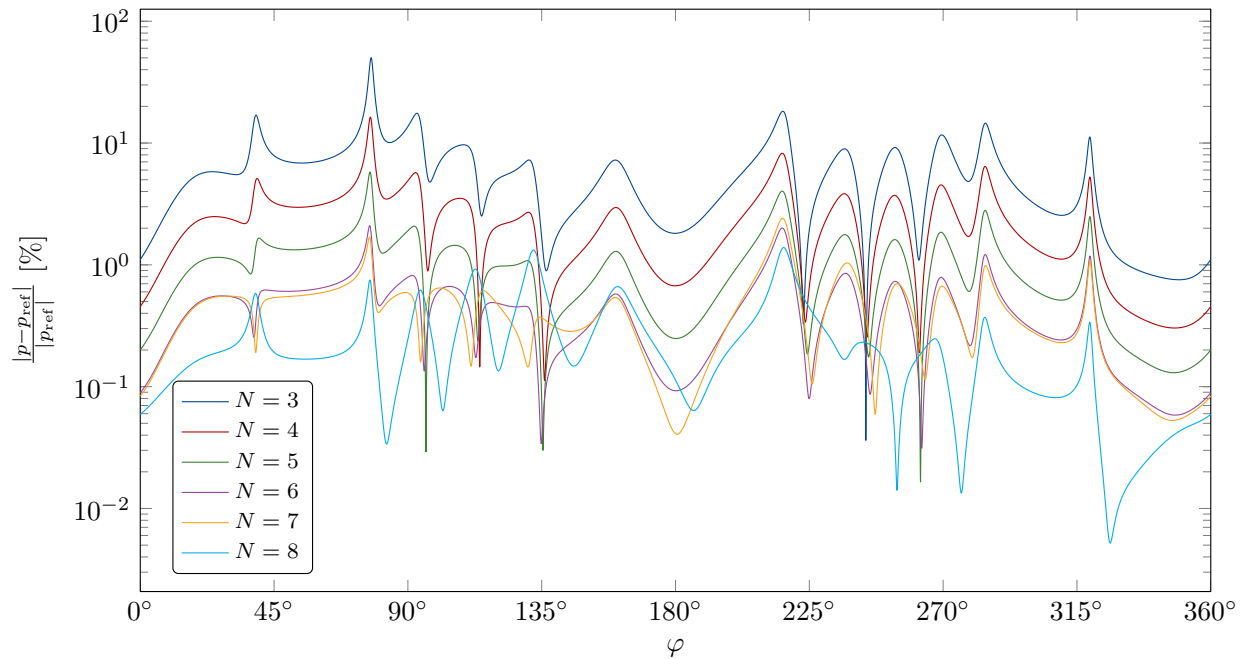
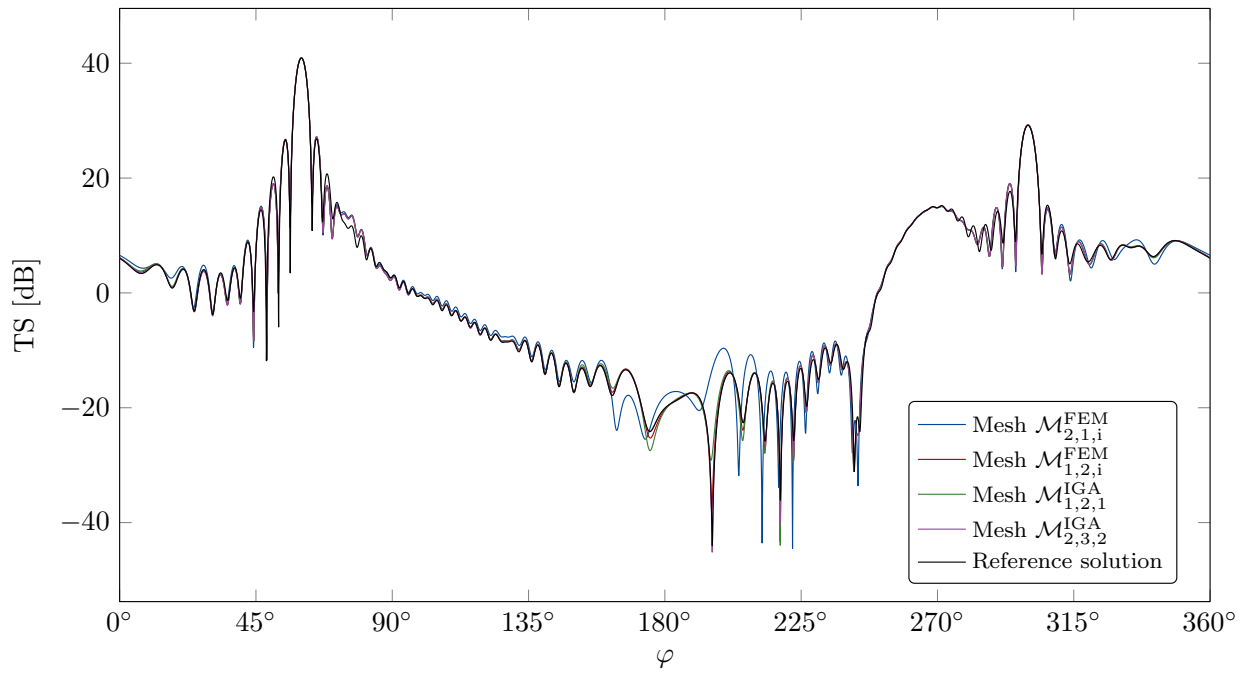
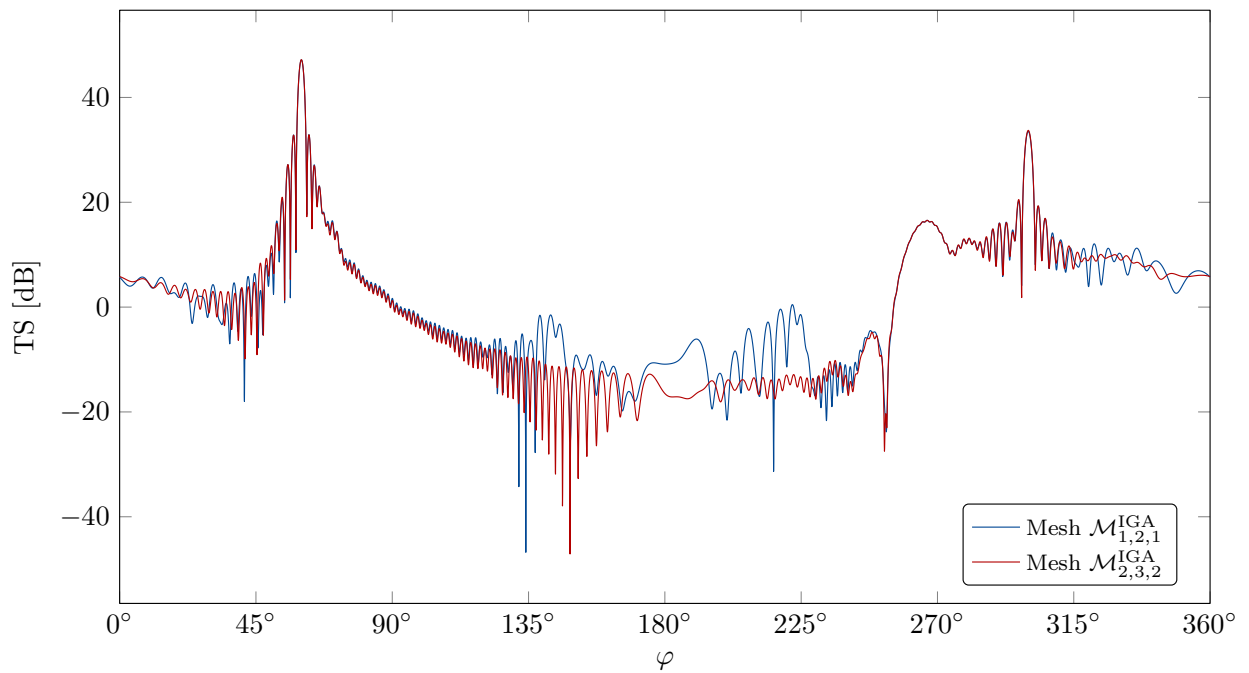


Figure 27: **Stripped BeTSSi submarine with SHBC**: Computation of the relative error in the far field (Eq. (45)) compared to a reference solution at $f = 100$ Hz. The computations are done using IGA on mesh $\mathcal{M}_{2,3,2}^{\text{IGA}}$ using the BGU formulation.



(a) $f = 500$ Hz



(b) $f = 1000$ Hz

Figure 28: **Stripped BeTSSi submarine with SHBC**: Computation of target strength (Eq. (51)) as a function of the azimuth angle in the spherical coordinate system. The numerical evaluations are evaluated with Eq. (51).

5. Conclusions

This article addresses acoustic scattering characterized by sound waves reflected by man-made elastic objects. The present approach is characterized by:

- The fluid surrounding (inside and in the vicinity outside) the solid scatterer is discretized by using isogeometric analysis (IGA).
- The unbounded domain outside the artificial boundary circumscribing the scatterer is handled by use of the infinite element method (IEM).
- The elastic scatterer is discretized by using IGA.
- The coupled acoustic structure interaction (ASI) problem is solved as a monolithic problem.

The main finding of the present study is that the use of IGA significantly increases the accuracy compared to the use of C^0 finite element analysis (FEA) due to increased inter-element continuity of the spline basis functions.

Furthermore, the following observations are made

- IGA and the four presented IEM formulations work well on acoustic scattering for low frequencies. Among the infinite element formulations, the unconjugated version seems to give the best results.
- IGA's ability to represent the geometry exactly was observed to be of less importance for accuracy when comparing to higher order ($\hat{p} \geq 2$) isoparametric FEA. However, a more significant improvement offered by IGA is due to higher continuity of the spline basis functions in the solution space.
- The IGA framework enables roughly the same accuracy per element (compared to higher order isoparametric FEA) even though the number of degrees of freedom is significantly reduced.
- IGA is more computationally efficient than FEA to obtain highly accurate solutions. That is, when the mesh is sufficiently resolved, a given accuracy is obtained computationally faster using IGA.
- As for the FEA, IGA also suffers from the pollution effect at high frequencies. This will always be a problem, and for the higher frequency spectrum, the methods must be extended correspondingly. The XIBEM [47, 48] (extended isogeometric boundary element method) is such an extension for the boundary element method. This technique (and similar enrichment strategies) could be applied to IEM as well, and is suggested as future work.
- The IEM suffers from high condition numbers when the number of radial shape functions in the infinite elements (N) is large. This becomes a problem for more complex geometries as N must be increased to achieve higher precision.

The main disadvantages of using IGA with IEM is the need for a surface-to-volume parametrization between the scatterer and the artificial boundary, Ω_a . In this paper, the scatterer has been simple enough to discretize Ω_a using a single 3D NURBS patch. For more complex geometries, this becomes more involved, and is a topic of active research to this date in the IGA community [49, 50, 51]. The surface-to-volume parametrization and the conditioning are the main open issues of IGA with IEM and should be explored in future research.

Acknowledgements

This work was supported by the Department of Mathematical Sciences at the Norwegian University of Science and Technology and by the Norwegian Defence Research Establishment.

The stripped BeTSSi submarine simulations were performed on resources provided by UNINETT Sigma2 - the National Infrastructure for High Performance Computing and Data Storage in Norway (reference number: NN9322K/4317).

The authors would like to thank the reviewers for detailed response and many constructive comments.

A. Derivation of bilinear form in infinite elements

In this appendix, the integrals in the bilinear forms for the infinite elements will be separated for the PGU case¹⁰. For generality, the derivation is done in the prolate spheroidal coordinate system.

A.1. The prolate spheroidal coordinate system

The prolate spheroidal coordinate system is an extension of the spherical coordinate system. It is defined by the relations

$$x = \sqrt{r^2 - \mathcal{T}^2} \sin \vartheta \cos \varphi \quad (\text{A.1})$$

$$y = \sqrt{r^2 - \mathcal{T}^2} \sin \vartheta \sin \varphi \quad (\text{A.2})$$

$$z = r \cos \vartheta \quad (\text{A.3})$$

with foci located at $z = \pm \mathcal{T}$ and $r \geq \mathcal{T}$. Note that the coordinate system reduces to the spherical coordinate system when $\mathcal{T} = 0$. the following inverse formulas may be derived

$$\begin{aligned} r &= \frac{1}{2}(d_1 + d_2) \\ \vartheta &= \arccos\left(\frac{z}{r}\right) \\ \varphi &= \text{atan2}(y, x) \end{aligned} \quad (\text{A.4})$$

where

$$\begin{aligned} d_1 &= d_1(x, y, z) = \sqrt{x^2 + y^2 + (z + \mathcal{T})^2} \\ d_2 &= d_2(x, y, z) = \sqrt{x^2 + y^2 + (z - \mathcal{T})^2} \end{aligned}$$

and

$$\text{atan2}(y, x) = \begin{cases} \arctan\left(\frac{y}{x}\right) & \text{if } x > 0 \\ \arctan\left(\frac{y}{x}\right) + \pi & \text{if } x < 0 \text{ and } y \geq 0 \\ \arctan\left(\frac{y}{x}\right) - \pi & \text{if } x < 0 \text{ and } y < 0 \\ \frac{\pi}{2} & \text{if } x = 0 \text{ and } y > 0 \\ -\frac{\pi}{2} & \text{if } x = 0 \text{ and } y < 0 \\ \text{undefined} & \text{if } x = 0 \text{ and } y = 0. \end{cases}$$

The derivatives are found to be

$$\begin{aligned} \frac{\partial x}{\partial r} &= \frac{r \sin \vartheta \cos \varphi}{\sqrt{r^2 - \mathcal{T}^2}}, & \frac{\partial y}{\partial r} &= \frac{r \sin \vartheta \sin \varphi}{\sqrt{r^2 - \mathcal{T}^2}}, & \frac{\partial z}{\partial r} &= \cos \vartheta \\ \frac{\partial x}{\partial \vartheta} &= \sqrt{r^2 - \mathcal{T}^2} \cos \vartheta \cos \varphi, & \frac{\partial y}{\partial \vartheta} &= \sqrt{r^2 - \mathcal{T}^2} \cos \vartheta \sin \varphi, & \frac{\partial z}{\partial \vartheta} &= -r \sin \vartheta \\ \frac{\partial x}{\partial \varphi} &= -\sqrt{r^2 - \mathcal{T}^2} \sin \vartheta \sin \varphi, & \frac{\partial y}{\partial \varphi} &= \sqrt{r^2 - \mathcal{T}^2} \sin \vartheta \cos \varphi, & \frac{\partial z}{\partial \varphi} &= 0 \end{aligned} \quad (\text{A.5})$$

and

$$\begin{aligned} \frac{\partial r}{\partial x} &= \frac{x(d_1 + d_2)}{2d_1d_2}, & \frac{\partial r}{\partial y} &= \frac{y(d_1 + d_2)}{2d_1d_2}, & \frac{\partial r}{\partial z} &= \frac{z(d_1 + d_2) + \mathcal{T}(d_2 - d_1)}{2d_1d_2} \\ \frac{\partial \vartheta}{\partial x} &= \frac{xz}{d_1d_2\sqrt{r^2 - z^2}}, & \frac{\partial \vartheta}{\partial y} &= \frac{yz}{d_1d_2\sqrt{r^2 - z^2}}, & \frac{\partial \vartheta}{\partial z} &= \frac{1}{\sqrt{r^2 - z^2}} \left(\frac{z^2}{d_1d_2} + \frac{\mathcal{T}z(d_2 - d_1)}{d_1d_2(d_1 + d_2)} - 1 \right) \\ \frac{\partial \varphi}{\partial x} &= -\frac{y}{x^2 + y^2}, & \frac{\partial \varphi}{\partial y} &= \frac{x}{x^2 + y^2}, & \frac{\partial \varphi}{\partial z} &= 0. \end{aligned} \quad (\text{A.6})$$

¹⁰The other three formulations has been derived in [44]. For the more general ellipsoidal coordinate system, refer to [52].

The general nabla operator can be written as

$$\nabla = \frac{\mathbf{e}_r}{h_r} \frac{\partial}{\partial r} + \frac{\mathbf{e}_\vartheta}{h_\vartheta} \frac{\partial}{\partial \vartheta} + \frac{\mathbf{e}_\varphi}{h_\varphi} \frac{\partial}{\partial \varphi} \quad (\text{A.7})$$

where

$$\mathbf{e}_r = \frac{1}{h_r} \left[\frac{\partial x}{\partial r}, \frac{\partial y}{\partial r}, \frac{\partial z}{\partial r} \right]^\top, \quad \mathbf{e}_\vartheta = \frac{1}{h_\vartheta} \left[\frac{\partial x}{\partial \vartheta}, \frac{\partial y}{\partial \vartheta}, \frac{\partial z}{\partial \vartheta} \right]^\top, \quad \mathbf{e}_\varphi = \frac{1}{h_\varphi} \left[\frac{\partial x}{\partial \varphi}, \frac{\partial y}{\partial \varphi}, \frac{\partial z}{\partial \varphi} \right]^\top$$

and

$$\begin{aligned} h_r &= \sqrt{\frac{r^2 - \Upsilon^2 \cos^2 \vartheta}{r^2 - \Upsilon^2}} \\ h_\vartheta &= \sqrt{r^2 - \Upsilon^2 \cos^2 \vartheta} \\ h_\varphi &= \sqrt{r^2 - \Upsilon^2} \sin \vartheta. \end{aligned}$$

The Jacobian determinant (for the mapping from Cartesian coordinates to prolate spheroidal coordinates) may now be written as

$$J_1 = h_r h_\vartheta h_\varphi = (r^2 - \Upsilon^2 \cos^2 \vartheta) \sin \vartheta. \quad (\text{A.8})$$

As any normal vector at a surface with constant radius $r = \gamma$ can be written as $\mathbf{n} = \mathbf{e}_\vartheta \times \mathbf{e}_\varphi = \mathbf{e}_r$

$$\partial_n p = \mathbf{n} \cdot \nabla p = \mathbf{e}_r \cdot \nabla p = \frac{1}{h_r} \frac{\partial p}{\partial r}. \quad (\text{A.9})$$

The surface Jacobian determinant at a given (constant) $r = \gamma$ is

$$J_S = h_\vartheta h_\varphi = \sqrt{r^2 - \Upsilon^2 \cos^2 \vartheta} \sqrt{r^2 - \Upsilon^2} \sin \vartheta, \quad (\text{A.10})$$

such that

$$q \partial_n p J_S = \mathcal{O}(r^{-3}) \quad \text{whenever} \quad q = \mathcal{O}(r^{-3}) \quad \text{and} \quad p = \mathcal{O}(r^{-1}). \quad (\text{A.11})$$

That is, for the Petrov–Galerkin formulations

$$\lim_{\gamma \rightarrow \infty} \int_{S_\gamma} q \partial_n p \, d\Gamma = \lim_{\gamma \rightarrow \infty} \int_0^{2\pi} \int_0^\pi q \partial_n p J_S \, d\vartheta \, d\varphi = 0. \quad (\text{A.12})$$

A.2. Bilinear form for unconjugated Petrov–Galerkin formulation

The bilinear form (in the domain outside the artificial boundary) in Eq. (43) (in the unconjugated case) can in the Petrov–Galerkin formulations be simplified to

$$\begin{aligned} B_{\text{PGU}}(R_I \psi_n, R_J \phi_m) &= \lim_{\gamma \rightarrow \infty} \int_{\Omega_\gamma^+} [\nabla(R_I \psi_n) \cdot \nabla(R_J \phi_m) - k^2 R_I \psi_n R_J \phi_m] \, d\Omega \\ &= \int_{\Omega_a^+} [\nabla(R_I \psi_n) \cdot \nabla(R_J \phi_m) - k^2 R_I \psi_n R_J \phi_m] \, d\Omega \end{aligned} \quad (\text{A.13})$$

as the mentioned surface integral in the far field vanishes (this is however not the case for the Bubnov–Galerkin formulations). Recall that the radial shape functions are given by

$$\begin{aligned} \phi_m(r) &= e^{ik(r-r_a)} Q_m\left(\frac{r_a}{r}\right), \quad m = 1, \dots, N \\ \psi_n(r) &= e^{ik(r-r_a)} \tilde{Q}_n\left(\frac{r_a}{r}\right), \quad n = 1, \dots, N \end{aligned}$$

such that the derivative can be computed by

$$\frac{d\phi_m}{dr} = \left[ik Q_m\left(\frac{r_a}{r}\right) - \frac{r_a}{r^2} Q'_m\left(\frac{r_a}{r}\right) \right] e^{ik(r-r_a)}$$

and corresponding expression for ψ_n . Using the expression for the nabla operator found in Eq. (A.7)

$$\begin{aligned}\nabla(R_I\psi_n) \cdot \nabla(R_J\phi_m) &= \frac{1}{h_r^2} \frac{\partial(R_I\psi_n)}{\partial r} \frac{\partial(R_J\phi_m)}{\partial r} + \frac{1}{h_\vartheta^2} \frac{\partial(R_I\psi_n)}{\partial \vartheta} \frac{\partial(R_J\phi_m)}{\partial \vartheta} + \frac{1}{h_\varphi^2} \frac{\partial(R_I\psi_n)}{\partial \varphi} \frac{\partial(R_J\phi_m)}{\partial \varphi} \\ &= \frac{1}{h_r^2} \frac{\partial\psi_n}{\partial r} \frac{\partial\phi_m}{\partial r} R_I R_J + \frac{1}{h_\vartheta^2} \psi_n \phi_m \frac{\partial R_I}{\partial \vartheta} \frac{\partial R_J}{\partial \vartheta} + \frac{1}{h_\varphi^2} \psi_n \phi_m \frac{\partial R_I}{\partial \varphi} \frac{\partial R_J}{\partial \varphi}\end{aligned}$$

which multiplied with the Jacobian J_1 yields

$$\begin{aligned}\nabla(R_I\psi_n) \cdot \nabla(R_J\phi_m) J_1 &= \left[(r^2 - \Upsilon^2) \frac{\partial\psi_n}{\partial r} \frac{\partial\phi_m}{\partial r} R_I R_J + \psi_n \phi_m \frac{\partial R_I}{\partial \vartheta} \frac{\partial R_J}{\partial \vartheta} \right. \\ &\quad \left. + \frac{r^2 - \Upsilon^2 \cos^2 \vartheta}{(r^2 - \Upsilon^2) \sin^2 \vartheta} \psi_n \phi_m \frac{\partial R_I}{\partial \varphi} \frac{\partial R_J}{\partial \varphi} \right] \sin \vartheta\end{aligned}$$

Combining all of this into Eq. (A.13) yields

$$B_{\text{PGU}}(R_I\psi_n, R_J\phi_m) = \int_0^{2\pi} \int_0^\pi K(\vartheta, \varphi) \sin \vartheta \, d\vartheta \, d\varphi \quad (\text{A.14})$$

where

$$\begin{aligned}K(\vartheta, \varphi) &= \int_{r_a}^\infty \left\{ (r^2 - \Upsilon^2) \frac{\partial\psi_n}{\partial r} \frac{\partial\phi_m}{\partial r} R_I R_J + \psi_n \phi_m \frac{\partial R_I}{\partial \vartheta} \frac{\partial R_J}{\partial \vartheta} \right. \\ &\quad \left. + \frac{r^2 - \Upsilon^2 \cos^2 \vartheta}{(r^2 - \Upsilon^2) \sin^2 \vartheta} \psi_n \phi_m \frac{\partial R_I}{\partial \varphi} \frac{\partial R_J}{\partial \varphi} - k^2 (r^2 - \Upsilon^2 \cos^2 \vartheta) \psi_n \phi_m R_I R_J \right\} dr.\end{aligned}$$

Inserting the expressions for the radial shape functions ϕ and ψ (with Einstein's summation convention) with their corresponding derivatives one obtains the following expression using the substitution $\rho = \frac{r}{r_a}$ and the notation $\varrho_1 = \Upsilon/r_a$ (the eccentricity of the infinite-element spheroid), $\varrho_2 = kr_a$ and $\varrho_3 = k\Upsilon$

$$\begin{aligned}K(\vartheta, \varphi) &= \left\{ R_I R_J \left[-2\varrho_2^2 B_{\tilde{n}+\tilde{m}}^{(1)} - i\varrho_2(\tilde{n} + \tilde{m} + 2) B_{\tilde{n}+\tilde{m}+1}^{(1)} + [\tilde{m}(\tilde{n} + 2) + \varrho_3^2] B_{\tilde{n}+\tilde{m}+2}^{(1)} \right. \right. \\ &\quad \left. \left. + i\varrho_1^2 \varrho_2(\tilde{n} + \tilde{m} + 2) B_{\tilde{n}+\tilde{m}+3}^{(1)} - \tilde{m}(\tilde{n} + 2) \varrho_1^2 B_{\tilde{n}+\tilde{m}+4}^{(1)} + \varrho_3^2 \cos^2 \vartheta B_{\tilde{n}+\tilde{m}+2}^{(1)} \right] \right. \\ &\quad \left. + \frac{\partial R_I}{\partial \vartheta} \frac{\partial R_J}{\partial \vartheta} B_{\tilde{n}+\tilde{m}+2}^{(1)} + \frac{\partial R_I}{\partial \varphi} \frac{\partial R_J}{\partial \varphi} \frac{1}{\sin^2 \vartheta} \left(B_{\tilde{n}+\tilde{m}+1}^{(2)} - \varrho_1^2 \cos^2 \vartheta B_{\tilde{n}+\tilde{m}+3}^{(2)} \right) \right\} r_a e^{-2i\varrho_2} \tilde{D}_{n\tilde{n}} D_{m\tilde{m}}\end{aligned}$$

where the radial integrals

$$B_n^{(1)} = \int_1^\infty \frac{e^{2i\varrho_2\rho}}{\rho^n} d\rho \quad B_n^{(2)} = \int_1^\infty \frac{e^{2i\varrho_2\rho}}{(\rho^2 - \varrho_1^2)\rho^{n-1}} d\rho, \quad n \geq 1$$

can be evaluated according to formulas in Appendix B.

Assume that the artificial boundary Γ_a is parameterized by ξ and η . As Γ_a is a surface with constant radius, $r = r_a$, in the prolate spheroidal coordinate system, it may also be parameterized by ϑ and φ . Therefore,

$$d\vartheta d\varphi = \begin{vmatrix} \frac{\partial\vartheta}{\partial\xi} & \frac{\partial\vartheta}{\partial\eta} \\ \frac{\partial\varphi}{\partial\xi} & \frac{\partial\varphi}{\partial\eta} \end{vmatrix} d\xi d\eta \quad (\text{A.15})$$

where

$$\begin{aligned}\frac{\partial\vartheta}{\partial\xi} &= \frac{\partial\vartheta}{\partial x} \frac{\partial x}{\partial\xi} + \frac{\partial\vartheta}{\partial y} \frac{\partial y}{\partial\xi} + \frac{\partial\vartheta}{\partial z} \frac{\partial z}{\partial\xi}, & \frac{\partial\vartheta}{\partial\eta} &= \frac{\partial\vartheta}{\partial x} \frac{\partial x}{\partial\eta} + \frac{\partial\vartheta}{\partial y} \frac{\partial y}{\partial\eta} + \frac{\partial\vartheta}{\partial z} \frac{\partial z}{\partial\eta} \\ \frac{\partial\varphi}{\partial\xi} &= \frac{\partial\varphi}{\partial x} \frac{\partial x}{\partial\xi} + \frac{\partial\varphi}{\partial y} \frac{\partial y}{\partial\xi} + \frac{\partial\varphi}{\partial z} \frac{\partial z}{\partial\xi}, & \frac{\partial\varphi}{\partial\eta} &= \frac{\partial\varphi}{\partial x} \frac{\partial x}{\partial\eta} + \frac{\partial\varphi}{\partial y} \frac{\partial y}{\partial\eta} + \frac{\partial\varphi}{\partial z} \frac{\partial z}{\partial\eta}\end{aligned}$$

and the inverse partial derivatives with respect to the coordinate transformation (from the prolate spheroidal coordinate system to the Cartesian coordinate system) is found in Eq. (A.6). This Jacobian matrix may be evaluated by

$$J_3 = \begin{bmatrix} \frac{\partial \vartheta}{\partial \xi} & \frac{\partial \vartheta}{\partial \eta} \\ \frac{\partial \varphi}{\partial \xi} & \frac{\partial \varphi}{\partial \eta} \end{bmatrix} = \begin{bmatrix} \frac{\partial \vartheta}{\partial x} & \frac{\partial \vartheta}{\partial y} & \frac{\partial \vartheta}{\partial z} \\ \frac{\partial \varphi}{\partial x} & \frac{\partial \varphi}{\partial y} & \frac{\partial \varphi}{\partial z} \end{bmatrix} \begin{bmatrix} \frac{\partial x}{\partial \xi} & \frac{\partial x}{\partial \eta} \\ \frac{\partial y}{\partial \xi} & \frac{\partial y}{\partial \eta} \\ \frac{\partial z}{\partial \xi} & \frac{\partial z}{\partial \eta} \end{bmatrix} \quad (\text{A.16})$$

and the derivatives of the basis functions may then be computed by

$$\begin{bmatrix} \frac{\partial R_I}{\partial \vartheta} \\ \frac{\partial R_J}{\partial \vartheta} \\ \frac{\partial R_I}{\partial \varphi} \\ \frac{\partial R_J}{\partial \varphi} \end{bmatrix} = J_3^{-\top} \begin{bmatrix} \frac{\partial R_I}{\partial \xi} \\ \frac{\partial R_I}{\partial \eta} \end{bmatrix}. \quad (\text{A.17})$$

Defining the angular integrals

$$\begin{aligned} A_{IJ}^{(1)} &= \int_0^{2\pi} \int_0^\pi R_I R_J \sin \vartheta \, d\vartheta \, d\varphi, & A_{IJ}^{(2)} &= \int_0^{2\pi} \int_0^\pi \frac{\partial R_I}{\partial \vartheta} \frac{\partial R_J}{\partial \vartheta} \sin \vartheta \, d\vartheta \, d\varphi \\ A_{IJ}^{(3)} &= \int_0^{2\pi} \int_0^\pi R_I R_J \cos^2 \vartheta \sin \vartheta \, d\vartheta \, d\varphi, & A_{IJ}^{(4)} &= \int_0^{2\pi} \int_0^\pi \frac{\partial R_I}{\partial \varphi} \frac{\partial R_J}{\partial \varphi} \frac{1}{\sin \vartheta} \, d\vartheta \, d\varphi \\ A_{IJ}^{(5)} &= \int_0^{2\pi} \int_0^\pi \frac{\partial R_I}{\partial \varphi} \frac{\partial R_J}{\partial \varphi} \frac{\cos^2 \vartheta}{\sin \vartheta} \, d\vartheta \, d\varphi \end{aligned} \quad (\text{A.18})$$

the bilinear form may then finally be written as (Einstein's summation convention is used for the indices \tilde{n} and \tilde{m})

$$\begin{aligned} B_{\text{PGU}}(R_I \psi_n, R_J \phi_m) &= \left\{ A_{IJ}^{(1)} \left[-2\varrho_2^2 B_{\tilde{n}+\tilde{m}}^{(1)} - i\varrho_2(\tilde{n} + \tilde{m} + 2) B_{\tilde{n}+\tilde{m}+1}^{(1)} + [(\tilde{n} + 2)\tilde{m} + \varrho_3^2] B_{\tilde{n}+\tilde{m}+2}^{(1)} \right. \right. \\ &\quad \left. \left. + i\varrho_1\varrho_3(\tilde{n} + \tilde{m} + 2) B_{\tilde{n}+\tilde{m}+3}^{(1)} - \varrho_1^2(\tilde{n} + 2)\tilde{m} B_{\tilde{n}+\tilde{m}+4}^{(1)} \right] \right. \\ &\quad \left. + A_{IJ}^{(2)} B_{\tilde{n}+\tilde{m}+2}^{(1)} + \varrho_3^2 A_{IJ}^{(3)} B_{\tilde{n}+\tilde{m}+2}^{(1)} \right. \\ &\quad \left. + A_{IJ}^{(4)} B_{\tilde{n}+\tilde{m}+1}^{(2)} - \varrho_1^2 A_{IJ}^{(5)} B_{\tilde{n}+\tilde{m}+3}^{(2)} \right\} r_a e^{-2i\varrho_2} D_{m\tilde{m}} \tilde{D}_{n\tilde{n}}. \end{aligned} \quad (\text{A.19})$$

For completeness, the formulas for the other three formulations are included

$$\begin{aligned} B_{\text{BGU}}(R_I \psi_n, R_J \phi_m) &= \left\{ A_{IJ}^{(1)} \left[-2\varrho_2^2 B_{\tilde{n}+\tilde{m}-2}^{(1)} (1 - \delta_{\tilde{n}1} \delta_{\tilde{m}1}) - i\varrho_2(\tilde{n} + \tilde{m}) B_{\tilde{n}+\tilde{m}-1}^{(1)} + (\tilde{n}\tilde{m} + \varrho_3^2) B_{\tilde{n}+\tilde{m}}^{(1)} \right. \right. \\ &\quad \left. \left. + i\varrho_1\varrho_3(\tilde{n} + \tilde{m}) B_{\tilde{n}+\tilde{m}+1}^{(1)} - \varrho_1^2 \tilde{n}\tilde{m} B_{\tilde{n}+\tilde{m}+2}^{(1)} \right] \right. \\ &\quad \left. + A_{IJ}^{(2)} B_{\tilde{n}+\tilde{m}}^{(1)} + \varrho_3^2 A_{IJ}^{(3)} B_{\tilde{n}+\tilde{m}}^{(1)} \right. \\ &\quad \left. + A_{IJ}^{(4)} B_{\tilde{n}+\tilde{m}-1}^{(2)} - \varrho_1^2 A_{IJ}^{(5)} B_{\tilde{n}+\tilde{m}+1}^{(2)} \right\} r_a e^{-2i\varrho_2} D_{m\tilde{m}} \tilde{D}_{n\tilde{n}} \\ &\quad - i\varrho_2 r_a D_{m1} \tilde{D}_{n1} A_{IJ}^{(1)} \end{aligned} \quad (\text{A.20})$$

$$\begin{aligned} B_{\text{PGC}}(R_I \psi_n, R_J \phi_m) &= \left\{ A_{IJ}^{(1)} \left[-i\varrho_2(\tilde{n} - \tilde{m} + 2) B_{\tilde{n}+\tilde{m}+1}^{(1)} + [(\tilde{n} + 2)\tilde{m} - \varrho_3^2] B_{\tilde{n}+\tilde{m}+2}^{(1)} \right. \right. \\ &\quad \left. \left. + i\varrho_1\varrho_3(\tilde{n} - \tilde{m} + 2) B_{\tilde{n}+\tilde{m}+3}^{(1)} - \varrho_1^2(\tilde{n} + 2)\tilde{m} B_{\tilde{n}+\tilde{m}+4}^{(1)} \right] \right. \\ &\quad \left. + A_{IJ}^{(2)} B_{\tilde{n}+\tilde{m}+2}^{(1)} + \varrho_3^2 A_{IJ}^{(3)} B_{\tilde{n}+\tilde{m}+2}^{(1)} \right. \\ &\quad \left. + A_{IJ}^{(4)} B_{\tilde{n}+\tilde{m}+1}^{(2)} - \varrho_1^2 A_{IJ}^{(5)} B_{\tilde{n}+\tilde{m}+3}^{(2)} \right\} r_a D_{m\tilde{m}} \tilde{D}_{n\tilde{n}} \end{aligned} \quad (\text{A.21})$$

$$\begin{aligned}
B_{\text{BGC}}(R_I\psi_n, R_J\phi_m) = & \left\{ A_{IJ}^{(1)} \left[-i\varrho_2(\tilde{n} - \tilde{m})B_{\tilde{n}+\tilde{m}-1}^{(1)} + (\tilde{n}\tilde{m} - \varrho_3^2)B_{\tilde{n}+\tilde{m}}^{(1)} \right. \right. \\
& \left. \left. + i\varrho_1\varrho_3(\tilde{n} - \tilde{m})B_{\tilde{n}+\tilde{m}+1}^{(1)} - \varrho_1^2\tilde{n}\tilde{m}B_{\tilde{n}+\tilde{m}+2}^{(1)} \right] \right. \\
& \left. + A_{IJ}^{(2)}B_{\tilde{n}+\tilde{m}}^{(1)} + \varrho_3^2A_{IJ}^{(3)}B_{\tilde{n}+\tilde{m}}^{(1)} \right. \\
& \left. + A_{IJ}^{(4)}B_{\tilde{n}+\tilde{m}-1}^{(2)} - \varrho_1^2A_{IJ}^{(5)}B_{\tilde{n}+\tilde{m}+1}^{(2)} \right\} r_a D_{m\tilde{m}} \tilde{D}_{n\tilde{n}} \\
& - i r_a \varrho_2 D_{m1} \tilde{D}_{n1} A_{IJ}^{(1)}
\end{aligned} \tag{A.22}$$

where δ_{ij} is the Kronecker delta function in Eq. (31).

B. Evaluation of radial integrals

The exponential integral

$$E_n(z) = \int_1^\infty \frac{e^{-z\rho}}{\rho^n} d\rho, \quad \text{Re}(z) \geq 0 \tag{B.1}$$

is of great importance for the unconjugated formulations in the IEM. It is therefore important to be able to evaluate the integral accurately and efficiently, also for large (absolute) values of z (which will correspond to high frequencies). In [53, p. 229, 5.1.12] the series representation for evaluation of these functions can be found¹¹

$$E_n(z) = \frac{(-z)^{n-1}}{(n-1)!} \left[-\ln z - \gamma + \sum_{m=1}^{n-1} \frac{1}{m} \right] - \sum_{\substack{m=0 \\ m \neq n-1}}^\infty \frac{(-z)^m}{(m-n+1)m!} \tag{B.2}$$

with the empty sum interpreted to be zero. Moreover, using the continued fraction notation

$$b_0 + \frac{a_1}{b_1 + \frac{a_2}{b_2 + \frac{a_3}{b_3 + \dots}}} = b_0 + \frac{a_1}{b_1 + \frac{a_2}{b_2 + \frac{a_3}{b_3 + \dots}}} \tag{B.3}$$

the continued fraction representation of these functions are given by [53, p. 229, 5.1.22]

$$E_n(z) = e^{-z} \left(\frac{1}{z+1} \frac{n}{1+z} \frac{1}{1+z} \frac{n+1}{1+z} \frac{2}{z+1} \frac{n+2}{1+z} \frac{3}{z+1} \dots \right). \tag{B.4}$$

In [54, p. 222] Press et al. present an even faster converging continued fraction given by

$$E_n(z) = e^{-z} \left(\frac{1}{z+n} \frac{1 \cdot n}{z+n+2} \frac{2(n+1)}{z+n+4} \frac{3(n+2)}{z+n+6} \dots \right). \tag{B.5}$$

It is here suggested to use Eq. (B.2) when $|z| \lesssim 1$ and Eq. (B.4) or Eq. (B.5) when $|z| \gtrsim 1$. Press et al. then continue to present efficient algorithms for evaluation of these formulas.

Using series expansions at infinity

$$\frac{1}{\rho^2 - \varrho_1^2} = \frac{1}{\varrho_1^2} \sum_{j=1}^\infty \left(\frac{\varrho_1}{\rho} \right)^{2j}, \tag{B.6}$$

¹¹Here, γ is the Euler-Mascheroni constant which is defined by

$$\gamma = \lim_{n \rightarrow \infty} \left[-\ln(n) + \sum_{m=1}^n \frac{1}{m} \right] = 0.577215664901532860606512090082 \dots$$

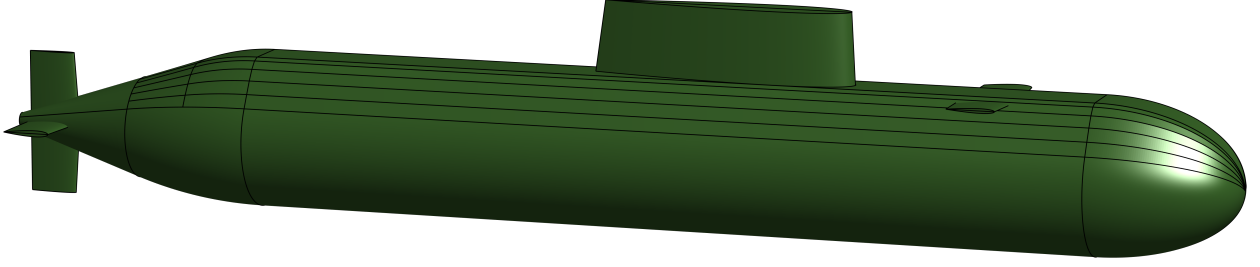


Figure C.29: Outer pressure hull for BeTSSi submarine.

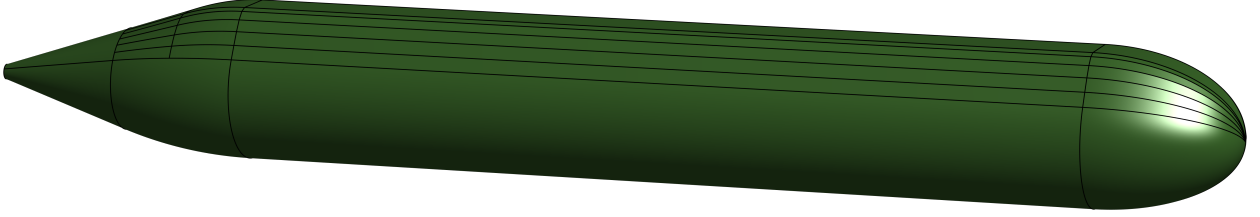


Figure C.30: The stripped BeTSSi submarine model.

the radial integrals for 3D infinite elements may be computed by

$$\int_1^\infty \frac{1}{\rho^n} d\rho = \frac{1}{n-1} \quad (\text{B.7})$$

$$\int_1^\infty \frac{1}{(\rho^2 - \varrho_1^2)\rho^{n-1}} d\rho = \sum_{j=0}^\infty \frac{\varrho_1^{2j}}{2j+n} \quad (\text{B.8})$$

in the conjugated case and

$$\int_1^\infty \frac{e^{2i\varrho_2\rho}}{\rho^n} d\rho = E_n(-2i\varrho_2) \quad (\text{B.9})$$

$$\int_1^\infty \frac{e^{2i\varrho_2\rho}}{(\rho^2 - \varrho_1^2)\rho^{n-1}} d\rho = \sum_{j=0}^\infty \varrho_1^{2j} E_{2j+n+1}(-2i\varrho_2) \quad (\text{B.10})$$

in the unconjugated case.

C. The stripped BeTSSi submarine model

In this section a simplified version of the BeTSSi submarine model (depicted in Figure C.29) will be presented. Namely a *stripped BeTSSi submarine model* without sail and rudders as in Figure C.30. The relevant BeTSSi parameters for the work presented herein are given in Table C.3. The model is symmetric about the xz -plane and has rotational symmetry for the lower part as described in Figure C.31. The transition from this axisymmetric part to the deck is described in Figure C.32. This transition as well as the deck itself, contains a set of rectangular panels of length L . The polynomial $P(y)$, is uniquely defined by the requirement that it defines a smooth transition between the hull and the deck. More precisely, the following requirement must be satisfied:

$$\begin{aligned} P(s) &= c, & P\left(b \sin \frac{\beta}{2}\right) &= -b \cos \frac{\beta}{2} \\ P'(s) &= 0, & P'\left(b \sin \frac{\beta}{2}\right) &= \tan \frac{\beta}{2} \end{aligned}$$

Table C.3: **BeTSSi submarine**: Parameters for the BeTSSi submarine benchmark.

Parameter	Description
$P_{\text{inc}} = 1 \text{ Pa}$	Amplitude of incident wave
$E = 2.10 \cdot 10^{11} \text{ Pa}$	Young's modulus
$\nu = 0.3$	Poisson's ratio
$\rho_s = 7850 \text{ kg m}^{-3}$	Density of solid
$\rho_f = 1000 \text{ kg m}^{-3}$	Density of water
$c_f = 1500 \text{ m s}^{-1}$	Speed of sound in water
$t = 0.01 \text{ m}$	Thickness of pressure hull
$\alpha = 18^\circ$	Arc angle of transition to the tail cone
$\beta = 240^\circ$	Rotational angle for the axisymmetric lower part of the pressure hull
$g_2 = 6.5 \text{ m}$	Distance in x -direction of transition to the tail cone
$g_3 = 6.5 \text{ m}$	Distance in x -direction of the tail cone
$L = 42 \text{ m}$	Length of the deck
$a = 7 \text{ m}$	Semi-major axis of bow
$b = 3.5 \text{ m}$	Semi-major axis of bow
$c = 4 \text{ m}$	Height from x -axis to the deck
$s = 1.2 \text{ m}$	Half of the width of the deck

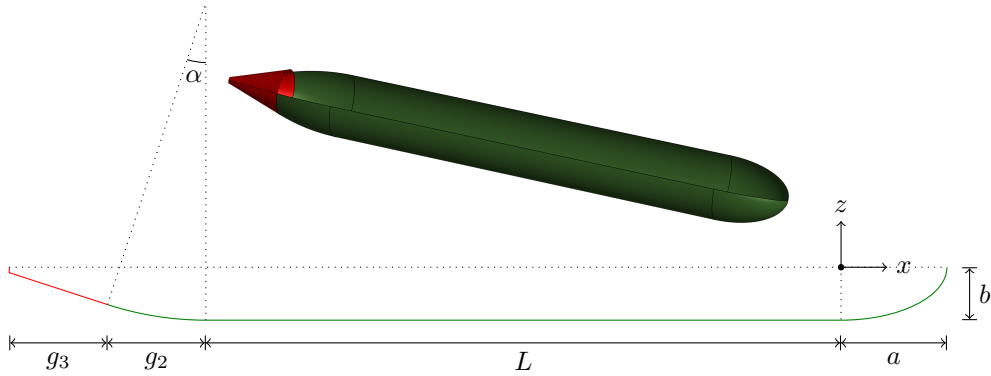


Figure C.31: The side line of the lower part of the BeTSSi submarine. The side lines are formed (from the right) by an ellipse with semi-major axis a and semi-minor axis b , followed by a straight line of length L , then an arc of angle α and finally two straight lines. The latter two straight lines (in red) are rotated about the x -axis and the remaining part (in green) are rotated an angle β around the x -axis.

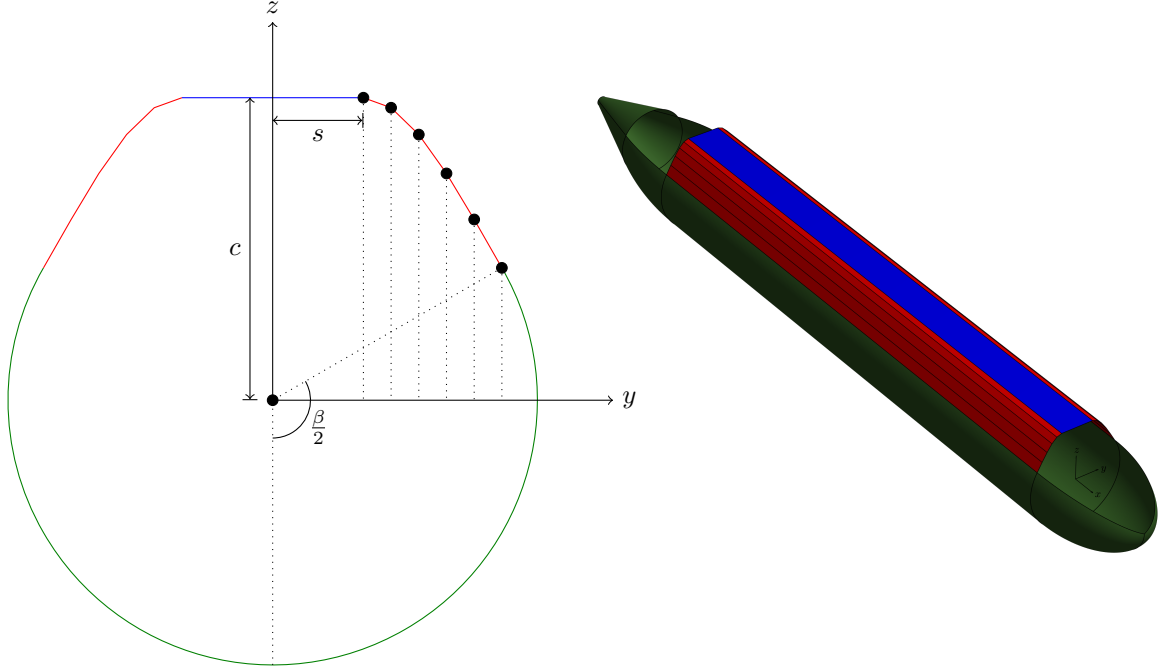


Figure C.32: The transition (red line) from the axisymmetric hull (green line) to the deck (blue line) is given by sampling a cubic polynomial, $P(y)$, at 6 equidistant points in the y -direction and connecting the resulting points with straight lines (corresponding 6 points are found for negative values y -values, $(0, y, P(|y|))$).

which gives the polynomial

$$P(y) = c + C_1(y - s)^2 + C_2(y - s)^3 \quad (\text{C.1})$$

where

$$C_1 = -\frac{3C_4 + C_3 \tan \frac{\beta}{2}}{C_3^2}, \quad C_2 = \frac{2C_4 + C_3 \tan \frac{\beta}{2}}{C_3^3}, \quad C_3 = b \sin \frac{\beta}{2} - s, \quad C_4 = c + b \cos \frac{\beta}{2}.$$

The upper part of the bow (highlighted in Figure C.33a) is obtained by linear lofting of elliptic curves from the 12 points described in Figure C.32 to the tip of the bow. The upper part of the tail section (highlighted in Figure C.33b) is connected using a tensor NURBS surface of degree 2 such that it defines a smooth transition from the axisymmetric cone to the deck. More precisely, the upper part of the cone tail is divided into 12 arcs with angle $\frac{2\pi-\beta}{12}$, and the resulting points are connected to corresponding points on the transition to the deck from the axisymmetric hull. As illustrated in Figure C.34a, the NURBS patch is given by 22 elements. Thus, $4 \cdot 23 = 92$ control points, $\mathbf{P}_{i,j}$, is needed as shown in Figure C.34b (23 and 4 control points in the ξ direction and η direction, respectively). The control points $\mathbf{P}_{1,j}$ and $\mathbf{P}_{23,j}$ for $j = 1, 2, 3, 4$ must be defined as in Figure C.35b, while the control points $\mathbf{P}_{i,1}$ must be defined as in Figure C.35a (with corresponding weights). For $2 \leq i \leq 22$ the weights are defined by $w_{i,j} = w_{i,1}$ for $j = 2, 3, 4$. That is,

$$w_{i,j} = \begin{cases} 1 & i \text{ odd} \\ \cos\left(\frac{2\pi-\beta}{24}\right) & i \text{ even, } i \neq 12 \\ \cos\left(\frac{2\pi-\beta}{12}\right) & i = 12 \end{cases} \quad (\text{C.2})$$

The location of the control points $\mathbf{P}_{i,j}$, $j = 2, 3$ and $2 \leq i \leq 22$, are determined by the requirement that the x component is the same as $\mathbf{P}_{1,j}$ and the fact that the control polygon lines must be tangential to the surface both at the deck and the cone tail.

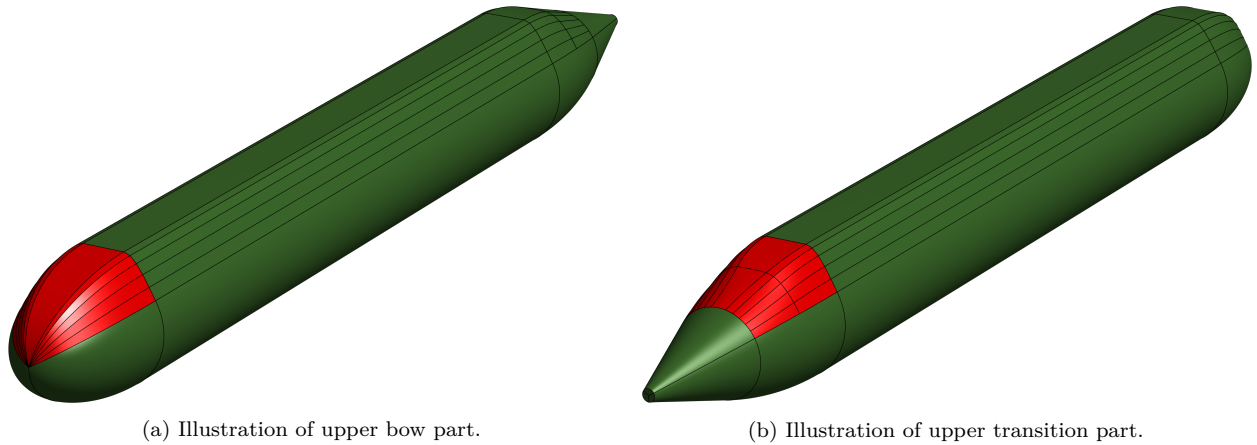


Figure C.33: Final patches for the stripped BeTSSi submarine.

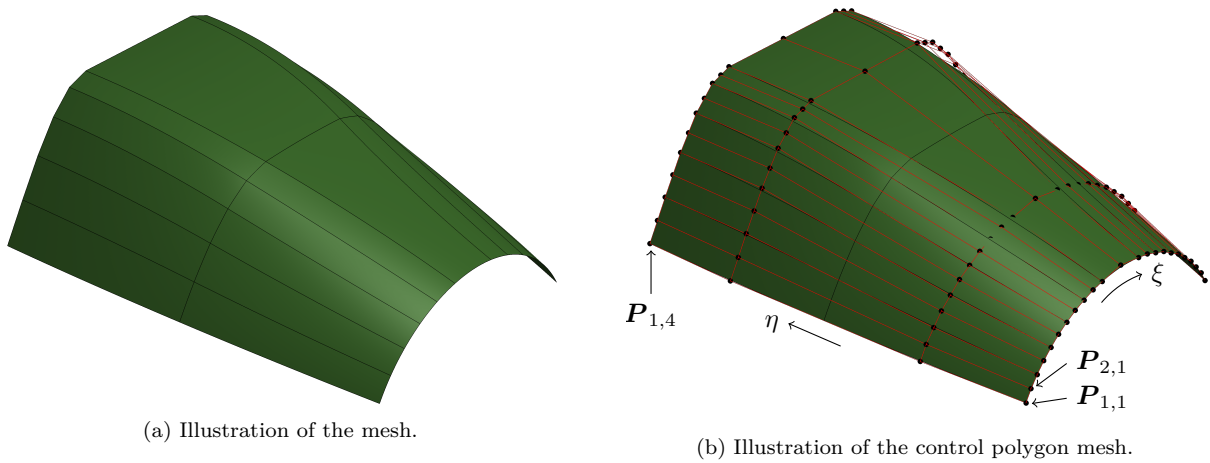


Figure C.34: Illustration of the upper transition part of the tail.

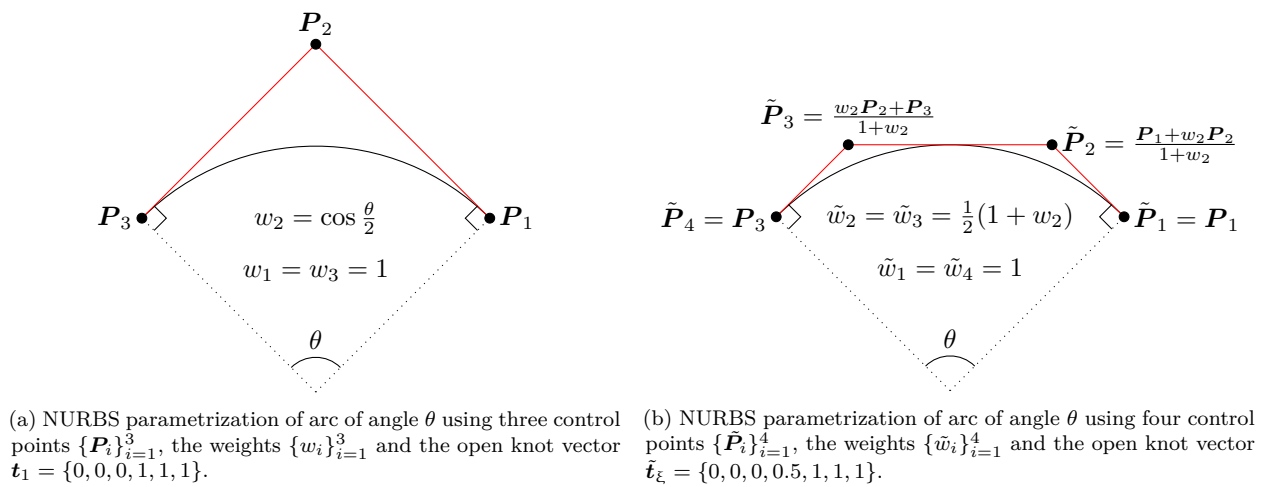


Figure C.35: Two ways of parametrizing an arc using NURBS [55, p. 315].

The inner surface of the BeTSSi submarine is generated by scaling a copy of the outer surface with the following change in the parameters $a \rightarrow a - t$, $b \rightarrow b - t$, $c \rightarrow c - t$, $s \rightarrow s - t/2$, $g_2 \rightarrow g_2 - t/2$ and $g_3 \rightarrow g_3 - t/2$ (α , β and l remain unchanged).

D. Approximating NURBS parametrizations with B-spline parametrizations

Starting with any NURBS parametrizations of a geometry where every internal knot has multiplicity $m = \check{p}_\xi$ in the ξ -direction and correspondingly in the other two parameter directions, we want to transform the NURBS parametrization of the exact geometry, to a B-spline representation. This representation approximates the geometry by interpolating the geometry at $n_\xi \cdot n_\eta \cdot n_\zeta$ (not necessarily unique) physical points resulting from a grid in the parametric space.

Let \mathbf{X} be the NURBS parametrization of the geometry (with notation similar to [6, p. 51])

$$\mathbf{X}(\xi, \eta, \zeta) = \sum_{i=1}^{n_\xi} \sum_{j=1}^{n_\eta} \sum_{l=1}^{n_\zeta} R_{i,j,l}^{\check{p}_\xi, \check{p}_\eta, \check{p}_\zeta}(\xi, \eta, \zeta) \mathbf{P}_{i,j,l}, \quad (\text{D.1})$$

with knot vectors \mathbf{t}_1 , \mathbf{t}_2 and \mathbf{t}_3 , polynomial order \check{p}_ξ , \check{p}_η and \check{p}_ζ . For each control point $\mathbf{P}_{i,j,l}$ we will need a corresponding interpolating point $\mathbf{Q}_{i,j,l}$ which will be located at the grid point $(\tilde{\xi}_i, \tilde{\eta}_j, \tilde{\zeta}_l)$. These points in the parameter domain are chosen to be the Greville abscissae

$$\tilde{\xi}_i = \frac{1}{\check{p}_\xi} \sum_{\tilde{i}=i+1}^{i+\check{p}_\xi} \xi_{\tilde{i}}, \quad i = 1, \dots, n_\xi \quad (\text{D.2})$$

$$\tilde{\eta}_j = \frac{1}{\check{p}_\eta} \sum_{\tilde{j}=j+1}^{j+\check{p}_\eta} \eta_{\tilde{j}}, \quad j = 1, \dots, n_\eta \quad (\text{D.3})$$

$$\tilde{\zeta}_l = \frac{1}{\check{p}_\zeta} \sum_{\tilde{l}=l+1}^{l+\check{p}_\zeta} \zeta_{\tilde{l}}, \quad l = 1, \dots, n_\zeta, \quad (\text{D.4})$$

where ξ_i , η_j and ζ_l are the knots of the knot vectors \mathbf{t}_1 , \mathbf{t}_2 and \mathbf{t}_3 , respectively.

We can now compute the interpolation points $\mathbf{Q}_{i,j,l}$ by

$$\mathbf{Q}_{i,j,l} = \mathbf{X}(\tilde{\xi}_i, \tilde{\eta}_j, \tilde{\zeta}_l). \quad (\text{D.5})$$

To find a B-spline approximation of the geometry which interpolates the points $\mathbf{Q}_{i,j,l}$, we want this new parametrization $\tilde{\mathbf{X}}$ to be based on \mathbf{X} such that their order and knot vectors are equal. As all weights will be set to 1 (to get a B-spline parametrization), we are only left with dofs in the control points, $\tilde{\mathbf{P}}_{i,j,l}$, of the B-spline parametrization. To find these points we require

$$\tilde{\mathbf{X}}(\tilde{\xi}_i, \tilde{\eta}_j, \tilde{\zeta}_l) = \sum_{\tilde{i}=1}^{n_\xi} \sum_{\tilde{j}=1}^{n_\eta} \sum_{\tilde{l}=1}^{n_\zeta} B_{\tilde{i}, \check{p}_\xi, \mathbf{t}_1}(\tilde{\xi}_i) B_{\tilde{j}, \check{p}_\eta, \mathbf{t}_2}(\tilde{\eta}_j) B_{\tilde{l}, \check{p}_\zeta, \mathbf{t}_3}(\tilde{\zeta}_l) \tilde{\mathbf{P}}_{\tilde{i}, \tilde{j}, \tilde{l}} = \mathbf{Q}_{i,j,l} \quad (\text{D.6})$$

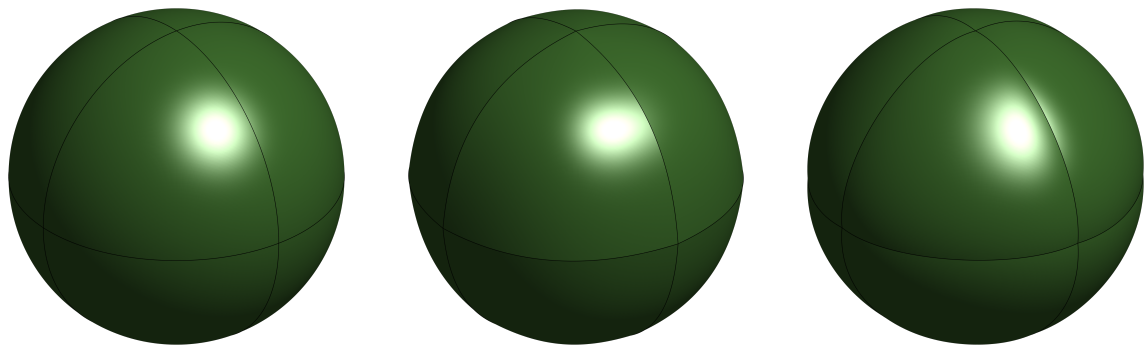
for all $i = 1, \dots, n_\xi$, $j = 1, \dots, n_\eta$ and $l = 1, \dots, n_\zeta$. We may therefore find $\tilde{\mathbf{P}}_{i,j,l}$ by solving a system of $3n_\xi \cdot n_\eta \cdot n_\zeta$ equations.

Application of this algorithm to the spherical shell parametrization using NURBS is illustrated in Figure D.36.

References

References

- [1] L. Gilroy, C. de Jong, B. Nolte, I. Schäfer, [BeTSSi II Benchmark Target Strength Simulation](#), Technical Report (WTD71 0029/2013 WB), Wehrtechnische Dienststelle für Schiffe und Marinewaffen der Bundeswehr, Maritime Technologie und Forschung (WTD 71), Eckenförde, Germany (2013).



(a) NURBS parametrization. (b) Approximation using $\check{p}_\xi = \check{p}_\eta = 2$. (c) Approximation using $\check{p}_\xi = \check{p}_\eta = 3$.

Figure D.36: Transformation of an exact NURBS parametrization of a spherical shell to a B-spline approximation of the same geometry.

- [2] P. Bouillard, F. Ihlenburg, [Error estimation and adaptivity for the finite element method in acoustics: 2D and 3D applications](#), *Computer Methods in Applied Mechanics and Engineering*, 176:147–163 (1999).
- [3] N. D. Manh, A. Evgrafov, A. R. Gersborg, J. Gravesen, [Isogeometric shape optimization of vibrating membranes](#), *Computer Methods in Applied Mechanics and Engineering*, 200:1343–1353 (2011).
- [4] N. D. Manh, [Isogeometric analysis and shape optimization in electromagnetism](#), Ph.D. thesis, Technical University of Denmark, Department of Informatics and Mathematical Modeling (2012).
- [5] T. Hughes, J. Cottrell, Y. Bazilevs, [Isogeometric analysis: CAD, finite elements, NURBS, exact geometry and mesh refinement](#), *Computer Methods in Applied Mechanics and Engineering*, 194:4135–4195 (2005).
- [6] J. A. Cottrell, T. J. Hughes, Y. Bazilevs, [Isogeometric Analysis: Toward Integration of CAD and FEA](#), Wiley, 2009.
- [7] L. Beirão da Veiga, A. Buffa, J. Rivas, G. Sangalli, [Some estimates for \$h\$ - \$p\$ - \$k\$ -refinement in isogeometric analysis](#), *Numerische Mathematik*, 118:271–305 (2011).
- [8] L. Beirão da Veiga, A. Buffa, G. Sangalli, R. Vázquez, [Mathematical analysis of variational isogeometric methods](#), *Acta Numerica*, 23:157–287 (2014).
- [9] P. Nørtoft, J. Gravesen, M. Willatzen, [Isogeometric analysis of sound propagation through laminar flow in 2-dimensional ducts](#), *Computer Methods in Applied Mechanics and Engineering*, 284:1098–1119 (2015).
- [10] S. A. Sauter, C. Schwab, [Boundary Element Methods](#), Springer Berlin Heidelberg, Berlin, Heidelberg, 2011, pp. 183–287.
- [11] M. Schanz, O. Steinbach, [Boundary Element Analysis: Mathematical Aspects and Applications](#), Lecture Notes in Applied and Computational Mechanics, Springer Berlin Heidelberg, 2007.
- [12] Y. J. Liu, S. Mukherjee, N. Nishimura, M. Schanz, W. Ye, A. Sutradhar, E. Pan, N. A. Dumont, A. Frangi, A. Saez, [Recent advances and emerging applications of the boundary element method](#), *Applied Mechanics Reviews*, 64:030802 (2012).
- [13] D. S. Burnett, [A three-dimensional acoustic infinite element based on a prolate spheroidal multipole expansion](#), *The Journal of the Acoustical Society of America*, 96:2798–2816 (1994).
- [14] K. Gerdes, L. Demkowicz, [Solution of 3D-Laplace and Helmholtz equations in exterior domains using \$hp\$ -infinite elements](#), *Computer Methods in Applied Mechanics and Engineering*, 137:239–273 (1996).
- [15] J.-P. Berenger, [A perfectly matched layer for the absorption of electromagnetic waves](#), *Journal of Computational Physics*, 114:185–200 (1994).
- [16] J.-P. Berenger, [Perfectly matched layer for the FDTD solution of wave-structure interaction problems](#), *IEEE Transactions on Antennas and Propagation*, 44:110–117 (1996).
- [17] S. Marburg, B. Nolte, [Computational Acoustics of Noise Propagation in Fluids-Finite and Boundary Element Methods](#), vol. 578, Springer, 2008.
- [18] S. N. Chandler-Wilde, I. G. Graham, S. Langdon, E. A. Spence, [Numerical-asymptotic boundary integral methods in high-frequency acoustic scattering](#), *Acta Numerica*, 21:89–305 (2012).
- [19] D. Givoli, [Numerical methods for problems in infinite domains](#), vol. 33, Elsevier, 2013.
- [20] J. J. Shirron, [Solution of exterior Helmholtz problems using finite and infinite elements](#), Ph.D. thesis, University of Maryland College Park (1995).
- [21] A. Bayliss, M. Gunzburger, E. Turkel, [Boundary conditions for the numerical solution of elliptic equations in exterior regions](#), *SIAM Journal on Applied Mathematics*, 42:430–451 (1982).
- [22] T. Hagstrom, S. Hariharan, [A formulation of asymptotic and exact boundary conditions using local operators](#), *Applied Numerical Mathematics*, 27:403–416 (1998), Special Issue on Absorbing Boundary Conditions.
- [23] R. Tezaur, A. Macedo, C. Farhat, R. Djellouli, [Three-dimensional finite element calculations in acoustic scattering using arbitrarily shaped convex artificial boundaries](#), *International Journal for Numerical Methods in Engineering*, 53:1461–1476 (2001).
- [24] P. Bettess, [Infinite elements](#), *International Journal for Numerical Methods in Engineering*, 11:53–64 (1977).
- [25] P. Bettess, O. C. Zienkiewicz, [Diffraction and refraction of surface waves using finite and infinite elements](#), *International Journal for Numerical Methods in Engineering*, 11:1271–1290 (1977).

- [26] L. Demkowicz, F. Ihlenburg, [Analysis of a coupled finite-infinite element method for exterior Helmholtz problems](#), *Numerische Mathematik*, 88:43–73 (2001).
- [27] A. Sommerfeld, *Partial differential equations in physics*, vol. 1, Academic press, 1949.
- [28] C. H. Wilcox, [An expansion theorem for electromagnetic fields](#), *Communications on Pure and Applied Mathematics*, 9:115–134 (1956).
- [29] R. Leis, *Initial Boundary Value Problems in Mathematical Physics*, J. Wiley & Teubner Verlag, Stuttgart, 1986.
- [30] F. Ihlenburg, *Finite Element Analysis of Acoustic Scattering*, vol. 132 of *Applied Mathematical Sciences*, Springer, New York, USA, 1998.
- [31] K. Gerdes, [The conjugated vs. the unconjugated infinite element method for the Helmholtz equation in exterior domains](#), *Computer Methods in Applied Mechanics and Engineering*, 152:125–145 (1998).
- [32] R. J. Astley, [Infinite elements for wave problems: a review of current formulations and an assessment of accuracy](#), *International Journal for Numerical Methods in Engineering*, 49:951–976 (2000).
- [33] J. J. Shirron, S. Dey, [Acoustic infinite elements for non-separable geometries](#), *Computer Methods in Applied Mechanics and Engineering*, 191:4123–4139 (2002).
- [34] J. J. Shirron, I. Babuška, [A comparison of approximate boundary conditions and infinite element methods for exterior Helmholtz problems](#), *Computer Methods in Applied Mechanics and Engineering*, 164:121–139 (1998).
- [35] J. V. Venås, T. Jenserud, [Exact 3D scattering solutions for spherical symmetric scatterers](#), *Journal of Sound and Vibration*, 440:439–479 (2019).
- [36] R. N. Simpson, M. A. Scott, M. Taus, D. C. Thomas, H. Lian, [Acoustic isogeometric boundary element analysis](#), *Computer Methods in Applied Mechanics and Engineering*, 269:265–290 (2014).
- [37] K. Gerdes, F. Ihlenburg, [On the pollution effect in FE solutions of the 3D-Helmholtz equation](#), *Computer Methods in Applied Mechanics and Engineering*, 170:155–172 (1999).
- [38] L. Coox, O. Atak, D. Vandepitte, W. Desmet, [An isogeometric indirect boundary element method for solving acoustic problems in open-boundary domains](#), *Computer Methods in Applied Mechanics and Engineering*, 316:186–208 (2017).
- [39] I. Babuška, F. Ihlenburg, E. T. Paik, S. A. Sauter, [A generalized finite element method for solving the Helmholtz equation in two dimensions with minimal pollution](#), *Computer Methods in Applied Mechanics and Engineering*, 128:325–359 (1995).
- [40] G. Strang, G. J. Fix, *An analysis of the finite element method*, vol. 212, Prentice-Hall Englewood Cliffs, NJ, 1973.
- [41] P. G. Ciarlet, *Basic Error Estimates for Elliptic Problems*, vol. 2, North-Holland, Amsterdam, The Netherlands, 1991.
- [42] T. Hughes, A. Reali, G. Sangalli, [Efficient quadrature for NURBS-based isogeometric analysis](#), *Computer Methods in Applied Mechanics and Engineering*, 199:301–313 (2010), Computational Geometry and Analysis.
- [43] K. A. Johannessen, [Optimal quadrature for univariate and tensor product splines](#), *Computer Methods in Applied Mechanics and Engineering*, 316:84–99 (2017), Special Issue on Isogeometric Analysis: Progress and Challenges.
- [44] J. V. Venås, [Isogeometric analysis of acoustic scattering](#), Master’s thesis, Norwegian University of Science and Technology, Trondheim, Norway (2015).
- [45] K. A. Johannessen, T. Kvamsdal, T. Dokken, [Isogeometric analysis using LR B-splines](#), *Computer Methods in Applied Mechanics and Engineering*, 269:471–514 (2014).
- [46] M. Kumar, T. Kvamsdal, K. A. Johannessen, [Superconvergent patch recovery and a posteriori error estimation technique in adaptive isogeometric analysis](#), *Computer Methods in Applied Mechanics and Engineering*, 316:1086–1156 (2017).
- [47] M. Peake, J. Trevelyan, G. Coates, [Extended isogeometric boundary element method \(XIBEM\) for two-dimensional Helmholtz problems](#), *Computer Methods in Applied Mechanics and Engineering*, 259:93–102 (2013).
- [48] M. Peake, J. Trevelyan, G. Coates, [Extended isogeometric boundary element method \(XIBEM\) for three-dimensional medium-wave acoustic scattering problems](#), *Computer Methods in Applied Mechanics and Engineering*, 284:762–780 (2015), Isogeometric Analysis Special Issue.
- [49] L. Engvall, J. A. Evans, [Isogeometric triangular Bernstein–Bézier discretizations: Automatic mesh generation and geometrically exact finite element analysis](#), *Computer Methods in Applied Mechanics and Engineering*, 304:378–407 (2016).
- [50] L. Engvall, J. A. Evans, [Isogeometric unstructured tetrahedral and mixed-element Bernstein–Bézier discretizations](#), *Computer Methods in Applied Mechanics and Engineering*, 319:83–123 (2017).
- [51] S. Xia, X. Qian, [Isogeometric analysis with Bézier tetrahedra](#), *Computer Methods in Applied Mechanics and Engineering*, 316:782–816 (2017), Special Issue on Isogeometric Analysis: Progress and Challenges.
- [52] D. S. Burnett, R. L. Holford, [An ellipsoidal acoustic infinite element](#), *Computer Methods in Applied Mechanics and Engineering*, 164:49–76 (1998).
- [53] M. Abramowitz, I. A. Stegun, *Handbook of Mathematical Function: With Formulas, Graphs, and Mathematical Tables*, Dover, New York, USA, 1965.
- [54] W. H. Press, S. A. Teukolsky, W. T. Vetterling, B. P. Flannery, *Numerical recipes in C*, vol. 2, Cambridge Univ Press, 1988.
- [55] L. Piegl, W. Tiller, *The NURBS book*, Springer Science & Business Media, 1997.